CHARACTERIZATION OF PLASMA ACTUATOR BASED MICROTHRUSTER CONCEPTS FOR HIGH ALTITUDE AIRCRAFTS AND CUBESATS

By

JIGNESH SONI

A DISSERTATION PRESENTED TO THE GRADUATE SCHOOL
OF THE UNIVERSITY OF FLORIDA IN PARTIAL FULFILLMENT
OF THE REQUIREMENTS FOR THE DEGREE OF
DOCTOR OF PHILOSOPHY

UNIVERSITY OF FLORIDA

2014

To Mom

ACKNOWLEDGMENTS

First of all, I would like to acknowledge my advisor and committee chair Dr. Subrata Roy, for his inimitable patience over the last five years as a friendly counsel in my journey through the maze of research. His unwavering support during the highs and lows of this sojourn has been crucial. I would like to thank committee members Dr. Norman Fitz-Coy for providing access to his experimental facilities, Dr. Lawrence Ukeiley for his constructive inputs, and Dr. Katia Matcheva for pointing me to the right sources for certain topics discussed in this thesis.

I would also like to thank my colleagues Tomas Houba, Ariel Blanco, Arnob Dasgupta, Navya Mastanaiah and Ankush Bhatia for the fruitful discussion on topics relevant to my research; Pengfei Zhao for discussions and assistance for the experimental work; and Moses Diwaker for his friendship and solidarity. I want to thank my family for their patience and support through my years in grad school. I'd like to thank my friends Amit Patel and Aastha Parikh, who have been family away from family. Lastly, I want to thank my brother Himanshu for instilling in me a sense of curiosity and creativity as a kid, to which I owe this thesis.

TABLE OF CONTENTS

page

LIST OF TABLES

LIST OF FIGURES

Abstract of Dissertation Presented to the Graduate School
of the University of Florida in Partial Fulfillment of the
Requirements for the Degree of Doctor of Philosophy

CHARACTERIZATION OF PLASMA ACTUATOR BASED MICROTHRUSTER CONCEPTS FOR HIGH ALTITUDE AIRCRAFTS AND CUBESATS

By

Jignesh Soni

December 2014

Chair: Subrata Roy
Major: Aerospace Engineering

Growing interest in small satellites and high altitude gliders warrants the development of suitable microthrusters to provide control authority. A feasibility study for a plasma actuator powered microscale propulsion device for high altitude application and small satellites is presented to address this need. Dielectric barrier discharge (DBD) actuators have been studied extensively for flow control applications at atmospheric pressures both under quiescent and free-stream velocity conditions. While conventional actuators have been characterized at atmospheric pressures, the proposed microthruster is intended for high altitude operation. Thus, the low pressure and low temperature characterization of DBD actuators are conducted. The effect of dielectric thickness and operating voltage on thrust, power and effectiveness are investigated. An empirical relation based on observed data is also proposed for predictive capabilities. The validation of the microthruster concept requires a thrust stand capable of microNewton level resolution. To meet this challenge, a high resolution thrust stand is designed, characterized, and validated. Novel calibration technique and damping mechanism are implemented to improve accuracy and functionality. The effect of magnetic field on DBD actuator performance is also investigated. To circumvent the

high wall shear losses of surface DBD actuators, volumetric DBD actuators are explored, and demonstrated to have better thrust and effectiveness performance. In the low pressure limit, several electrostatic and electromagnetic thruster designs utilizing DC glow discharge plasma are presented and investigated. The data presented in the thesis is intended to define the design space for future development of a prototype microthruster for space to ground applications like de-orbiting.

CHAPTER 1
INTRODUCTION

The realm of thrusters spans a wide regime, ranging from aircrafts flying at altitudes of several kilometers to satellites and spacecrafts orbiting at altitudes of several hundreds of kilometers. Atmospheric propulsion deals with aviation below the Karman line, which is considered as the boundary between Earth's atmosphere and space. Lying at an altitude of 100 kms, the Karman line represents the limit at which the atmosphere is too thin to generate enough aerodynamic lift to support the vehicle's weight, such that the aircraft would need to travel faster than the orbital velocity to sustain level flight (Darrin & O'Leary, 2009). Although reaching and maintaining orbits has been possible for decades, atmospheric light below the Karman line has remained out of reach due to limitations of airbreathing propulsion. The only aerial crafts that have been able to come close are hot air balloons. Recently there has been impetus to push the realm of atmospheric flight to higher altitudes, with significant efforts coming from the meteorological community in a quest to in an effort to study the upper atmosphere.

1.1 Need for Micropropulsion for Space Applications

The progresses in the fields of electronics driven by microelectronics and miniaturization have made a strong case for transition to small satellites (Stoewer, 1996). Launching several small satellites instead of a large one offers several advantages. Smaller, self-sufficient, one-off satellites can be launched along with several small satellites or 'piggy-back' on a large satellite on a conventional launch vehicle, significantly reducing the launch cost per satellite (Sandau, 2010). This is particularly conducive for satellites with very specific and short term missions, such as university research satellites, which are aimed at providing the students hands-on

experience with the subject of spacecraft engineering. Several satellites working on a single mission can be launched as a team, each focusing on a specific aspect of the mission, thus providing redundancy in the event of failure of one among them (Barnhart, Vladimirova, & Sweeting, 2007). A cluster of nano-satellites also offers expanse of coverage, formation flying ability, and faster revisit/coverage times. Table 1-1 shows the conventionally used classification for satellites.

Table 1-1. Mass classification of Satellites (Barnhart, Vladimirova, & Sweeting, 2007)

Category	Wet Mass (kg)	Cost (USD)
Large satellite	>1000	0.1 – 2 B
Medium sized satellite	500-1000	50 – 100 M
Mini satellite	100-500	10 – 50 M
Micro satellite	10-100	2 – 10 M
Nano satellite	1-10	0.2 – 2 M
Pico satellite	0.1-1	20 – 200 K
Femto satellite	<0.1	0.1 – 20 K

Much like conventional satellites, small satellites need to maintain precise orientation in orbit. For example, a satellite may need to constantly face a ground station on earth, orient the solar panels to optimize solar power production, or point to a partner satellite in orbit (particularly true for satellite constellations). For these operations, satellites in orbit need propulsion options like attitude control and orbit correction thrusters. A wide variety of thruster designs and options have been developed and used since the inception of small satellites to achieve these objectives. For nano-satellites typically weighing between 1 and 10 Kg, these thrusters require very minute forces for station keeping, orbital maneuvers, and attitude control. These forces are often of the order of several microNewtons or less.

Moreover, satellites in Low Earth Orbit (LEO) suffer from accumulated orbital decay over time due to atmospheric drag resulting in gradual de-orbiting. To correct for these deviations, the satellites require a boost at regular intervals to raise the orbit back to the desired level. The measure of the amount of effort required to bring about these changes in the trajectory of an orbiting body is called the delta-V (Δv). A Δv of approximately 0.6 m/s per km of altitude change is required in a LEO at 250 km altitude (Wertz & Larson, 2007). The Δv requirements for a similar mission for a 100 kg micro-satellite are reproduced in Figure 1-1 (Scharfe & Ketsdever, 2009).

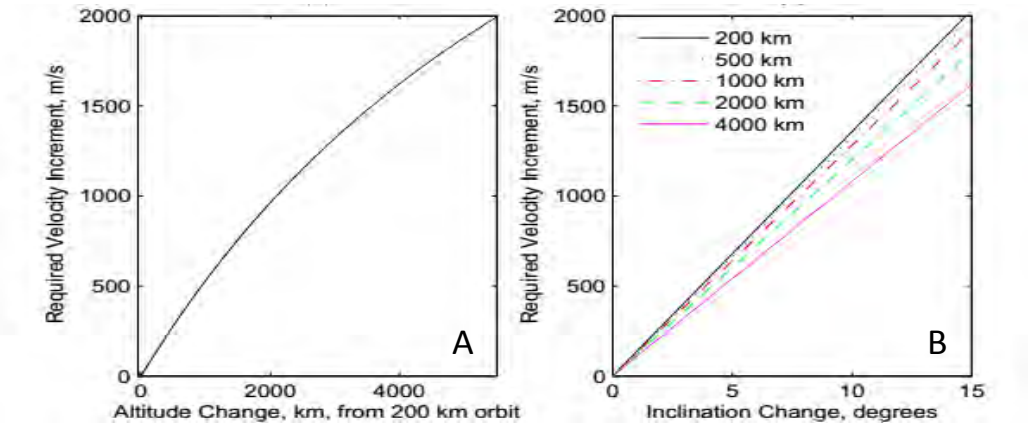

Figure 1-1. Delta-V requirement for different orbital maneuvers. A) To alter the altitude of the initial 200 km circular orbit. B) To change orbit inclination at various altitudes (Scharfe & Ketsdever, 2009).

A host of other maneuvers for appropriate orientation (orbit inclination, attitude control, slew), require varying amounts of Δv. Impulse bit requirements for a 1° change in pointing or orientation for a 1 kg satellite have been estimated to be around 29 μNs (Muller, 2000). Changes in orbit inclination requires a Δv of about 136 m/s per degree of plane change at a LEO orbit, while a 180° slew maneuver performed over one minute might require a steady thrust level of about 0.06 mN (Wertz & Larson, 2007). A JPL study for a 5 kg inspection satellite suggested a thrust capability of 10 mN to meet the

thrust requirements resulting from various maneuvers (Mueller, Goldberg, & Alkalai, 2007).

An estimate of the thrust requirements for drag compensation can be made from fundamentals of aerodynamics and orbital mechanics. For demonstration, a nano-satellite of the shape of a cube of 10 cm x 10 cm x 10 cm size with a mass of 1 kg (called a CubeSat), is assumed to be orbiting at a LEO altitude of 300 km. The orbital velocity at this altitude is,

$$v = \sqrt{\frac{GM}{r}} = 7728\ m/s \tag{1-1}$$

Air density at that altitude is about 1.9×10^{-11} kg/m^3 (Young J. L., 2001), and the coefficient of drag for a three dimensional cube is known to be 1.05 (Young, Munson, & Okiishi, 2004). Accordingly, the drag on the CubeSat of given dimensions at this altitude and orbital velocity is given by

$$F_d = \frac{1}{2} C_d \rho A v^2 = 5.95\ \mu N \tag{1-2}$$

To maintain the CubeSat in its designated orbit, the thruster would need to apply a constant thrust of this magnitude to compensate for atmospheric drag..

In discussing various propulsion technologies, the metric of comparison is the amount of velocity increment gained per unit mass of the propellant used. This metric, called the Specific Impulse (I_{sp}), is defined as change in momentum per unit propellant spent

$$I_{sp} = \frac{\Delta M}{m g_0} = \frac{\Delta M / t}{(m g_0)/t} = \frac{F}{\dot{m} g_0} \tag{1-4}$$

Higher the I_{sp}, lesser the mass of the propellant required to achieve a certain velocity increment. The Specific impulse is related to the exhaust velocity as

$$I_{sp} = \frac{F}{\dot{m} g_0} = \frac{\dot{m} v_e}{\dot{m} g_0} = \frac{v_e}{g_0} \tag{1-5}$$

This is deducible from the fact that a higher exhaust velocity will impart a higher reactive momentum to the vehicle for the same mass flow rate of propellant. It is also interesting to note that Specific Impulse is a function of the gravitational field the vehicle is working against. A rocket designed on Earth will have a higher specific impulse on Mars, all other parameters being identical.

Conventional thrusters like cold-gas, mono-propellant, and electrothermal thrusters have been miniaturized to meet the propulsion requirements for small satellites. However, with reducing scales of size and weight, these devices suffer from rapid deterioration in performance vis-a-viz efficiency, specific impulse, and thrust per weight. Electrostatic and electromagnetic propulsion options, although providing high specific impulse, are weight and power extensive. These constraints have led to the development of many novel microthruster concepts. (Paulson & Soberster, 2013)

1.2 Need for Micropropulsion for Atmospheric Applications

The need for thrusters is not limited to satellites in orbit. Study of stratospheric altitudes limits the use of conventional aircrafts due to low air density (Sóbester, 2011). Hot air weather balloons, the method of choice for decades, suffer from zero to very little control authority and hence geographical coverage (Paulson & Soberster, 2013). The concept of high altitude sailplanes and gliders has received considerable attention in recent years .These unpowered gliders are suitable for missions that require little

control authority and no on-board propulsion, and benefit from extended spatial and temporal coverage (Paulson & Sobester, 2013). Several such gliders are being investigated across the globe. Project MAVIS (Massive Atmospheric Volume Instrumentation System) involves launching a fleet of small instrumented gliders from a high altitude weather balloon. The autopilot-guided descent paths can be optimized for sampling efficiency, collecting an accurate meteorological map. Project ASTRA (Atmospheric Science Through Robotic Aircraft) is investigating the use of such a balloon launched glider for gathering information about atmospheric observables at Stratospheric altitudes. Test flights have demonstrated peak altitude of over 70,000 ft and range of over 100 kms. Figure 1-2 shows the test glider and balloon launch developed as part of the project (Sobester, et al., 2011)

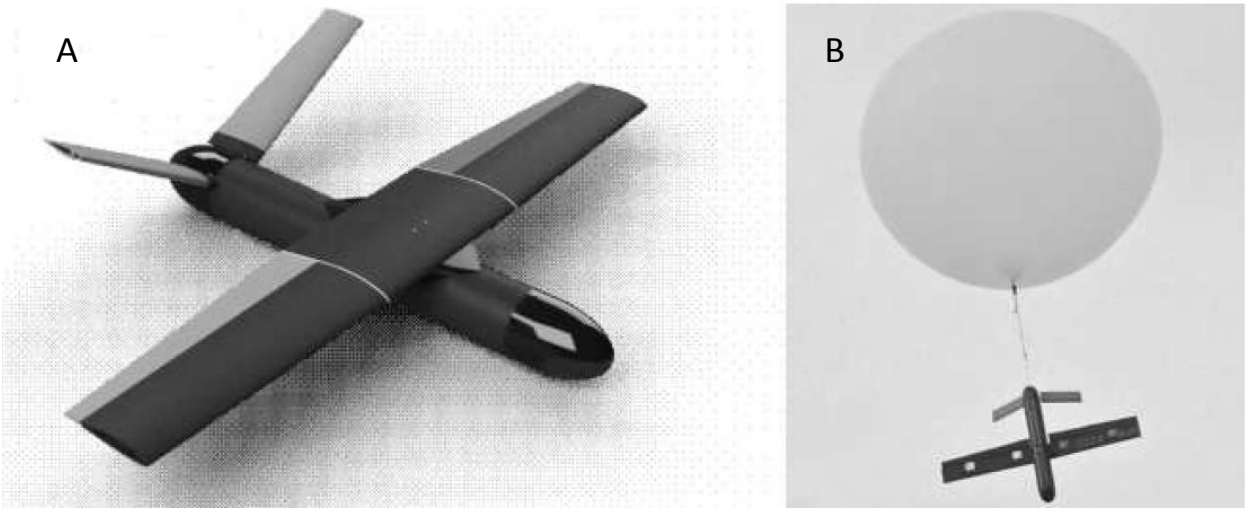

Figure 1-2. BALUGA sensorcraft glider prototype developed as part of project ASTRA. A) Details of the glider. B) Launch from a high altitude balloon (Sobester, et al., 2011).

The control authority of such a glider can be improved by augmenting with active thrust control. This can lead to gains in the range and times over which the glider can gather data. Conventional methods of flight control involve moveable surfaces and

come with associated complexities of servo mechanisms and linkages, and added weight penalty. This opens up the possibility of using thrust vectoring technologies to achieved flight control. During its flight, as the glider traverses through the atmosphere, the ambient conditions (pressure and temperature) vary significantly throughout its altitude. Figure 1-3 shows the temperature and pressure profile such a glider is expected to endure and perform under, (Stratosphere to Sea Level) where the ambient pressure varies by over 3 orders of magnitude and temperature by almost 100 degrees. The performance of any thrust producing under these conditions would need to be characterized and understood well to allow optimum design.

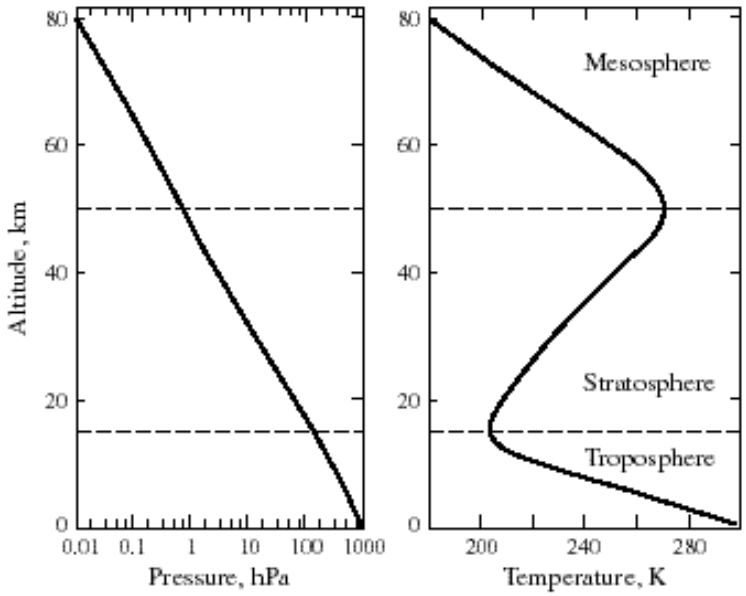

Figure 1-3. Variation in ambient pressure and temperature with altitude (Daniel, 1999).

The proposed thruster is based on the principle of DBD actuation. The performance of theses actuators depends significantly on environmental conditions such as pressure, temperature, humidity, and gas composition. Most work on DBD actuators has been performed at atmospheric pressures and temperature. There is a

gap in the current understanding of how these devices perform at elevated altitudes, such as those encountered by a high altitude glider.

The wider goal of this thesis is a conceptual thruster design capable of performing through a wide range of altitude: in orbit, as well as in lower atmosphere, as illustrated in Figure 1-4. The design paradigm is the desire to be able to use atmospheric air as propellant as long as the altitude permits considering decreasing air density. Once the density is lower than the desired critical performance point, onboard propellant could be used as the working propellant. Such a concept has been under development at conventional scales in the form of the SABRE (Synergistic Air-Breathing Rocket Engine) (Longstaff & Bond, 2011). However no such concept exists at the scales intended for small spacecrafts and aircrafts. *It is this gap this thesis intends to address*.

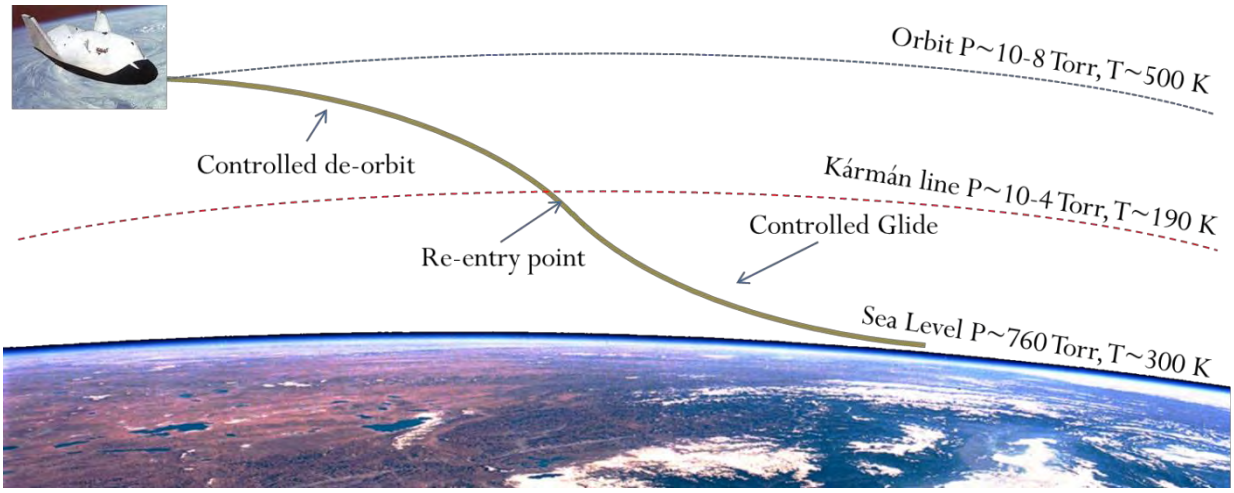

Figure 1-4. Design objective: Orbit to Earth propulsion system.

The rest of the thesis is organized as follows. Chapter 2 provides an overview of existing micropropulsion technologies and the state of the art, along with some discussion on the merits and limitations of each. Chapter 3 presents an overview of gas discharges and plasma physics to enable better understanding of the phenomena.

Chapter 4 reviews the concepts of DBD actuators vis-à-vis the concept, working principle, physics, and characteristics. Chapter 5 will present details of the new microthruster being proposed as part of this thesis, along with preliminary results from numerical simulations performed at the Applied Physics Research Group. Chapter 6 will present the design, characterization, and validation of a custom thrust stand built to measure the micronewton level thrust expected from the proposed thruster. Chapter 7 presents a survey of low pressure DBD actuation, along with the findings of the current research. Chapter 8 discusses the effect of ambient air temperature and dielectric heating on actuator performance. Chapter 9 looks at the effect of magnetic field on conventional DBD actuator in an effort to enhance its performance and presents the findings. Chapter 10 explores volumetric DBD actuators and presents a comparison with conventional surface DBD actuators, suggesting some merit over the latter. Chapter 11 explores several non-DBD thruster concepts, including electrostatic and electromagnetic thruster concepts, and presents a case for further exploration. Chapter 12 makes recommendations for future work based on the finding of this thesis, and provides a roadmap to carry out the recommended work, along with preliminary data.

CHAPTER 2
REVIEW OF EXISTING MICROPROPULSION TECHNOLOGIES

The need for precise maneuvering of small satellites in orbit requires thrusters that can impart minute forces in the desired direction. For larger satellites, conventional technologies like cold-gas, mono-propellant, chemical and electrothermal thrusters have been used reliably. However, with reducing scales of size and weight, each of these options becomes increasingly untenable. The weight penalties associated with chemical thrusters in terms of inert weight of thruster subsystems (pumps, valves, separate storage tanks) render them unsuitable for down scaling. These limitations have led to exploration into miniaturization of other thruster technologies, and development of novel thruster types designed solely to meet low thrust, high specific impulse demands of small satellites. To put the proposed thruster in perspective of the state of the art, a survey of existing micro-propulsion technologies along with their limitations is presented below.

2.1 Overview of Space Propulsion Technology

Generally, space propulsion options are broadly classified into three types:

- Chemical Propulsion
- Electrical Propulsion
- Nuclear Propulsion

Propulsion requirements for microsatellite applications generally necessitate low thrust and high I_{sp} devices. These requirements are readily met by two categories of thrusters: chemical and electrical, either of which is further divided into subtypes based on working principle, design details, and propellant types. Several prototypes in each of these subtypes have been designed and tested in the last few decades with varying degrees of success. Some designs have been deployed on actual missions, proving

their worth. Excellent and extensive reviews of available thruster designs and demonstrated performance are available in literature (Mueller, Hofer, & Ziemer, 2010; Mueller J. , 1997; Mueller J. , 2000; Janson, Helvajian, Hansen, & Lodmell, 1999; Scharfe & Ketsdever, 2009; Mueller, Ziemer, Richard, Wirz, & O'Donnell, 2008). In the interest of brevity, only relevant and representative designs are discussed in the following section.

2.2 Survey of Existing Chemical Propulsion Options for Micro Satellites

2.2.1 Cold Gas Thrusters

Cold gas thrusters are the simplest of all propulsion options. These devices produce thrust by virtue of a compressed gas exiting a nozzle. Control authority is achieved by a valve that dictates propellant flow. Apart from simplicity of design, cold gas thrusters offer several other advantages such as non-toxic propellants, lack of spacecraft contamination from reaction products, lack of thermal concerns (heating and structural), and no net charging of the spacecraft (unlike Ion thrusters).

Cold gas thrusters conventionally used for attitude control of large satellites have a thrust range of 4.5 mN – 105 N (Mueller, Hofer, & Ziemer, 2010). For micro-satellites requiring forces of the order of micronewtons, further downscaling using conventional manufacturing technologies vis-à-vis valve design and nozzle machining has proven challenging. This has led to non-conventional approaches in the design of cold-gas thrusters, including micromachining and lithography. Whilst Deep Reactive Ion Etching (DRIE) has been used to fabricate micro nozzles (Figure 2-1) to successfully achieve supersonic expansion with up to 98% nozzle effectiveness at 19 μm nozzle width (Bayt, Breuer, & Ayon, 1998), piezoelectric valves with a footprint of only 2.8 mm and 200 μm

thickness have been developed for proportional control of propellant flow, offering significant reductions in weight and power consumption (Kohler, et al., 2002).

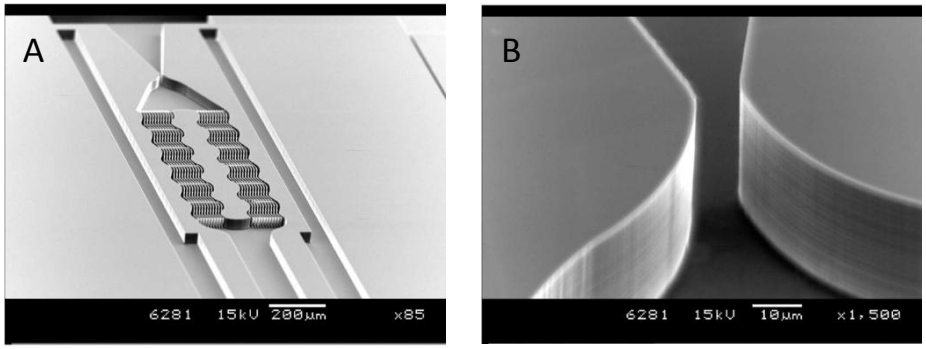

Figure 2-1. Silicon micro-machined cold gas thruster. A) SEM image the cold gas thruster chip. B) Close up of the nozzle throat with throat width of 10 µm (Kohler, et al., 2002).

The main drawback of cold gas thrusters is their limited specific impulse. Almost all variants of cold-gas thrusters have an I_{sp} between 65-85 s, rendering them unsuitable for missions with long durations and hence high Δv since more propellant needs to be carried to compensate for the low specific impulse.

2.2.2 Mono Propellant Thrusters

Mono propellant thrusters are thrusters that utilize only one working propellant. The propellant is passed through a catalyst bed, which either reacts with the propellant or decomposes it in an exothermic process, resulting in thermal expansion of the products. Hydrazine, which has been the propellant of choice for many years, is used in conjunction with alumina catalyst bed made of pellets in a mesh construction (Muller, 2000).

For microscale applications, due to the limited surface area availability of the catalytic bed, electrolytic ignition has been used to achieve decomposition of the propellant. In one such design (Wu & Yetter, 2009), the inside surface of the combustion chamber is lined with screen-printed silver electrodes (Figure 2-2). The

hydroxyl-ammonium nitrate (HAN) based liquid propellant undergoes exothermic chemical decomposition when a potential difference is applied across the electrodes. The thruster itself was fabricated using commercial Low Temperature Co-fired Ceramic tapes, and the entire thruster 'chip' (excluding the power supply) occupied a volume of 0.82 mm^3 (25.4 mm x 12.7 mm x 1 mm). The thruster was able to generate impulse bit of 0.003 Ns with a peak thrust of 150 mN using a voltage input of 45 V. HAN, however, is known to be highly toxic and corrosive, leading to electrode degradation over time.

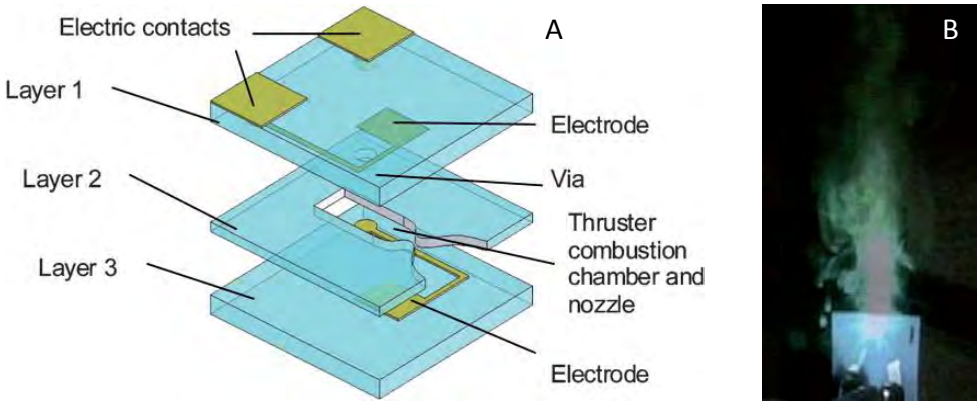

Figure 2-2. Liquid monopropellant microthruster. A) Schematic of the LTCC tape electrolytic thruster. B) Test firing of the device (Wu & Yetter, 2009).

A hydrazine based microthruster, composed of Si-micro-machined micro-reactor and micro-nozzle has been reported in literature (Yuan, Li, Huang, Chen, & Chen, 2011). The hydrazine propellant is decomposed on passing through a micro-machined catalyst bed, composed of iridium deposited on a Ti/SiOx/Si substrate (Figure 2-3). The design was able to generate a thrust of about 1 mN at hydrazine flow rates of 0.43 – 1.20 mg/s. The specific impulse observed was close to 162 s, with an associated hydrazine dissociation rate of up to 92.3 – 94.6 %. Heat loss through the thruster structure was found to be a significant source of performance limitation, along with degradation of the catalyst bed.

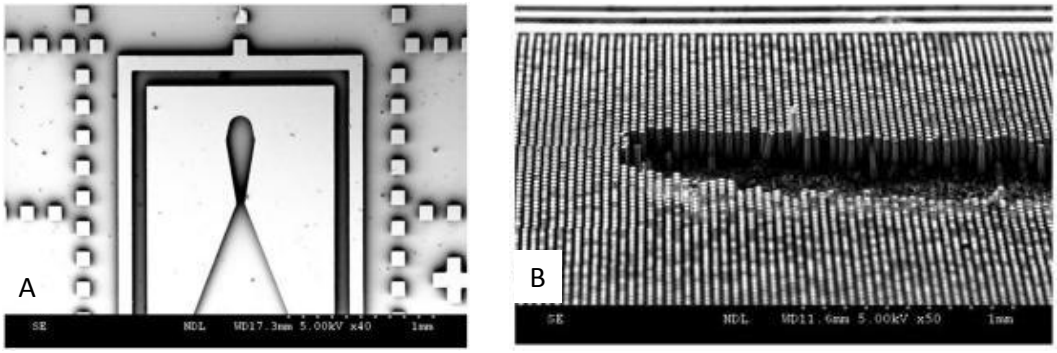

Figure 2-3. Silicon micromachined monopropellant thruster. A) SEM image of the micromachined nozzle. B) Iridium coated micro-machined micro-reactor catalyst bed (Yuan, Li, Huang, Chen, & Chen, 2011).

2.2.3 Solid Bi-Propellant Thrusters

Solid propellants offer the advantages of simplicity of design and ease of propellant storage. Several solid propellant micro rocket motors have been developed using various micromachining techniques. A MEMS microscale rocket fabricated using silicon micromachining is reported in literature (Rossi, Orieux, Larangot, Conto, & Esteve, 2002). The micro rockets utilize a metal-oxidizer fuel combination of Al-NH_4ClO_4 using polybutadiene polymer as binder. A polysilicon resistor is patterned onto a thin dielectric membrane and acts as the igniter (Figure 2-4). Experimental testing demonstrated a thrust range of 0.36 – 8.9 mN depending on geometry and nozzle throat diameter (Rossi, et al., 2006).

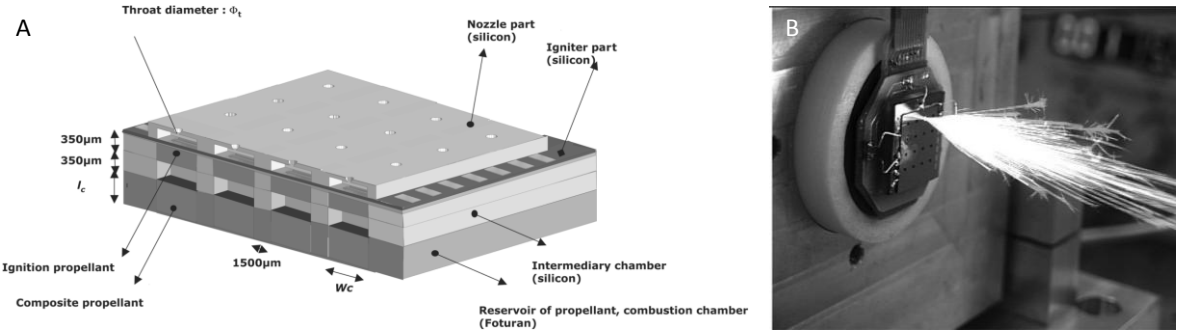

Figure 2-4. Al-NH_4ClO_4 based solid propellant MEMS microthruster. A) Schematic of the array of 16 solid propellant thrusters. B) Test firing of a demonstration prototype (Rossi, et al., 2006).

A slightly modified design (Zhang, Chou, & Ang, 2004; Zhang K. L., Chou, Ang, & Tang, 2005) offered a simpler fabrication process suitable for batch production (Figure 2-5). Using gunpowder based propellant, the thruster design was able to deliver between 3.52 x 10^{-5} to 2.11 x 10^{-4} Ns of total impulse at sea level, corresponding to an I_{sp} of 4.48 – 28.29 s.

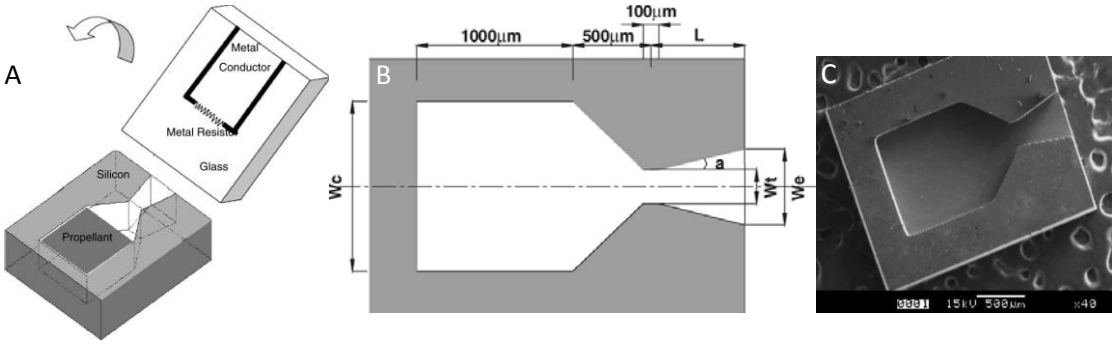

Figure 2-5. Gunpowder based solid propellant MEMS microthruster. A) Schematic of the microthruster. B) Dimensional sketch. C) SEM image of the microthruster (Zhang K. L., Chou, Ang, & Tang, 2005).

Both the aforementioned designs are suitable only for impulse *bits*. They suffer from the inherent limitation of solid propellant when it comes to throttleability and reuse.

2.2.4 Liquid Bi-Propellant Thrusters

The higher specific impulse of bi-propellant thrusters in general has resulted in the quest to miniaturize the technology to mitigate the low I_{sp} of cold-gas and mono-propellant thrusters.

A highly miniaturized version of a high pressure bi-propellant rocket has been fabricated using silicon micromachining (London, et al., 2001). Individually etched single crystal silicon wafers are stacked and fusion bonded to create the propellant feed channels, combustion chamber and nozzle. Regenerative cooling using ethanol or water as coolant is employed by etching 9 µm wide cooling grooves (Figure 2-6). A fuel-oxidizer combination of gaseous methane and oxygen was able to generate a thrust of

1 N at a chamber pressure of 12 atm, delivering a thrust to weight ratio of 85 while delivering 750 W of thrust power. Further downscaling posed design challenges, and the thrusts levels of the order of milliNewtons or less were difficult to reproduce reliably.

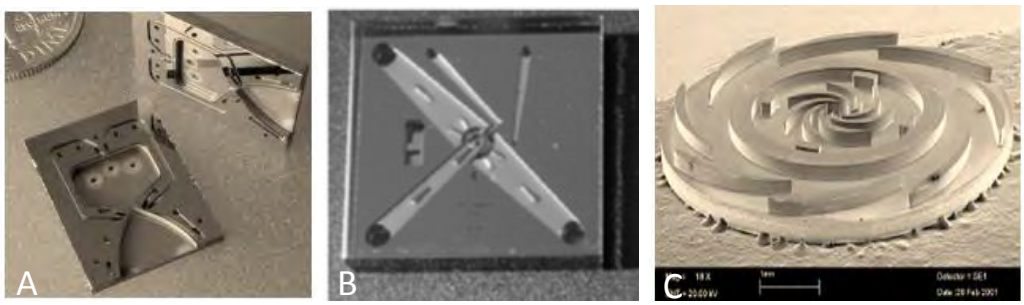

Figure 2-6. Liquid bipropellant micro-rocket engine. A) Si micromachined combustion chamber and nozzle. B) 1" square microturbopump chip. C) SEM image of the 6 mm diameter turbopump impeller (Epstein, Li, jacobson, & Kerrebrock, 2005).

2.2.5 Gaseous Bipropellant Thrusters

A gaseous bipropellant microthruster has been fabricated using LTCC tapes for structural elements and silver spark-ignition electrodes (Wu & Lin, 2010). Numerical simulations of the combustion process were found to agree well with the experimental observations made using a sapphire window in the combustion chamber walls. The thruster was capable of producing a thrust output between 0.2 and 1.97 mN, throttled by controlling the propellant flow rate using oxygen and ethylene propellants (Figure 2-7).

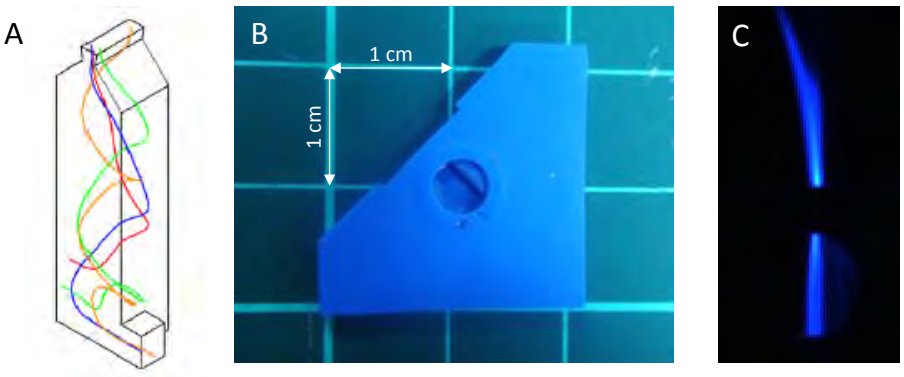

Figure 2-7. Gaseous fuel bipropellant micro-rocket. A) Numerical simulation of fuel-oxidizer flow in the thruster. B) Test prototype device. C) Image of thruster combustion plume (Wu & Lin, 2010).

2.3 Survey of Existing Electric Propulsion Options for Micro Satellites

2.3.1 Electrothermal Thrusters

Electrothermal thrusters are a class of electric propulsion devices that convert electrical energy into thermal energy of the propellant, which is manifested as the kinetic energy of the heated gas exiting through a nozzle, thus generating thrust. The use of resistive heating is most common, although other methods (arc heating, microwave heating) have been used successfully.

2.3.1.1 Resistojets

A novel electrothermal microthruster, called the Free Molecular Micro Resistojet (FMMR), has been reported in literature (Lee, Lilly, Muntz, & Ketsdever, 2005). The design utilizes microphotolithography techniques to fabricate a heater chip on a silicon wafer. Resistive elements are made of pattern deposited Ti/Pt/Au using Plasma Enhanced Chemical Vapor Deposition. The heater chip has an array of micro slots etched into it, with the resistive elements patterned around the periphery of the slots (Figure 2-8). The chip is mounted on a plenum which is supplied with a propellant and is maintained at 50 Pa plenum pressure. The resistive heating of the Ti/Pt/Au pattern can heat the chip to a temperature of up to 600 K while keeping the power consumption under 3 W. (Ketsdever, Green, Muntz, & Vargo, 2000; Wong, Reed, & Ketsdever, 2001). The exiting propellant picks up thermal energy from the heater chip surface by molecular heat transfer, thus providing more thrust than pressure driven flow alone. Numerical simulations of the device predicted exit velocities, thrust, and specific impulse of the order of 450 m/s, 0.2 – 1.5 mN, and 45 – 77 s respectively (Ahmed, Gimelshein, & Ketsdever, 2005). Experimental testing using water propellant demonstrated thrust values of 129 μN at a specific impulse of 79.2 with heater chip temperature of 580 K

(Lee, Bauer, Killingsworth, Lilly, & Duncan, 2007). Depending on the propellant used, heater chip temperature, and mass flow rate, thrusts up to 1.7 mN at a specific impulse of up to 160 s could be achieved (Ketsdever, Lee, & Lilly, 2005). Heat loss through the plenum and chip, however, remained a significant source of loss and lead to low energy conversion efficiency.

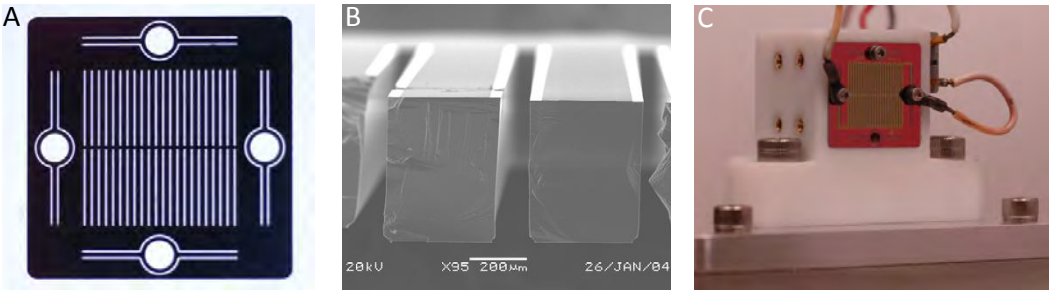

Figure 2-8. Free Molecular Micro Resistojet. A) Microfabricated Si heater chip. B) SEM image of the etched slots. C) Demonstration prototype of the FMME thruster (Ketsdever, Lee, & Lilly, 2005).

2.3.1.2 DC Arcjets

DC arcjets improve the performance of cold gas thrusters by generating an electrical arc discharge in the propellant flow to impart additional energy, thus improving the specific impulse. The configuration generally involves electrodes placed at the exit of the nozzle to minimize heat loss to the thruster walls. Arc jet thrusters using gaseous, liquid, as well as solid propellants have been utilized. Gaseous propellants are generally pressure fed, and act like arc-enhanced cold-gas thrusters. Liquid propellant thrusters are delivered either by a pump or by capillary action. For solid propellants, the arc ablates a small amount of material from the propellant block, which then accelerates by thermal expansion.

Figure 2-9 (A) shows a solid propellant design (Schein, et al., 2001) which utilizes a coaxial electrode arrangement with the cathode at the center. The metal cathode also acts as the propellant block, and is consumed over the lifetime of the

thruster. A titanium cathode demonstrated thrust to power ratios of up to 2.2 μN/W, with force resolution of up to 1 μN. Specific impulse ranged from 1100 s for tantalum to 3000 s for titanium. Impulse bits up to 100 μNs have been generated at 100 Hz using chromium cathode. Figure 2-9 (B) shows the power processing unit (PPU) that can power such a thruster. The entire unit is 4 cm x 4 cm x 4 cm, weighs 150 g, and can run off a 12/24 volt satellite bus. Figure 2-9 (C) shows an Alameda Applied Science/ JPL Vacuum Arc Thruster in operation, based on similar principles (Mueller, Hofer, & Ziemer, Survey of propulsion technologies applicable to cubesats, 2010).

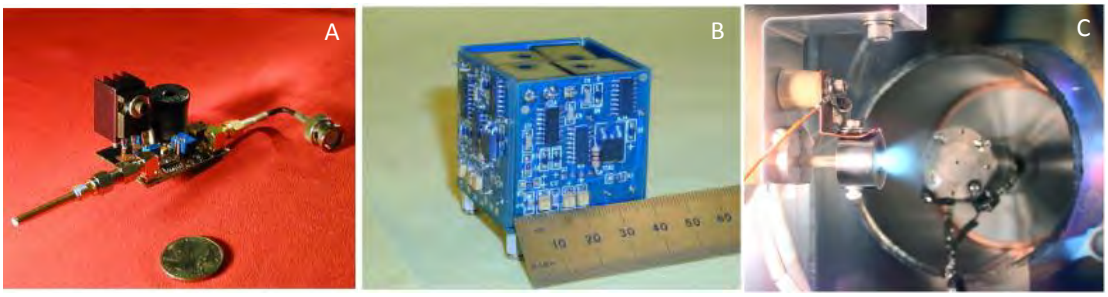

Figure 2-9. DC Arcjet microthrusters. A) Vacuum arcjet thruster (Schein, et al., 2001). B) PPU developed for powering the arcjet thruster (Rysanek, Hartmann, schein, & Binder, 2002). C) AASC Vacuum Arc Thruster under testing (Mueller, Hofer, & Ziemer, 2010).

2.3.1.3 Microwave Arcjets

Microwave arcjets use alternating electric fields to set up oscillations in polar molecules, resulting in thermal heating and subsequent expansion through a nozzle to generate thrust. One such design, called the Microdischarge Cavity Thruster (Burton, et al., 2009) uses aluminum foil electrodes covered in Al_2O_3 by nanoporous structure anodization (Fig. 2-10). A pair of such foils is combined, and micro-cavities for nozzles are chemically etched using wet electrochemical processes. Nozzles with throat and exit diameters down to 75 μm and 100 μm respectively have been reliably fabricated. Initial testing demonstrated thrust capacity of up to 1 mN at a thermal efficiency of about

22 %. Heat loss to the micro-cavity walls was found to be a contributing factor to the average performance of the test thruster.

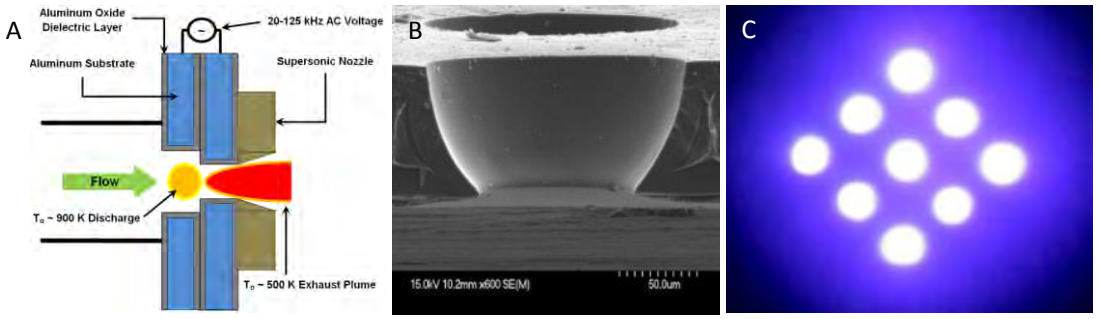

Figure 2-10. Microwave arcjet microthruster. A) Schematic of a microdischarge cavity thruster (Burton, et al., 2011). B) SEM image of a micronozzle etched in Si (Burton, et al., 2009). C) MEMS micro-cavity plasma discharge (Burton, et al., 2011).

2.3.2 Electrostatic Thrusters

Electrostatic thrusters are a class of thrusters that convert electrical energy directly into kinetic energy using Coulomb forces. The design uses electrostatic forces to accelerate heavy charged ions towards the thruster exit, imparting a reactive momentum to the vehicle. In the simplest schemes, a gaseous propellant is first ionized by strong electric fields or high energy electrons. The resulting ions are then accelerated towards a screen maintained at a negative potential (cathode), which accelerates the ions as they exit the thruster. To alleviate gradual charge buildup, the exiting ion beam is neutralized by an electron gun, which also prevents reverse interaction of the plume with the spacecraft which can result in contamination of critical surfaces such as solar panels and sensors (Goebel & Katz, 2008).

For micro-propulsion, electrostatic thrusters are generally classified into three types: gridded ion engines, Hall effect thrusters, and colloid thrusters.

2.3.2.1 Gridded Ion Thrusters

Gridded ion thrusters utilize a metal screen maintained at a negative potential to attract positively ionized propellant atoms. For micro-propulsion, the design is essentially a scaled down version of the conventional ion engines that have been used for spacecraft attitude control thrusters. Figure 2-11 presents three such designs, and Table 2-1 provides design details and performance parameters for these thrusters. High thruster mass remains a challenge for these designs. For a nanosatellite weighing 1 kg, a thruster mass alone (without considering the PPU) occupies about 20% of the total spacecraft mass.

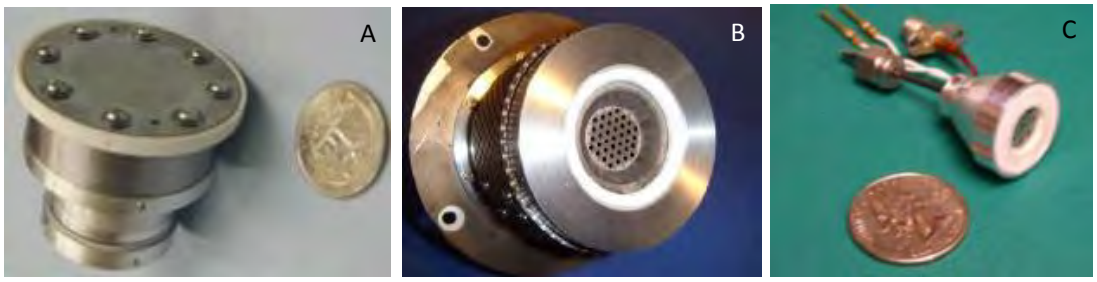

Figure 2-11. Gridded ion microthrusters. A) JPL Miniature Xenon Ion Thruster (MiXI). B) University of Giessen μNRIT-2.5 Miniature Ion Thruster. C) Penn State University MRIT Micro-Ion Thruster (Mueller, Hofer, & Ziemer, 2010).

Table 2-1. Design and Performance parameters of the MiXI, μNRIT-2.5, and MRIT (Mueller, Hofer, & Ziemer, 2010)

Model	MiXI	μNRIT-2.5	MRIT
Propellant	Xe	Xe	Ar
Thrust (mN)	0.01 1.5	0.05 – 0.6	0.001 – 0.06
I_{sp} (s)	2500 - 3200	2861	5480
Power (W)	13-50	13-34	-
Efficiency (%)	> 40	4 - 47	15
Diameter (cm)	3	2.5	2
Mass (g)	200	210	-

2.3.2.2 Hall Thrusters

Gridded ion thrusters suffer from performance deterioration over time due to grid erosion resulting from heavy ion bombardment. To overcome this limitation, the concept

of a ‘virtual’ cathode was developed in the form of Hall Effect Thruster. The Hall Thruster design uses axial electric and radial magnetic field to ionize the neutrals and trap the electrons at the exit of an annular flow passage. The electric field due to the circulating electrons acts as the cathode and attracts the ions, which exit the thruster with high velocity. As in gridded ion thrusters, the exiting ion beam is neutralized with electrons from a cathode source to avoid net charge buildup (Goebel & Katz, 2008).

A highly miniaturized version of conventional annular Hall thruster has been reported in literature (Ito, Gascon, Crawford, & Cappelli, 2007). The thruster comprises a coaxial design with a 0.5 mm channel width and 4 mm outer diameter. The radial magnetic field was generated using Samarium-Cobalt (SmCo) permanent magnets generating a 0.7 T field at the channel exit. The thruster was able to demonstrate a thrust in the range of 0.6-1.6 mN at a specific impulse in the range of 300-850 s. The power consumption was found to be within 10-40 W, with the anode thrust efficiency limited to 10-15 %.

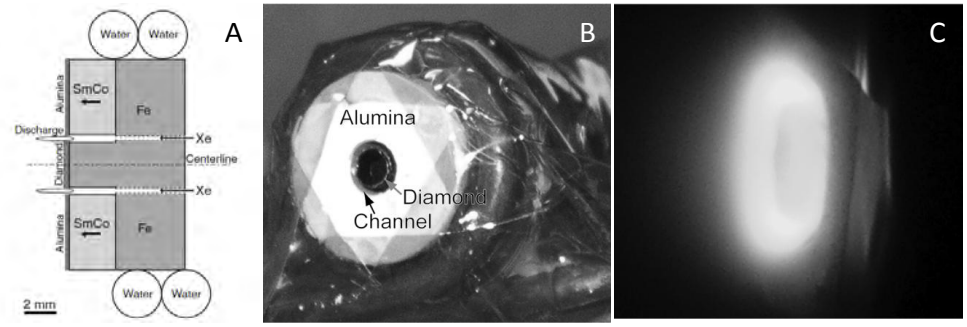

Figure 2-12. Micro Hall thruster. A) Schematic. B) Image of the micro-Hall thruster. C) Prototype micro-Hall thruster in operation (Ito, Gascon, Crawford, & Cappelli, 2007).

Further miniaturization of Hall thruster, however, poses challenges vis-à-vis magnetic field profile, magnetic saturation of the thruster material, and thermal demagnetization resulting from intense heat from ionizing gases. To circumvent these

issues, a modified design for Hall thruster has been developed. This design (Figure 2-13) makes use of a largely axial magnetic field with a small radial component in a cylindrical channel instead of an annular one (Ikeda, Togawa, Nishida, Tahara, & Watanabe, 2011). The cylindrical discharge chamber is 7mm in diameter and length, with the anode located at the upstream end. The largely axial magnetic field is generated by SmCo permanent magnets on the central axis and at the exit plane. The thruster was able to achieve stable operation at powers as low as 10 W operating at 400 V. Thrusts in the range of 0.3 to 3.5 mN at specific impulses ranging from 400 to 1400 s were demonstrated. Thruster efficiency of up to 18% was achieved with this design. This is significantly less than typical values of efficiencies for conventional Hall thrusters (Goebel & Katz, 2008), suggesting performance deterioration with downscaling.

Figure 2-13. Cylindrical Hall effect microthruster. A) Schematic (Polzin, Raites, Gayoso, & Fisch, 2010). B) Prototype 7 mm channel cylindrical thruster. C) Prototype thruster in operation (Ikeda, Togawa, Nishida, Tahara, & Watanabe, 2011).

2.3.2.3 Colloidal Thruster

Colloidal thrusters are a type of electrostatic thrusters, which achieve thrust through acceleration of charged particles, or agglomerations thereof, instead of ionized atoms. The propellant is usually stored in liquid form; however, dry powder propellants

have also been demonstrated. Propellant delivery is often by capillary action or piezo-micropumps.

DRIE fabricated micro-emitters have been developed as part of an electrospray microthruster (Alexander, Stark, Smith, Stevens, & Kent, 2003). An integrated colloid thruster system was devised using 1-butyl1-3-methylimidazolium as propellant, which is an ionic liquid at room temperature. Figure 2-14 shows the thruster assembly, SEM view of the micro-emitter arrays, and the electrospray emanating from a capillary.

A similar design was able to demonstrate thrust ranging between 5 to 500 μN, at a thrust-to-power ratio of 20 μN/W. The thruster could be operated in a low-thrust-high-I_{sp} mode, or a high-thrust-low-I_{sp} mode, with specific impulse approaching 7560 s for the former (Smith, Stark, Krpoun, & Shea, 2009). Colloid thrusters, however, suffer from small lifetimes due to liquid impingement on the extractor electrodes and eventual shorting (Tajmar & Genovese, 2003).

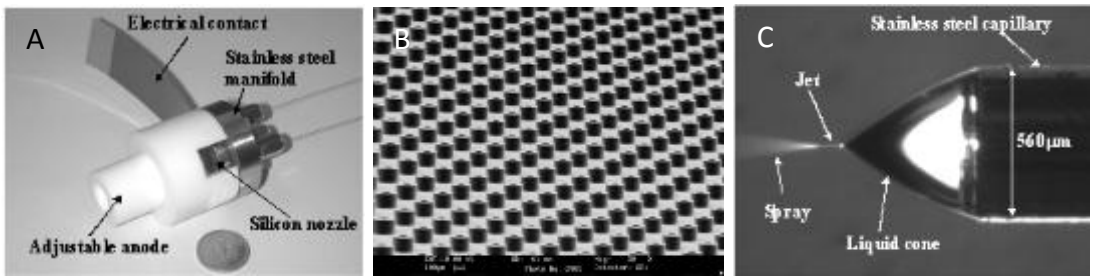

Figure 2-14. Colloidal electrospray microthruster. A) Thruster micro-emitter assembly. B) SEM image of microfabricated emitter array on Si wafer. C) Cone jet and electrospray structure from a stainless-steel emitter (Alexander, Stark, Smith, Stevens, & Kent, 2003).

2.3.3 Electromagnetic Thrusters

The presence of charged particles in electrostatic thrusters opens up the possibility of using magnetic forces to achieve higher acceleration, and hence higher specific impulse. The magnetic field can be externally imposed or can be self-induced

by the plasma current. Teflon blocks have been used as solid propellant in several versions (Rayburn, Campbell, & Mattick, 2005). Such devices are capable of providing very small impulse bits, and offer high total impulse to propellant weight ratio due to compactness of shape resulting from the use of solid propellant. A design utilizing liquid propellant has also been demonstrated (Simon, Land, & Emhoff, 2006). This thruster, called the MILIPULT (Micro Liquid Pulsed Plasma Thruster), was able to produce 0.4 – 0.6 μNs impulse bits using a 1.0 mF capacitor charged at 200 – 700 V. In both the aforementioned designs, however, steady state thrust production is not possible due to inherent design.

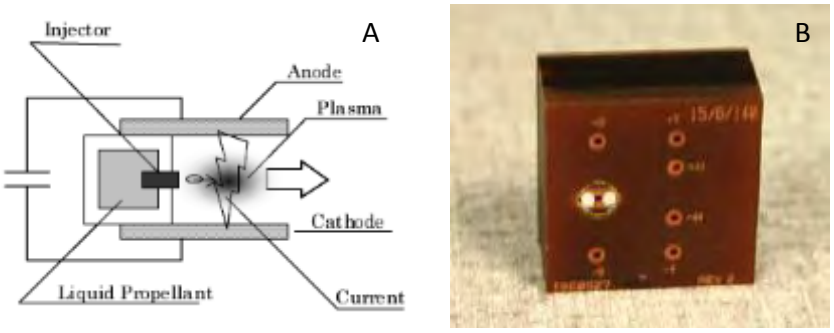

Figure 2-15. Electromagnetic pulsed plasma microthruster. A) Schematic of Liquid Propellant PPT. B) MILIPULT prototype (Simon, Land, & Emhoff, 2006).

The aim of the above survey is by no means to be comprehensive, but to present novel and state-of-the-art technologies being utilized in pursuit of ever smaller thrusters. Few of these designs have actually been commissioned and successfully flown aboard a spacecraft or satellite due to concerns with reliability, weight, power requirements, propellant dispensation, or thrust resolution and repeatability. The demand for a suitable microthruster that can meet the SWaP requirements while avoiding these issues leaves open room for exploring newer concepts and novel ideas. The Free Molecular Electro Jet (FMEJ) thruster being proposed here is just one of these ideas being put forward as a possible alternative to address some of these issues.

CHAPTER 3
GAS DISCHARGES PHYSICS

Dielectric barrier discharges are a class of gas discharges that generate plasma without complete breakdown of the gas. They are, therefore, also called partial discharge. The ionized gas generated by these partial discharge I albeit still *plasma*. Plasma refers to a system of charged particles which demonstrate collective behavior. The term “plasma” was chosen by physicist Irwin Langmuir (Langmuir, 1928) to reflect the similarity with blood plasma, which is composed of two kinds of ‘particles’: the red and white blood cells. In gas plasmas, these two groups are represented by the positive ions and the negative electrons. Real world plasmas, however, are much more generalized and include positive as well as negative ions along with electrons and neutrals. The collective behavior of plasma is largely determined by several physical parameters which are representative of the length and time scales which dictate the nature of plasma interactions. Any understanding of DBDs would be incomplete without understanding these parameters and interactions. These are described at length in subsequent sections.

3.1 Electrical Breakdown in Gases

Plasmas are generated by breakdown of gases at the atomic level, where the electrons are ejected from neutral atoms by energetic photons or electrons. One such mechanism, especially of import to laboratory plasmas, is electrical breakdown by externally applied potential (Raizer, 1987). The mechanism of electrical breakdown can best be described in terms of the current-voltage characteristics of the discharge. Consider a low pressure gas contained in a sealed glass tube with electrodes at either

end as shown in Figure 3-1 inset. The voltage across the electrodes is gradually increased from zero and the resulting current is measured, as plotted in Figure 3-1.

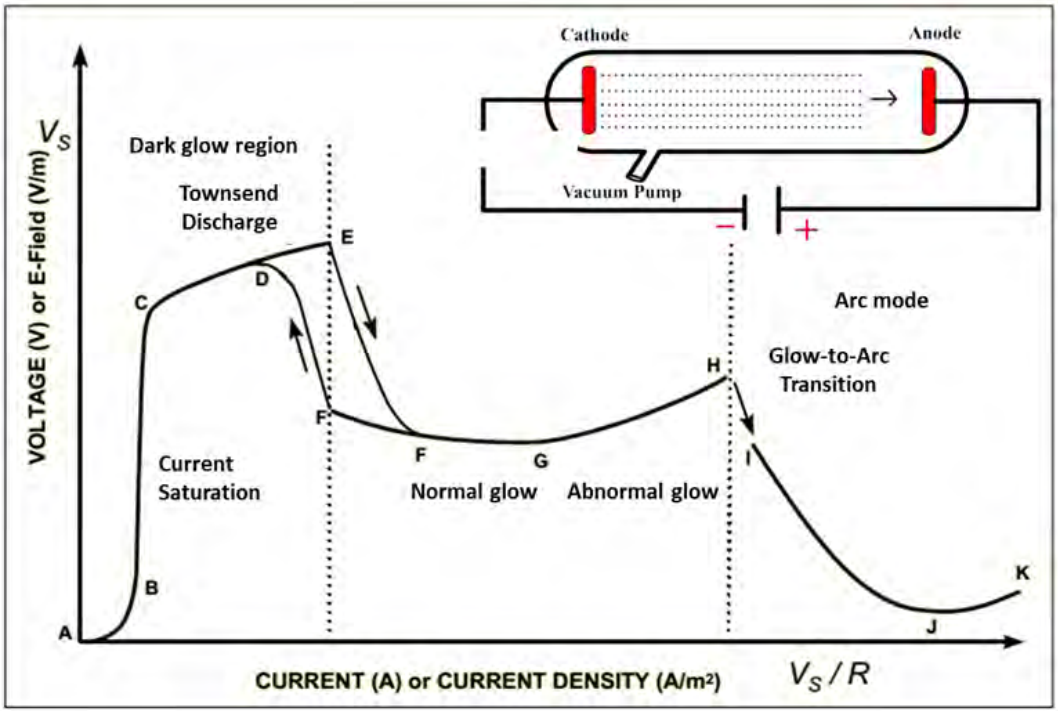

Figure 3-1. VI Characteristics of a DC gas discharge (Roth J. R., 1995).

Even in the absence of electrical breakdown, there is a background population of electrons resulting from photo-ionization by background radiation. In the absence of a driving potential, these free electrons follow random thermal motion, occasionally colliding with the neutrals. When the driving potential is slowly increased, the resulting electric field accelerates the background electrons toward the anode increasing their kinetic energy. As long as the kinetic energy gained is less than the ionization energy of a background neutral, any collision only results in momentum exchange and the electrons have a bulk motion towards the anode in proportion to the applied voltage (A-B). Once the applied potential is high enough to sweep all free electrons towards the anode, the current reaches a saturation value (B) which depends on the intensity of the background radiation producing the electrons. The saturated current barely increases

beyond this point as the voltage is increased. However, once the applied potential is high enough such that kinetic energy gained by the background electrons crosses the threshold ionization energy of the neutrals, the primary electrons create an extra secondary electron through ionizing collisions. The secondary electrons joins the primary electrons and accelerate towards the anode, producing further ionizing events in a process termed as Townsend discharge. The discharge is still dark as the photon density emitted by the plasma is not night enough (B-C). As the voltage is increased further, corona discharge appears at places of non-uniform electric fields such as sharp points and around thin wires. This initially dark discharge eventually becomes visible as the current reaches sufficient levels (D-E). At point E, the voltage is high enough to set off an avalanche of ionization events where each colliding electron produces an extra electron and the two accelerate again to produce further ionizing events. The resulting increase in conductivity due to increased presence of charges carriers results in a rapid increase in current by several orders of magnitude. In this region, the plasma becomes luminous and emits light which is characteristic of the gas present in the discharge tube. After this discontinuous transition (E-F), the plasma enters the normal glow region, which exhibits a negative dynamic resistance, with voltage decreasing slightly with increasing current. At this point, the plasma will try to decrease the electric field at any point by increasing the local charge density, resulting in filaments of plasma. The plasma at this point covers only a portion of the electrode, and keeps the current density constant by covering an increasing portion of the electrode as the current is increased (F-G). At point G, the plasma covers the entire electrode, and enters the abnormal glow region. Once the entire electrode is covered, the plasma can only push more current by

increasing the voltage across the tube, as seen in the region G-H. At point H, the electrode becomes sufficiently hot to emit electrons by thermionic emission, which amplifies the ionization events resulting in highly conducting plasma with a sharp increase in current. The Joule heating from the high current makes the plasma in this region extremely hot with strong light emission in a broad (UV-VIS) spectrum. This is the glow-to-arc transition (H-K), which exhibits changing dynamic resistance with increasing current.

3.2 Plasma Parameters

Plasmas come in a variety of forms, from lab plasmas (Tokamaks), to atmospheric plasmas (Aurora Borealis) to interstellar plasmas (stellar and nebular plasma). Although the essence of these plasmas is same, they differ vastly in their behavior and characteristics. Plasma parameters are physical quantities that help understand and classify the plasma into different regimes, which helps in understanding and modeling their behavior. The three classical parameters used for this purpose are discussed in the following section.

3.2 1 Debye Length

The behavior of solitary a charged particle can be described simplistically by elementary laws. The electrostatic force *F* exerted by a charged particle on another is given by Coulomb's law as (Griffith, 2012)

$$F_{Coulomb} = \frac{1}{4\pi\varepsilon_0}\frac{q_1 q_2}{r^2} \tag{3-1}$$

where q_1 and q_2 are the charge of the two particles, and r is the distance separating them. This force can be seen as arising from the interaction of the second particle with the force "field" of the exerting particle, called the electric field. This field

can be thought of arising from an electric potential φ which can be formulated as (Griffith, 2012)

$$\phi = \frac{1}{4\pi\varepsilon_0}\frac{q_1 q_2}{r} \tag{3-2}$$

The expression suggests an inverse decay of the potential with distance. The potential field of a particle in collective plasma, however, displays a deviation from this decay rate due to the phenomenon known as ‘shielding’. Shielding essentially involves the cancellation of the electric field of a particle by the electric field of an oppositely charged particle that it attracts.

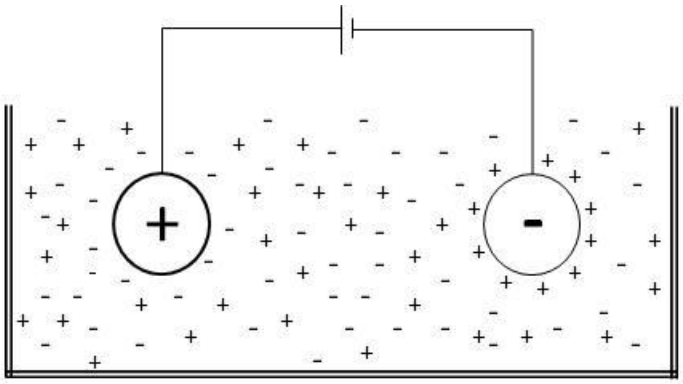

Figure 3-2. Illustration of Electrostatic Shielding in a Plasma.

Consider a positively charged sphere. In the absence of external plasma, the sphere would exert an electric field decaying as per the inverse square law. However, when this sphere is immersed in a plasma, the negative particles (electrons) are attracted towards it and the sphere is surrounded by a cloud of electrons (Figure 3-2). This electron cloud exerts its own electric field, opposite in direction of the field of the positive sphere, thus weakening it. Analysis suggests an exponential decay of the positive field due to the electrostatic shielding by the electron cloud, which is given as (Goebel & Katz, 2008)

$$\phi = \frac{e}{4\pi\varepsilon_0 r}\exp\left(-\frac{r}{\lambda_D}\right) \tag{3-3}$$

Figure 3-3 compares the potential field from a positively charged particle with and without shielding. The length scale over which this exponential potential decay takes place is called the Debye length, λ_D.

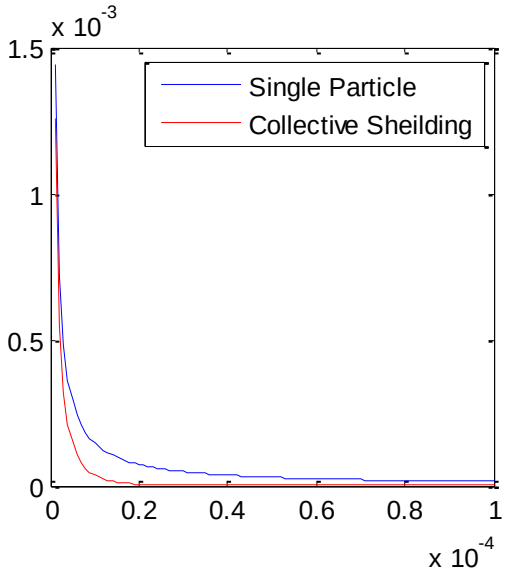

Figure 3-3. Potential distribution around a charged particle with and without shielding (T_e =1 eV, n_e = 10^{18} m^{-3}).

Debye length is one of the fundamental plasma parameters which provide an insight into physical quantities like plasma density and temperature. The Debye length depends on physical quantities such as electron and ion temperatures and densities. However for most plasmas the electron Debye length is the smaller length scale due to higher electron mobility; hence, it is often expressed in terms of electron density n_e and temperature T_e as

$$\lambda_D = \sqrt{\frac{\varepsilon_0 k_B T_e}{n_e q_e^2}} \tag{3-4}$$

This relationship suggests a hotter plasma will have a longer Debye length, which results from the fact that hotter electrons will be able to escape the electrostatic pull to a higher distance, thus 'diffusing' the effect of shielding and hence extend the Debye region. A higher electron density lends itself to stronger shielding on account of higher charge density, thus shortening the Debye length. Table 3-1 below provides representative values of Debye length for plasma found in different situations.

Table 3-1. Debye length scales for different types of plasma (Goldston & Rutherford, 1995)

Plasma	Density $n_e(m^{-3})$	Electron temperature $T_e(K)$	Debye length $\lambda_D(m)$
Solar core	10^{32}	10^{7}	10^{-11}
Tokamak	10^{20}	10^{8}	10^{-4}
Gas discharge	10^{16}	10^{4}	10^{-4}
Ionosphere	10^{12}	10^{3}	10^{-3}
Magnetosphere	10^{7}	10^{7}	10^{2}
Solar wind	10^{6}	10^{5}	10
Interstellar medium	10^{5}	10^{4}	10
Intergalactic medium	1	10^{6}	10^{5}

3.2.2 Plasma Frequency

While the interaction length scales in a plasma are determined by Debye length, the time scales are governed by a similar parameter called the Plasma Frequency. The concept of plasma frequency can be elucidated by considering a slab of plasma at equilibrium. In this equilibrium configuration the plasma is 'quasi-neutral', that is to say the net electric field by the positive species is effectively cancelled out by the negative species, resulting in a zero electric field inside the plasma. Now if all the particles of one

species, say electrons, are displaced by a small distance, this deviation from their equilibrium position creates a net electric field. The resulting electrostatic force from the residual field tries to pull the slab of electrons back to their equilibrium position. The ions are considered relatively stationary due to their higher mass and resulting inertia, being over 3 orders of magnitude higher than the electrons. The electrons that are accelerated back to the starting position overshoot it owing to inertia and are set in an oscillating motion. The frequency at which this oscillation takes place is characteristic of the plasma and is called the plasma frequency. The plasma frequency is found to be solely a function of the electron number density n_e, given as (Goebel & Katz, 2008)

$$\omega_{pe} = \sqrt{\frac{n_e e^2}{\varepsilon_0 m_e}} \tag{3-5}$$

where e is the elementary charge and m_e is the electron mass, and ε_o is the permittivity of free space.

Plasma frequency is a measure of plasma timescales, and dictates the speed at which an electromagnetic disturbance can travel through the plasma. If the disturbing field is oscillating at a frequency larger than the plasma frequency, the plasma essentially does not have enough time to respond for the signal to propagate. Plasma frequency explains a lot of the phenomenon related to propagation of electromagnetic waves such as reflection of radio waves in the Ionosphere. The plasma density in the ionosphere determines the plasma frequency at a particular altitude, which determines the upper limit of the signal frequency that can penetrate the region. Signals of higher frequency are reflected by the ionosphere, a fact that is utilized in the transmission of radio waves across the globe by Ionospheric reflection. Plasma frequency also explains the communication blackout experienced during the re-entry of space-faring vehicles

such as the Space Shuttle. The intense heat around the Space Shuttle ionizes the air around the vehicle, which shields the communication frequencies from ground stations.

3.2.3 Number of Particles in Debye Sphere

Along with the length and timescales, another important plasma parameter that determines whether a collection of charged particles can be treated as a plasma is the number of particles in the Debye sphere, N_D, defined as

$$N_D = 4\pi n \lambda_D^3 \tag{3-6}$$

where n is the plasma number density

3.3 Three Requirements for Plasma

As mentioned earlier, the behavior of a collection of particles is different from an isolated one due to interparticle interaction and the tendency of the plasma to neutralize any electric fields arising within it. This collective behavior lends itself continuum-like models for understanding and predicting plasmas. Much like continuum treatment of fluids which depends on satisfying the minimum density criterion via the Knudsen number, the collective treatment of plasmas also necessitates certain conditions to be present. For a system of charges particles to be treated collectively as a plasma, the following requirements must be met (Chen, 1984):

- $L >> \lambda_D$

  The region within the Debye length consists of higher density of one charged species over another, resulting in a net charge within. The condition of quasi-neutrality no longer holds valid in this region due to this charge separation. Since continuum treatment of plasma relies heavily on the quasi-neutrality assumption, the characteristic length of the plasma L should be much greater than the Debye length for collective treatment to hold over majority of the plasma domain.

- $\tau >> 2\pi/\omega_{pe}$

  For electrostatic interactions to dominate so that the systems is more than just a gas, the timescale of these interactions should be much shorter than the collision

timescales which dictate the gas-like characteristics of a system of particles. This requires that the plasma frequency be much greater than the electron-neutral collision frequency τ.

- $N_D >> 1$

  This requirement is called the plasma approximation. It arises from the fact that the quintessential electrostatic shielding phenomenon that defines collective plasma behavior arises only in the presence of multiple particles. A single particle cannot exert enough influence to shield the potential fields. This requires that charged particles interact with multiple particles in its vicinity instead of the nearest particles. The characteristic length in plasma being the Debye length, it's natural that this criteria is presented as the number of particles inside a 'Debye sphere', and that the number of particles in this sphere be much greater than unity.

3.4 Plasma Particle Interactions

Inter-particle interactions in a plasma take place through a multitude of mechanisms. Interactions between charged particles are predominantly governed by electrostatic forces between the species, whereas charged and neutral species predominantly interact via interatomic and molecular forces. Depending on the plasma regime, collision process can influence and even dominate diffusion, mobility and resistivity of particle species (Franz, 2009).

The collision frequency between two species is determined by the relative velocity and the collision cross section, which is a function of the relative velocity. For instance, the ionization cross section of electron on Xenon (a common propellant) is found to be a strong function of the electron energy as evident from Figure 3-4 below.

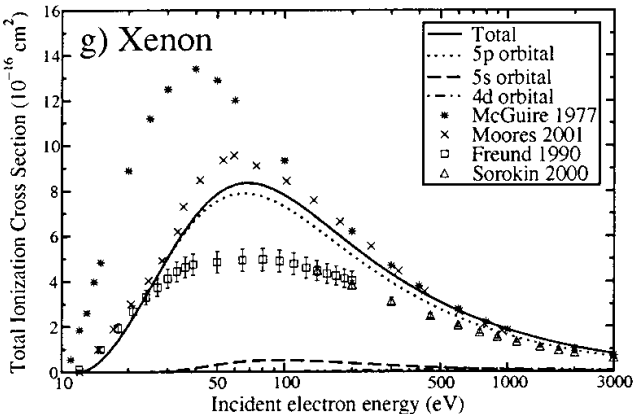

Figure 3-4. Variation of Xenon ionization cross-section with electron energy (Bartlett & Stelbovics, 2002).

The collision frequency can be deduced from the concept of mean free path, which is the distance a relatively fast moving particle travels before colliding with a particle of another species. The mean free path is given as

$$\lambda = \frac{1}{n_a \sigma} \tag{3-7}$$

The collision frequency and the time between collision can be deduced from this based on the average velocity of the particle as

$$\nu = \frac{1}{\tau} = n_a \sigma \bar{v} \tag{3-8}$$

In the particular case of electron-neutral collisions, using the relevant parameters and the definition of average velocity gives the expression for electron-neutral collision frequency as (Goebel & Katz, 2008)

$$\nu_{en} = \sigma_{en}\left(T_e\right) n_a \sqrt{\frac{8kT_e}{\pi m}} \tag{3-9}$$

The energy dependent collision cross section $\sigma_{en}(T_e)$ is often determined by experimental or numerical methods.

Interaction between charged species depends on a multitude of factors including the relative velocity and impact parameter, as detailed in the Rutherford scattering model (Goldston & Rutherford, 1995). Relevant treatment suggests electron-ion collision frequency is given by (Goebel & Katz, 2008)

$$\nu_{ei} = 2.9\times10^{-12}\,\frac{n_e \ln\Lambda}{T_{eV}^{3/2}} \tag{3-10}$$

where *ln* Λ is the Coulomb logarithm which takes into account the difference in effectiveness of large angle collisions as against small angle interactions. The Coulomb logarithm can be approximated as (Goebel & Katz, 2008)

$$\ln\Lambda = 23 - \frac{1}{2}\ln\left(\frac{10^{-6} n_e}{T_{eV}^{3/2}}\right) \tag{3-11}$$

In similar vein, electron-electron collision frequency can be estimated as (Goebel & Katz, 2008)

$$\nu_{ee} = 5\times10^{-12}\,\frac{n_e \ln\Lambda}{T_{eV}^{3/2}} \tag{3-12}$$

while the ion-ion collision frequency is given as (Goebel & Katz, 2008)

$$\nu_{ii} = Z^4\left(\frac{m}{M}\right)^{1/2}\left(\frac{T_e}{T_i}\right)^{3/2}\nu_{ee} \tag{3-13}$$

Various bulk plasma properties can be modeled based on interparticle interaction such as collision. An example is the electrical resistivity of plasma, which can be derived from the collisional dynamics. Using the steady-state momentum conservation equation, the resistivity of the plasma can be expressed as (Goebel & Katz, 2008)

$$\eta = \frac{m\left(\nu_{ei} + \nu_{en}\right)}{e^2 n} \tag{3-14}$$

For fully-ionized plasma ($v_{en} = 0$), the resistivity can be expressed in terms of plasma frequency as (Goebel & Katz, 2008)

$$\eta_{ei} = \frac{m\nu_{ei}}{e^2 n} = \frac{1}{\varepsilon_0 \tau_{ei} \omega_p^2} \tag{3-15}$$

3.5 Thermal Classification of Plasma

The temperature of a gas is a measure of the kinetic energy of its constituent particles. The randomized motion of the atoms and molecules forms the very basis of energy transfer and thermalization through collisions. Under equilibrium conditions, the particle velocities follow the Maxwellian distribution where the number of particles of a gas at temperature T that have velocities between v and $v+dv$ is given as (Goldston & Rutherford, 1995)

$$dn = 4\pi n \left(\frac{m}{2\pi kT} \right)^{3/2} \exp\left(-\frac{mv^2}{2\pi kT} \right) v^2 dv \tag{3-16}$$

where n is the total gas density, k_B is the Boltzmann constant, and m is the mass of the constituent particle.

Statistical considerations demonstrate that the number of particles of a gas with certain energy can be determined from the Boltzmann distribution, given as

$$n_i = n_0 g_i A e^{-\frac{E_i}{kT}} \tag{3-17}$$

where n_0 is the total number density, n_i is the number density of particles with energy E_i and degeneracy g_i (number of energy states with same energy), and T is the gas temperature. Particles of a given energy level are constantly created and removed by various processes (excitation and relaxation through particle or photonic collisions). Under equilibrium, the rate of creation and removal are exactly balances such that the aggregate density of particles in a particular energy state remains constant.

Plasma, being a mixture of different species, can contain several positive and negative species. Generally the predominant negative species is the electrons, and there could be several positive species depending on the composition and conditions of the gas that constitutes the plasma. In the most general case, each species could have its own unique Maxwellian energy distribution, which defines its temperature. For example in DBD plasma, the electrons are found to be at a temperature of several eV whiles the ions are generally 'cold', i.e. at room temperature. This leads to a condition where different plasma species are not in thermal equilibrium with each other. A multitude of factors determine if this occurs, such as insufficient thermalization through collision and radiation among different species. Accordingly, plasmas are generally classified in several thermal categories.

3.5.1 Complete Thermal Equilibrium (CTE)

A plasma in CTE is characterized by equilibrium of temperature and radiation. This equilibrium results in the radiation having a blackbody spectrum at the plasma temperature, characterized by Plank's Law (Friedman & Kennedy, 2011)

$$\rho(\upsilon,T)=\frac{8\pi h\upsilon^3}{c^3}\frac{1}{e^{\frac{h\upsilon}{kT}}-1} \tag{3-18}$$

Here $\rho(\upsilon,T)$ is the spectral energy density at wavelength υ and temperature T, c is the speed of light, and h is the planks constant. The plasma species are at the same corresponding blackbody temperature. For the plasma to be in complete equilibrium, all radiation that is produced by various processes must be absorbed by the plasma. This radiation equilibrium requires the mean free path of radiation absorption to be larger than the characteristic dimension of the plasma. This requirement is not realized in laboratory plasmas, which are generally optically thin. CTE can only be approximated in

a large plasma volume where the central part is homogenous and does not sense the boundaries. The Solar corona is an example of CTE plasma.

3.5.2 Local Thermodynamic Equilibrium (LTE)

Since optical opaqueness is the only restriction that is impossible to meet to attain CTE in laboratory plasmas, such plasma are often modeled as being under LTE. LTE allows for spatial variations in temperature to account for different levels of radiation loss in the central region and the boundaries, and the transport of species across the plasma volume. (Miziolek, Palleschi, & Schechter, 2006) The plasma species are, however, expected to be in thermal equilibrium locally. This means that the collisional processes have to balance out to maintain partition functions and distributions. Note that this equilibrium temperature itself is allowed to evolve in time, but at any given instance, different plasma species are expected to be in thermal equilibrium locally. The domination of collisional processes to achieve equilibrium conditions requires a minimum electron number density given as (Griem, 1964)

$$n_e > 9.1\times10^{17}\left(\frac{E_2}{E_{ionization}}\right)^3\left(\frac{kT}{E_{ionization}}\right)^{1/2} \tag{3-19}$$

3.5.3 Partial LTE

When the electron densities in a plasma are not high enough to satisfy the LTE conditions, the radiative transitions play an important role as they are responsible for triggering the overpopulation of energy levels. One instance could be where the electron density is lower than the criteria for the lowest energy level, for which $E_{ionization}$ is high. In such cases, the kinetic energies of electrons and heavy particles can be different. However, like LTE, PLTE also requires a minimum electron density to be maintained, as given by (Hotinceanu, Borsos, & Dinu, 2010)

$$n_e > 7\times10^{18}\left(\frac{Z^6}{n^{\frac{17}{2}}}\right)\left(\frac{kT}{E_{ionization}}\right)^{1/3} \quad (3\text{-}20)$$

An example approach to modeling PLTE involves ground state neutrals not in equilibrium with the continuum radiation temperature while the electron and ion temperatures are allowed to be different (Kroesen, Schram, Timmermans, & De Haas, 1990).

3.5.4 Non-Thermal Plasma

When the mechanisms responsible for thermalization are insufficient such that none of the species are in equilibrium with each other or with the continuum radiation, the plasma is said to be non-thermal. This type of plasma is the hardest of model due to failure of some basic assumptions that are often used to model the collective behavior. Dielectric barrier discharge is a good example of such plasmas, with electron and ion temperatures often differing by orders of magnitude (Biganzoli, Barni, Riccardi, Gurioli, & Pertile, 2013).

3.6 Degree of Ionization

The process of converting a neutral gas into a plasma proceeds through a multitude of mechanisms and chain reactions, the primary one being Townsend mechanism. However, under certain conditions, there may not be enough free electrons or with high enough energy, such that not all the neutral particles in the gas are ionized. In this case the equilibrium plasma consists of electrons, ions, and neutrals. The relative concentrations of the charged and uncharged species determine the degree of ionization of the plasma, defined as

$$I = \frac{n_i}{n_i + n_n} \tag{3-21}$$

where n_i and n_n represent ion and neutral densities respectively. Statistical treatment of such a system of charged particles suggests that in a weakly ionized plasma, the equilibrium composition of the plasma can be expressed as (Friedman & Kennedy, 2011)

$$\frac{n_{i+1} n_e}{n_i} = \frac{2}{\Lambda^3} \frac{g_{i+1}}{g_i} \exp\left[-\frac{\left(E_{i+1} - E_i\right)}{k_B T} \right] \tag{3-22}$$

where *i* denotes the state of ionization, *n* the number density of the i^{th} state, *g* the degeneracy, *E* the energy, *T* the equilibrium temperature of the plasma, and Λ the electron de-Broglie wavelength. For a system with only singly ionized particles, the degree of ionization in terms of the total number of particles *n* can be expressed as

$$\frac{n_e^2}{n - n_e} = \frac{2}{\Lambda^3} \frac{g_1}{g_0} \exp\left[-\frac{\Delta E}{k_B T} \right] \tag{3-23}$$

where ΔE is the ionization energy. Table 3-2 provides the ionization energies of some common propellants, along with atomic mass, for reference.

Table 3-2. First ionization energies and atomic mass of common propellants (Kieckhafer & King, 2007).

Propellant	First Ionization Energy (eV)	Mass (amu)
Bismuth	7.3	209
Cadmium	9.0	112.4
Cesium	3.9	132.9
Iodine	10.4	126.9
Krypton	14.0	83.8
Mercury	10.4	200.6
Xenon	12.1	131.3

The knowledge of plasma parameters, interactions, and degree of ionization helps one classify and understand plasma behavior. Measurement of plasma physical quantities (densities, temperatures) can be made using intrusive (Langmuir probes) or non-intrusive (optical emission spectroscopy) methods, which reveals the regime the plasma is operating in. Based on this knowledge, appropriate assumptions can be applied to treat the plasma or to develop simplified models to describe the plasma and plasma-dependent processes, such as the transfer of momentum to neutrals in a DBD actuator. The variation in plasma physical quantities also throws light on trends in observed bulk quantities such as induced flow and force in case of DBD actuators.

CHAPTER 4
DIELECTRIC BARRIER DISCHARGE ACTUATORS

The FMEJ concept is based on the principle of DBD actuation. A general understanding of DBD actuators is necessary for any intended design optimization of a thruster using these actuators. To this end, the following sections provide a brief overview of the principle, characteristics, and applications of plasma actuators to aid better understanding of the device.

4.1 Dielectric Barrier Discharge

Dielectric barrier discharges (DBDs) are plasma generated between two electrodes separated by an insulating dielectric such as air (Figure 4-1). Also called partial discharges since they do not result in a complete electrical breakdown resulting in a direct current path in the dielectric, DBDs are a form of localized electrical breakdown. In air, such a discharge manifests itself as a visible discharge, called the Corona discharge, bluish in color and accompanied by a characteristic hum. The physical mechanism responsible for the discharge is the Townsend mechanism, whereby a free electron, accelerated by a strong electric field, triggers an avalanche multiplication by impact ionization. This results in an ionized region that extends a finite distance from the electrode surface but is not strong enough to form a plasma arc.

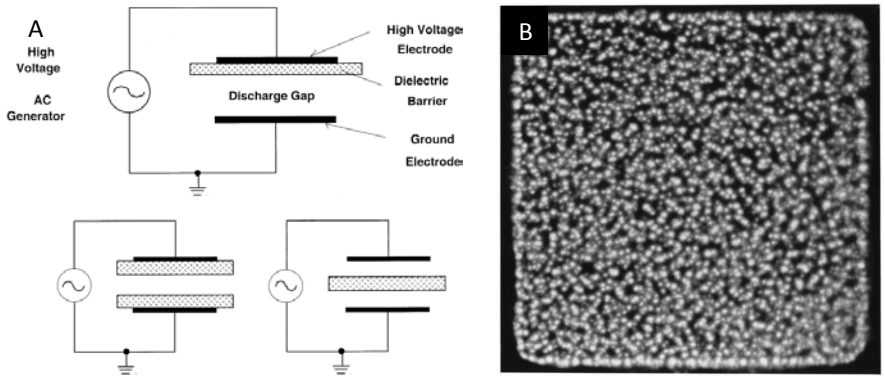

Figure 4-1. Dielectric Barrier Discharges. A) Arrangement of a DBD device. B) Visible characteristics of the microdischarges (Kogelschatz, 2002).

The visible characteristics of a dielectric barrier discharge are short lived micro discharge filaments that occur in large numbers (Kogelschatz, 2002). At atmospheric pressures, electrons accelerated by a strong electric field can generate an appreciable charge separation at the tip of the microdischarge due to different drift velocities of electrons and ions. The electric field resulting from this charge separation is superimposed on the applied electric field, resulting in a high field region, typically about 10 μm thick. The propagation speed of these microdischarges is of the order of 10^5-10^6 m/s with a radius of about 0.1 – 1 mm. Once the discharge has bridged the electrode gap, it deposits its charge on the dielectric, leading to a local collapse of the electric field at the spot. The entire process from the streamer initiation to quenching takes a few nanoseconds, with the transferred charge of no more than 100s of pC. The short time and space scales mean the energy deposited in the process is typically no more than a few μJ, which prevents the domination of thermal energy modes, thus arresting the temperature increase to only a few Kelvin. (Kogelschatz, 2002)

Dielectric barrier discharges essentially provide a means of generating cold, non-equilibrium plasmas at atmospheric pressures. This has led to the use of these discharges for a number of industrial applications, such as ozone production, surface modification, treatment of pollution gases, CO_2 lasers and excimer lamps, and flat screen plasma display screens (Kogelschatz, 2003)

4.2 DBD Actuators

4.2.1 Actuator Concept

The use of dielectric barrier discharge to induce a flow/force was conceived over a decade ago (Roth, Sherman, & Wilkinson, 1998). The idea involves asymmetrically placed electrodes on either side of a dielectric driven by an alternating voltage of

several kilovolts at kilohertz frequencies. The ground electrode is encapsulated to prevent plasma formation since plasma is desired only at the powered electrode. Figure 4-2 shows a schematic of such an arrangement.

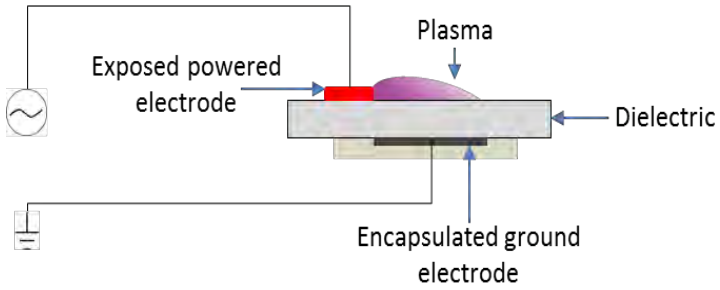

Figure 4-2. Typical arrangement of a DBD plasma actuator.

Initial results demonstrated that such an arrangement could induce wall jets along the actuator surface, originating at the downstream edge of the powered electrode extending along the width of the ground electrode (Roth J. R., 2000). Investigations into the velocity profile of the wall jet revealed that bulk of the inducement was taking place within the visible glow discharge. The strength of the wall jet was found to be a function of electrical and geometrical parameters, which will be discussed in a subsequent section.

4.2.2 Actuator Physics

The physical phenomena taking place in a DBD actuator manifest themselves in several forms. The glow discharge gives the first clue about the energy conversion process taking place by means of ionization. Time resolution of the nature of the glow reveals a dynamic relationship between the driving signal and the observed glow (Orlov, 2006). Figure 4-3 shows the time-resolved output from a photomultiplier tube aimed at the discharge location and the time-resolved input signal profile. It was observed that there is a strong correlation between the qualitative nature of the discharge and the

signal phase. Firstly, the discharge does not take place over the entire cycle, but is present only for a finite fraction of the half cycle the signal is in. Secondly, for the positive half of the cycle, the discharge shows few but strong light emissions corresponding to individual microdischarges, while for the negative half of the cycle, the character is weaker but more frequent.

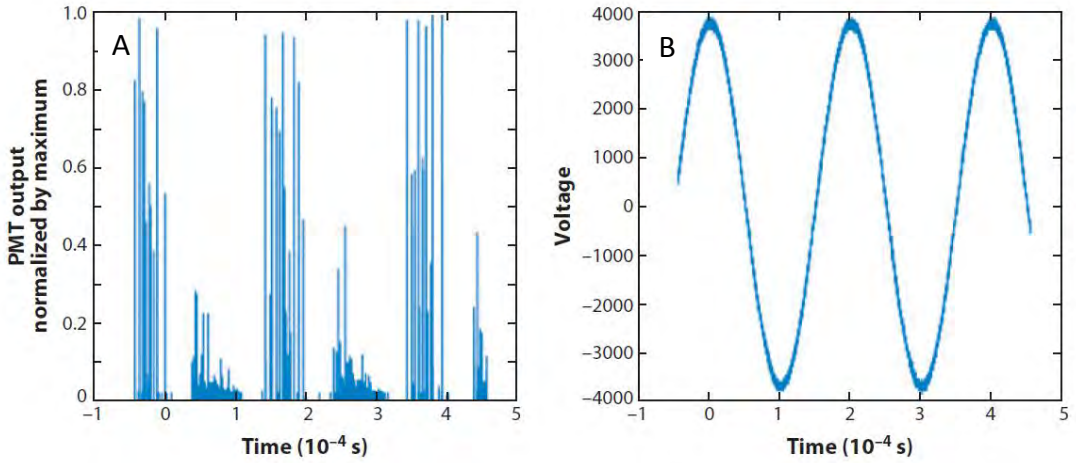

Figure 4-3. DBD microdischarge light emission characteristics. A) Time-resolved normalized output from the photomultiplier tube. B) Driving voltage signal (Corke, Enloe, & Wilkinson, 2009).

The physical mechanism responsible for this asymmetrical behavior of the discharge has to do with electron emission and transport. During the negative half of the cycle, the exposed metal electrode readily emits electrons, which travel towards the ground electrode, but get obstructed by and deposited on the dielectric surface. The deposition of electrons at the surface results in a sheath phenomenon, whereby a charge separation region is created in the proximity of the surface resulting in electrostatic screening of the ground electrode. This screening effect results in a self-arresting nature of the discharge, where the applied electric field is cancelled by the superimposed field created by the charge-separated region. During the positive half cycle, the deposited electrons travel back to the exposed electrode and are readily

absorbed by the metal conductor. Moreover, the dielectric, being an insulator, does not readily give off electrons, resulting in fewer but strong microdischarges. This corroborates well with the time-resolved visual observations obtained using high-speed photography (Enloe, et al. 2008), reproduced below in Figure 4-4.

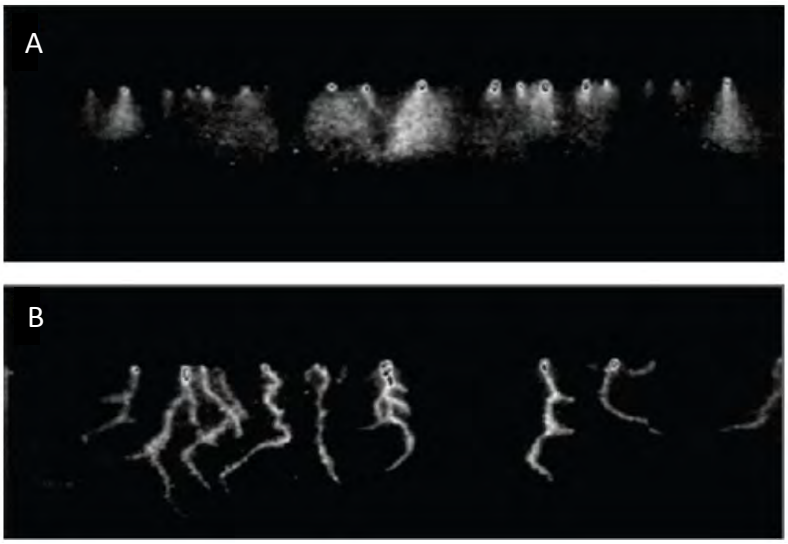

Figure 4-4. Visual characteristics of the microdischarge streamers. A) During the negative-going part of the cycle. B) During positive-going part of the cycle (Enloe, Font, McLaughlin, & Orlov, 2008).

The exact mechanism of force production was a subject of debate, and numerous investigations, experimental and numerical, have led to an increased understanding of molecular level phenomena. Numerical simulations (Font, 2000; Font & Morgan, 2005) suggested that during the positive half-cycle, there is a net momentum away from the exposed electrode and towards the dielectric, while during the negative half-cycle, the net momentum switches direction (dubbed the *PUSH-pull* scenario). The forward (directed downstream) momentum was significantly larger in magnitude than the reverse momentum, resulting in a net time-averaged force in the downstream direction. Experimental investigations using time-resolved Doppler (Forte, Jolibois, Moreau, Touchard, & Cazalens, 2006) and particle velocimetry (Kim, Do, Mungal, &

Capelli, 2007), however, revealed a scenario where the velocities do differ in magnitude over the two half-cycles, but not in direction (*PUSH-push* action). Recent investigations using time-resolved PIV revealed that positive sawtooth and square waveforms indeed exhibit a *PUSH-pull* action, whilst negative sawtooth elicited a *PUSH-none* forcing response (Kotsonis & Ghaemi, 2011). In any case, the transfer of momentum from few charged particles (ions and electrons) to the bulk of the flow is known to take place primarily via ion-neutral collisions, since the electron momentum transfer cross section is significantly smaller. Despite the limited understanding of the physics behind the force production mechanism, significant progress has been made in quantitative understanding of the relation between the induced force and the various parameters (voltage, frequency, geometry, gas composition etc).

4.2.3 Actuator Applications

The flow and force inducement capability of DBD actuators has opened up the possibility of their application in the field of flow control. All real-world flows exhibit the boundary layer phenomenon, which is a manifestation of viscous interactions. With no-slip condition at the wall imposing a zero velocity constraint, the flow over a surface exhibits a boundary later phenomenon. This layer, over which the flow adjusts itself to the wall and freestream boundary conditions, continues to grow downstream until momentum dissipation by viscous interactions overpowers the inertial forces, and the laminar nature of the flow is disrupted. Instability mechanisms (Tollmien–Schlichting wave being one of several) lead to the disruption of flow structure, leading to a transition to turbulence. The adverse pressure gradients resulting from turbulence ultimately lead to flow separation, leading to unfavorable aerodynamic conditions such as high drag, loss of lift, and stall (Schlichting, 2000).

Since separation generally results from loss of momentum by viscous dissipation, efforts to alleviate it generally aim at compensating for the lost momentum. These include synthetic jets, which inject momentum into a decaying boundary layer by physically adding high momentum fluid to achieve stability and delay transition (You & Moin, 2008). This principle is also reaped as an added benefit in film cooling. One main drawback of synthetic jet flow control is the lack of sufficient control authority in the amount of momentum added to the boundary layer. Control of mass flow rates through the jets generally requires moving components (Gimeno, et al., 2010). The machining of holes also compromises the structural integrity of the airfoil, especially in components that are under unusually high thermal and structural loads, such as turbine blades.

The ability of DBD actuators to induce wall jets has offered an alternative to synthetic wall jets for flow control. These actuators have several distinct advantages over synthetic actuators:

- Lack of moving parts. Flow control can be switched on and off using an electrical signal. No moving parts (such as valves) are required to activate flow control. DBD actuators also do away with the need of bleeding or diverting the main flow to feed the synthetic jet actuators.
- Versatility of design and geometry: Actuators with different geometries and shapes (linear, serpentine, dots) have been designed and tested. These designs can be customized to achieve different objectives.
- Scalability: Actuators with a wide range of lengths (0.01 – 1m) and dielectric thicknesses (10 μm – 10 mm) have been tested successfully, providing a range of flow/force options along with a wide range of thrust/weight ratios.
- Versatility of control authority: The performance of DBD actuators can be fine-tuned merely by varying the operating voltage, frequency, waveform, or duty-cycle once the geometry has been fixed.
- Surface compliance and structural integrity: Actuators can be flush-mounted on the surface. They do not need provision for holes/slits that can compromise structural integrity of the component.

The efficacy of DBD actuators for different applications has been reported in literature, and some of those applications are summarized below.

4.2.3.1 Separation control

DBD actuators have been used for flow separation control over airfoils. Several researchers have reported successful results in using DBD actuators to delay separation or reattach separated flow (Roupassov, 2008; Post & Corke, 2004a; Post & Corke, 2004b; Moreau, 2007; Corke, Mertz, & Patel, 2006; Huang, Corke, & Flint, 2006; Post & Corke, 2006). The application generally involves a linear actuator installed in a span-wise direction, whereby the induced velocity is in the downstream direction. Figure 4-5 shows the application of plasma actuator for separation control behind a bluff body (Thomas, Kozlov, & Corke, 2008). As evident, momentum addition at the separation point using a plasma actuator successfully reattaches the flow and pushes the separation point further along the circumference. Similar results have been demonstrated over airfoils in the aforementioned publications.

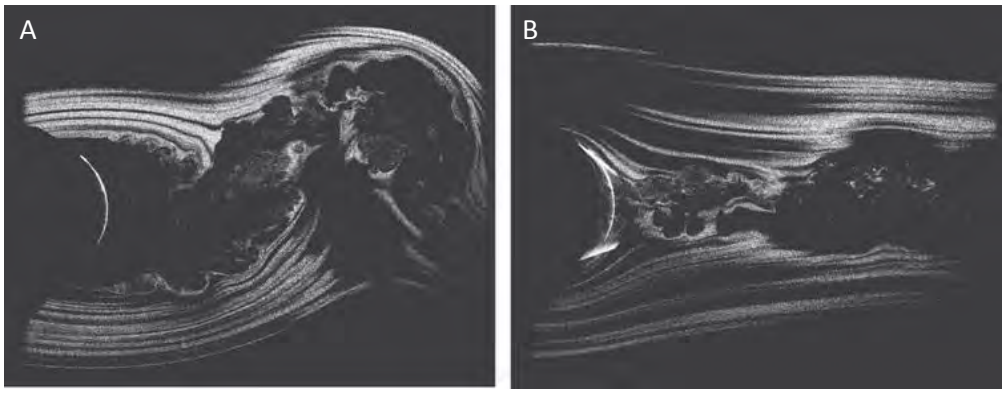

Figure 4-5. Bluff body separation control using plasma actuation. A) Plasma off. B) Plasma On (Thomas, Kozlov, & Corke, 2008).

4.2.3.2 Flow shaping and mixing

The use of serpentine DBD actuators to achieve localized out-of-plane velocity changes have been reported in literature. Numerical simulations indicate that the

serpentine actuators create areas of localized ‘pinching’ and ‘spreading’ (Roy & Wang, 2009). Experimental investigations, as presented in Figure 4-6, corroborated these predictions, with serpentine actuators generating complex 3D vortical structures and adding momentum in all three dimensions, resulting in rapid mixing (Durscher & Roy, 2012). These results open up the possibility of using serpentine plasma actuators in combustion processes to facilitate better mixing of fuel-oxidizer mixtures (Wang & Roy, 2011).

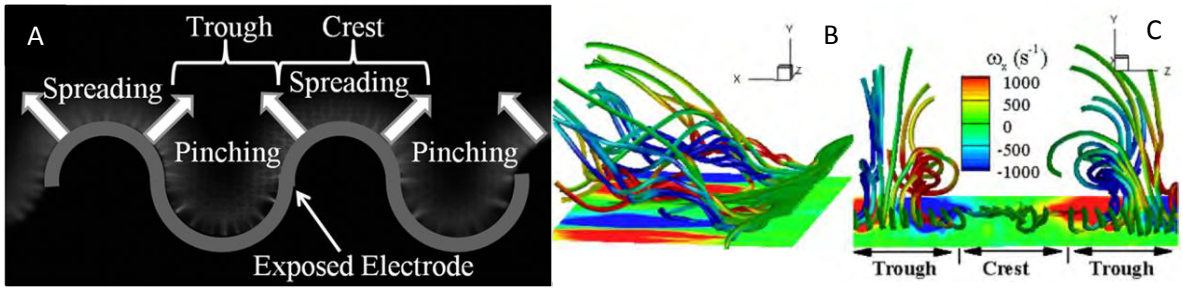

Figure 4-6. Serpentine plasma actuators. A) Layout of a serpentine actuator. B,C) Stream traces (colored by vorticity contours) showing complex three-dimensional structures (Durscher & Roy, 2012).

4.2.3.3 Micropumps

Conceptual designs of plasma actuator based micropumps have been investigated in literature. One such study (Wang & Roy, 2009) numerically investigated a design with an overall envelop of no more than a few mm^3. Results indicated flow rates of the order of a few ml/min could readily be achieved by such a design. The main advantages of plasma based micropumps are rapid on/off capability, absence of moving parts which increases reliability, and small footprint. Intended applications for such a device could be cooling of microelectronic circuits and propellant pumping for micropropulsion thrusters. Figure 4-7 provides the details and results for these simulations.

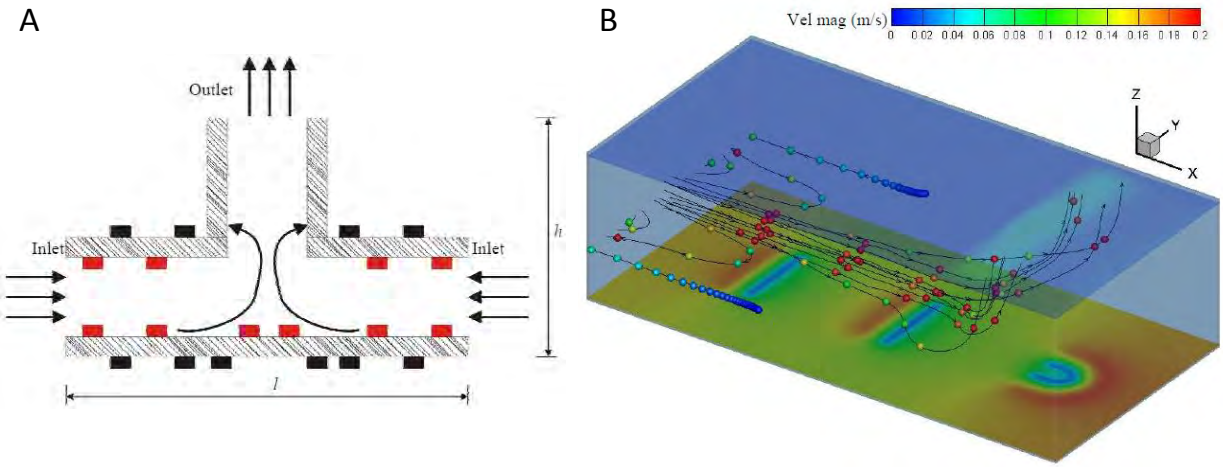

Figure 4-7. Plasma actuator based micropump. A) Schematic of such a pump. B) Velocity magnitude contours from numerical simulation (Wang & Roy, 2009).

4.2.3.4 Plasma velocity sensor

It has been observed that the power dissipated in a plasma actuator in a freestream flow depends upon the freestream velocity. This opens up the possibility of extracting information about the flow over a plasma actuator based on observed power consumption. One such device (Matlis & Corke, 2005) utilizes a plasma actuator with a 0.076mm gap powered at 350 V_{rms}. The device has demonstrated measurement capability at speeds up to Mach 5 and frequency response of up to 200 kHz. Later developments (Matlis, Corke, Cameron, & Morris, 2008) demonstrated its sensitivity for low-speed flows. Such a sensor has several advantages over a conventional hot-wire anemometer, such as faster response times, higher signal-to-noise ratio, robustness of design against damage, small footprint and envelope, immunity against temperature fluctuations, and easy calibration. Figure 4-8 shows the design details and results of such a sensor.

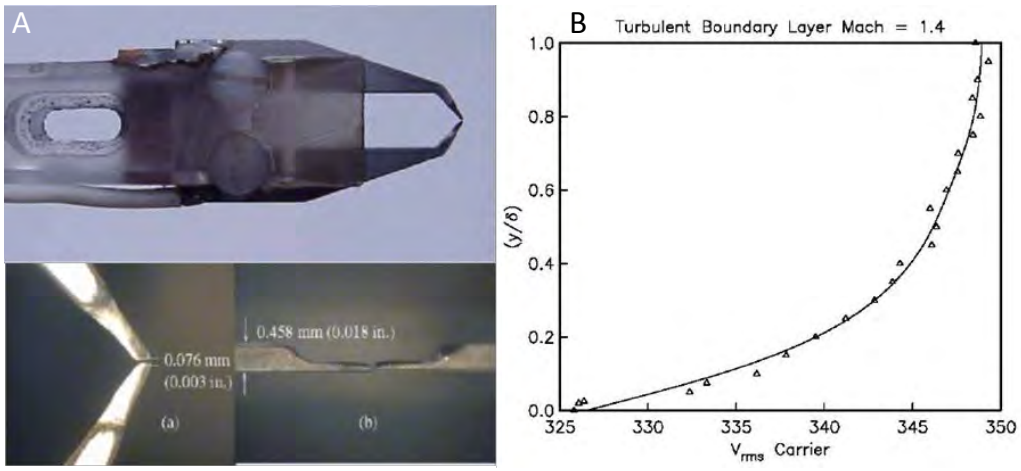

Figure 4-8. Plasma-actuator based anemometer. A) Design details. B) Measurement result from a turbulent boundary layer for a Mach 1.4 flow (Matlis, Corke, Cameron, & Morris, 2008).

4.4 DBD Actuator Characteristics

The effects of DBD actuation are strongly dependent on the operating parameters, which include electrical (voltage, frequency, waveform, duty cycle), geometrical (width and thickness of ground electrode, electrode spacing, thickness of dielectric), material (composition of dielectric, and electrodes), ambient conditions (gas composition, pressure, temperature), and arrangement (multi-barrier actuators, actuator arrays). Several studies are available in published literature on all of the above parameters. However, for the sake of brevity, only the most relevant parameters and representative publications are cited.

4.4.1 Effect of Operating Voltage

As the voltage is increased, the induced velocity is seen to increase up to a certain threshold voltage, after which it starts to plateau (Forte, Jolibois, Moreau, Touchard, & Cazalens, 2006). The induced thrust also shows similar trend, first increasing as voltage to the power 3.5, then reaching a saturation point after which it starts dropping (Durscher & Roy, 2012). The saturation phenomenon has been

investigated with ionization overheating instability resulting from elevated surface temperature as one possible mechanism (Durscher, Stanfield, & Roy, 2012).

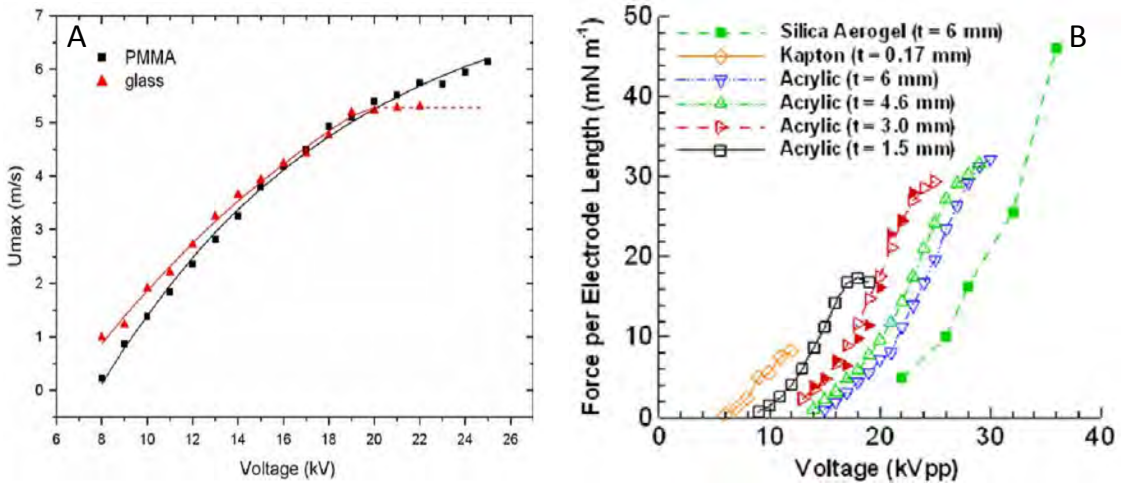

Figure 4-9. Effect of operating voltage on actuator performance. A) Induced velocity. B) Induced thrust (Forte, Jolibois, Moreau, Touchard, & Cazalens, 2006; Durscher & Roy, 2012).

4.4.2 Effect of Operating Frequency

The power delivered in an electrical signal is a direct function of the signal frequency; hence the power delivered to a plasma actuator is also a function of the operating frequency. The induced velocity is seen to increase with frequency in much the same fashion as with voltage, increasing initially before plateauing. The induced thrust at a given voltage is seen to increase with frequency; however the saturation thrust is higher at a lower frequency, suggesting lower frequencies help delay thrust saturation (Corke, Enloe, & Wilkinson, 2009).

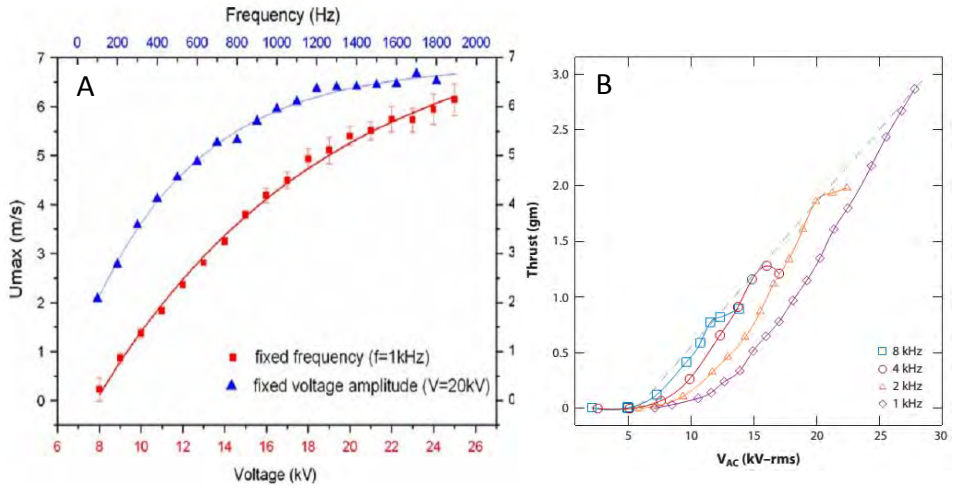

Figure 4-10. Effect of operating frequency on actuator performance. A) Induced velocity. B) Induced thrust (Forte, Jolibois, Moreau, Touchard, & Cazalens, 2006) (Corke, Enloe, & Wilkinson, 2009).

4.4.3 Effect of Dielectric Thickness

The limiting voltage for safe operation a DBD actuator is dependent on the electric breakdown voltage of the dielectric used. This implies thicker dielectrics can be operated at higher voltages, hence produce higher induced velocities and thrust. Experimental investigations corroborate this trend (Forte, Jolibois, Moreau, Touchard, & Cazalens, 2006; Thomas, Corke, Iqbal, Kozlov, & Schatzman, 2009).

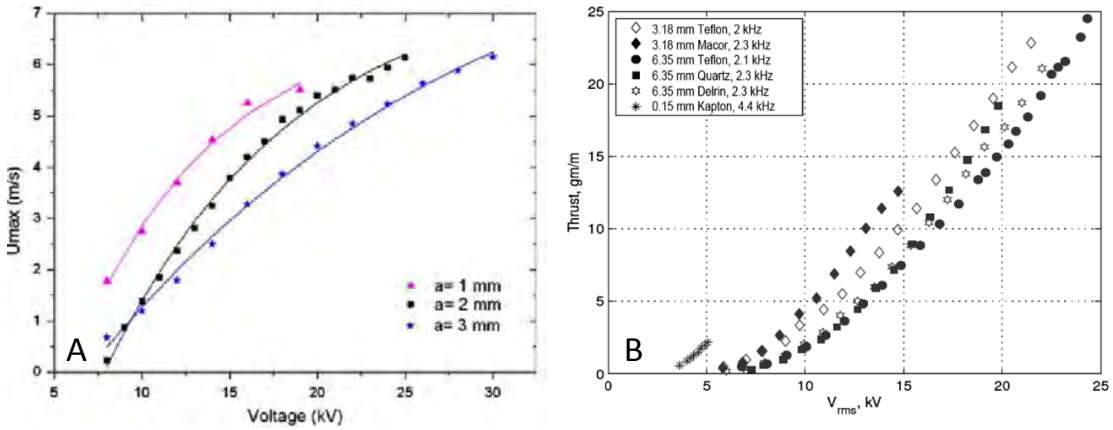

Figure 4-11. Effect of dielectric thickness on actuator performance. A) Induced velocity. B) Induced thrust (Forte, Jolibois, Moreau, Touchard, & Cazalens, 2006; Thomas, Corke, Iqbal, & Kozlov, 2009).

4.4.4 Effect of Dielectric Material

The dielectric constant of a material describes the degree of polarizability of the material. In other words, it represents, relative to vacuum, the amount of energy stored in the dielectric medium under the action of an applied voltage. Consequently, higher dielectric constant means lower breakdown voltage, as the data suggests (McPherson, Kim, Shanware, Mogul, & Rodriguez, 2002). This in turn implies higher energy transfer efficiency, which should mean that for a given thickness and voltage, a stronger dielectric (higher dielectric constant) would generate a higher force. This is indeed the trend observed in experiments (Thomas, Corke, Iqbal, Kozlov, & Schatzman, 2009). However, since a stronger dielectric also has a lower breakdown voltage, the maximum thrust before the actuator reaches saturation is found to be higher for weaker dielectrics.

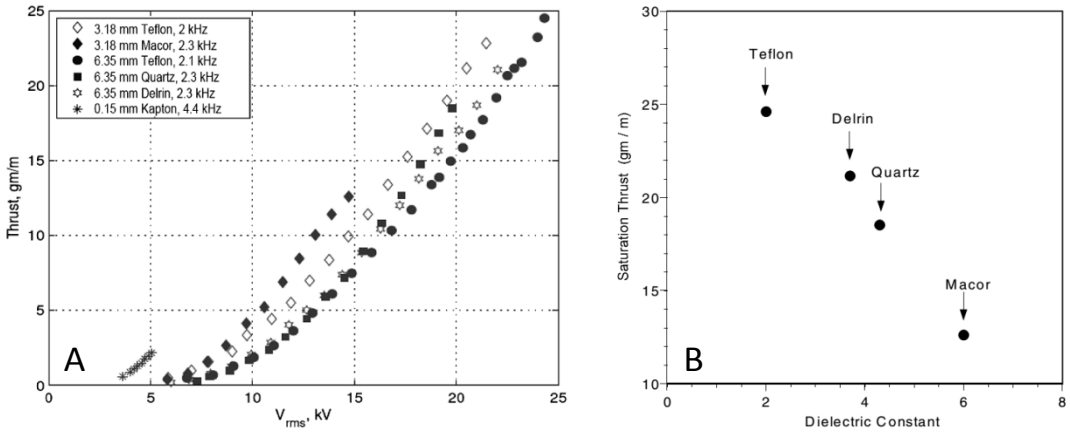

Figure 4-13. Effect of dielectric constant on actuator performance. A) Induced thrust. B) Maximum saturation thrust. (Thomas, Corke, Iqbal, Kozlov, & Schatzman, 2009).

The variation of actuator performance enables the design optimization of a DBD actuator device based on the force/flow requirements and power/weight constraints. It is seen that the actuators show non-monotonic performance with operating parameters, which suggests defining the right design space for a particular design is important for optimal performance.

CHAPTER 5
THE FREE MOLECULAR ELECTRO JET (FMEJ)

Chapter 2 presented a survey of existing micropropulsion options reported in literature. While a lot of them are novel and innovative, and many have been successfully tested, various issues continue to plague the microthruster niche. In an effort to address these issues in the quest for a suitable microthruster, a conceptual microthruster device, called the Free Molecular Electro Jet (FMEJ) (Roy, 2011), is being proposed.

5.1 The Free Molecular Electro Jet

The basic idea behind the FMEJ concept involves embedding electrodes with an electric potential difference along the dielectric surface of the channel walls to produce a discharged. Similar to the dielectric barrier discharge (DBD) , the charged particles in FMEJ channel are driven by the electric field imparting collisional momentum to the propellant in a desired direction by appropriate design and placement of the electrodes. Figure 5-1 shows a schematic of one of the several possible arrangements of the device to illustrate the concept.

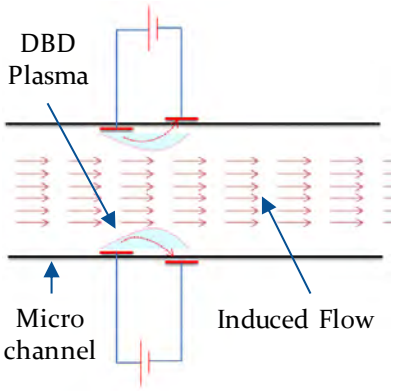

Figure 5-1. Schematic of the FMEJ

The FMEJ channel cross-section is 1 cm x 2 mm x 2 mm. Such a small channel size would result in a small overall thrusters envelop. Such a small foot print will be

quite suitable for small satellites where space and weight are at a premium. The working principle of the FMEJ is a proposed improvement over the existing Free Molecular Micro Resistojet (FMMR) (Ketsdever, Lee, & Lilly, 2005), where electrical energy is first converted into thermal energy by resistive heating, and then into kinetic emery of propellant molecules. In contrast, the FMEJ device convert the energy directly from electrical to kinetic, thus avoiding intermediate losses associated with thermal heating of the microthruster structural components. Moreover, the presence of charged particles implies that both electric and magnetic fields can be used to improve the desired performance of these thrusters. As such, the FMEJ is expected to demonstrate advantages in size, weigh, and power (SWaP) as compared to the FMMR.

5.2 Physics of the FMEJ

The FMEJ operating principle involves the concepts of magneto-hydro-dynamics and plasma physics. A weakly ionized plasma is generated using either a dielectric barrier discharge, or conventional glow discharge in a microchannel by applying a strong enough electric field. The region of ionization extends a finite distance away from the electrodes by the Townsend mechanism, enabling the interaction between ionized region and the bulk neutral region. This interaction takes in the form of different types of collisions (elastic, inelastic, charge-exchange, ionizing), by which momentum is transferred from the charged particles to the neutrals.

The fluid flow in such a channel is governed by a set of partial differential equations known as the Navier-Stokes equations, which put down the principle of conservation of mass, momentum, and energy in mathematical form. The physics of a plasma actuator is expressed mathematically by the momentum conservation equation, presented below.

$$\underbrace{mn\left(\frac{\partial\langle\mathbf{v}\rangle}{\partial t}+\langle\mathbf{v}\rangle\bullet\nabla\langle\mathbf{v}\rangle\right)}_{\text{Rate of change of momenum}}=\underbrace{\Delta\mathbf{M}\big|_c}_{\substack{\text{momentum}\\ \text{lost via}\\ \text{collisions}}}-\underbrace{m\langle\mathbf{v}\rangle f\big|_c}_{\substack{\text{momentum change}\\ \text{via particle gain/loss}}}-\underbrace{\nabla\bullet\mathbf{P}}_{\text{Pressure gradient term}}+\underbrace{qn\left(\mathbf{E}+\langle\mathbf{v}\rangle\times\mathbf{B}\right)}_{\text{Plasma body force term}} \quad (5\text{-}1)$$

Equation 5-1 relates the change in momentum of the fluid (LHS term) to various macro and micro level phenomena. Momentum loss in inelastic collision, changes in momentum by virtue of changing amount of a specie, and momentum diffusion resulting from pressure gradient are inherent to all fluid flows. The fourth term on the RHS captures the interaction of plasma with neutral fluid via collisions, which results in transfer of momentum from the charged species to the neutrals, resulting in an induced bulk velocity.

Plasma discharges in such application are self-limiting by virtue of the phenomenon of charge deposition, which cancels the applied field locally, leading to the quenching of the plasma microdischarge filament (Kogelschatz, 2003). This self-limiting nature ensures the current and power drawn by a plasma actuator device do not exceed the system architecture limits.

Moreover, the possibility of physical downscaling of conventional microactuators has been demonstrated in literature (Zito, Durscher, Soni, Roy, & Arnold, 2012a; Zito, et al., 2012b) While conventional DBD actuators have powered and ground electrodes of the order of several mm, and dielectric thickness generally of the order of several hundred microns, microactuators have been fabricated with electrode thickness, electrode widths and dielectric thicknesses of the order of 10 microns.

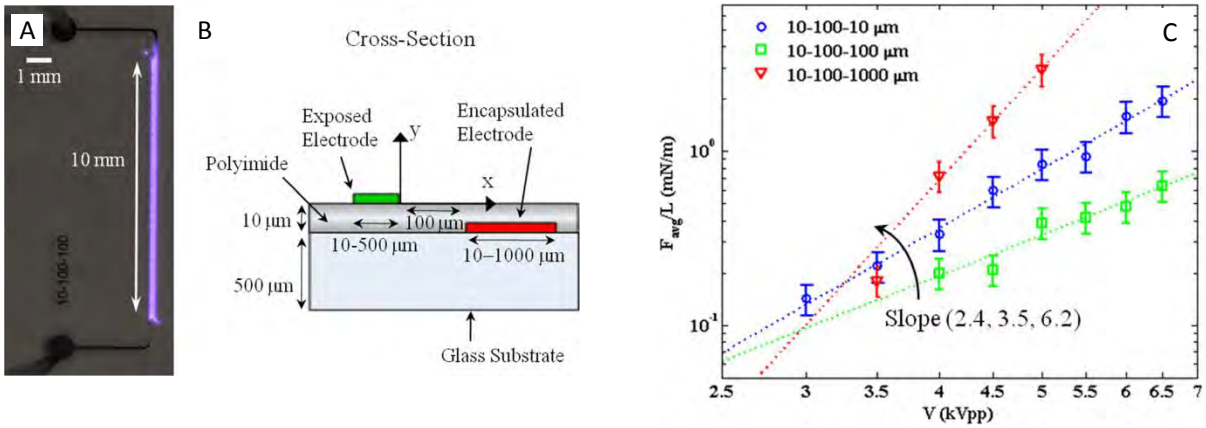

Figure 5-2. Demonstration of the scalability of DBD actuators. A) Microactuator plasma. B) Dimensional schematic. C) Thrust performance (Zito J. C., 2012a)

Direct force measurement of microactuators using a micronewton thrust stand (Zito J. C., 2012a) suggests an order of magnitude improvement in force and induced velocity per unit actuator mass, indicating promising results with downscaling. The higher thrust per weight performance is a major attractive feature for using microactuators for applications where weight is at a premium, such as small satellites and lightweight high-altitude glides.

5.3 Foundational Results

Numerical investigation into the feasibility of an FMEJ concept has been carried out at the Applied Physics Research Group using an in-house computational platform called Multiscale Ionized Gas (MIG). MIG is primarily finite element based modular code which is suitable for ready implementation of stiff multidimensional problems relevant for capturing the physics of FMEJ. This code has been organically developed at APRG over the past 14 years (Roy, 2000; Balagangadhar & Roy, 2001) and has been applied to solve both, plasma and gas dynamic problems at low and high pressures, and at macro and microscales for space propulsion and aerospace applications (Roy & Pandey, 2002; Roy & Pandey, 2003).

A preliminary 2D simulation of an FMEJ channel using a two species plasma fluid model (Rafatov, 2012) for the geometry and electrode arrangement of Figure 5-3 has been carried out (Blanco & Roy, 2013).

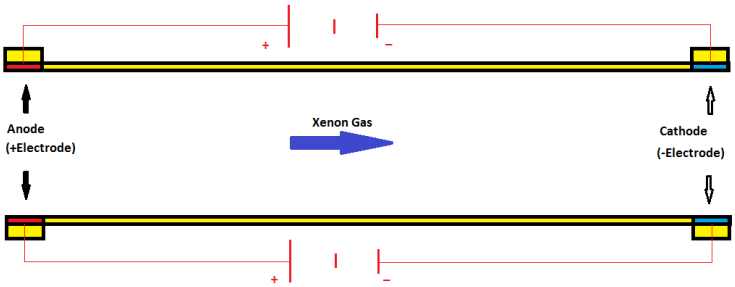

Figure 5-3. Schematic of a FMEJ configuration used in the simulation (Blanco & Roy, 2013).

Table 5-1. Design parameters of FMEJ (Blanco & Roy, 2013).

Parameter	Value
Gas Pressure	100 Pa
Length	1 cm
Height	2 mm
Working Propellant	Xenon
Potential Difference	50 V
Anode Current	23.2 mA
Anode Power	1.16 W
Total body Force (x-comp)	1.19 mN

To compare the device, data is provided in the Table 5-2 for FMMR and the results obtained for FMEJ using the body force distribution from the plasma simulation in a rarefied gas model.

Table 5-2. Comparison between FMMR and numerical prediction of FMEJ (Blanco & Roy, 2013)

Parameter	FMMR	FMEJ
Mass Flow Rate (mg/s)	3.0	3.1
Power (W)	3.2	1.16
Thrust (mN)	1.7	1.7
Isp (s)	58	56
Efficiency (%)	15 %	40 %

The preliminary numerical result shows a 167 % increase of efficiency for FMEJ in comparison with FMMR with similar mass flow rates, thrust and specific impulses. There results deem the prospect of a plasma channel microthruster rather promising, and encourage the experimental validation of the concept.

CHAPTER 6
DESIGN OF A MICRO NEWTON THRUST STAND

The FMEJ concept is proposed as a microthruster for small satellite and high altitude applications, which require forces of the order of several microNewton for executing various maneuvers. Although the design for thrusters capable of delivering these forces has been around for some time, the challenge lies in a method that resolves and measures sub-micro-Newton force accurately and reliably.

6.1 Review of Existing μNewton Thrust Stands

The general approach for a high resolution thrust stand is based on the principle of torsion balance. The thrust stand is essentially a torsion spring, which undergoes angular deflections under the action of a torque. This angular deflection, generated by an unknown force acting at a known distance, can be measured as linear displacement of the balance arm at a known distance from the pivot. The device was first conceived by Charles Coulomb to measure the electrostatic force, which led to the discovery of the Coulomb Law (Coulomb, 1785), and later by Henry Cavendish to measure the gravitational force between two masses (Cavendish, 1798) as illustrated in Figure 6-1.

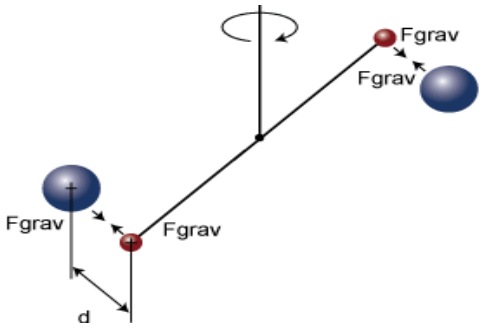

Figure 6-1. Concept of a Torsion Balance used for measurement of gravitational force between masses.

Several torsion balance design have reported in literature with the same fundamental working principles, albeit with different methods of providing a calibration

force, damping technique, and displacement measurement (Jamison A. K., 2001; Ziemer J. K., 2001; Gamero-Castano, Hruby, & Martinez-Sanchez, 2001; Gamero-Castaño, 2003; Koizumi H. K., 2004). Table 6-1 summarizes the detail and the resolution achieved by each of these.

Table 6-1. Review of existing thrust stands with sub-micronewton level resolution

Team	Calibration Source	Damping Mechanism	Displacement Measurement	Resolution	Accuracy
Jamison et al	Orifice Thruster	Viscous Oil Bath	LVDT	< 1 μN	± 2-16 %
Ziemer	Impact Pendulum	Damping coil	LVDT	< 1 μN	20%
Gamero-Castaño et al	Electrostatic	Electrostatic	Fiber Optic LDS	0.01 μN	-
Gamero-Castaño	Electrostatic	Electrostatic	Fiber Optic LDS	0.03 μN	-
Koizumi et al	Impact Pendulum	Electromagnetic	LVDT	0.7 μNs	-

Note that the orifice thruster used by (Jamison A. K., 2001) was calibrated using DSMC techniques, and the lowest thrust measured was 88.8 nN. Actual steady state thrust measure by (Ziemer J. K., 2001) was 1 μN using a FEEP thruster. The lowest thrust measured by (Gamero-Castano, Hruby, & Martinez-Sanchez, 2001) was 0.11μN using an electrospray source, and 7.89 μN by (Gamero-Castaño, 2003) using a colloid thruster. Koizumi et al only measured impulse bits using diode laser ablation microthruster, not steady state thrust.

6.2 The APRG μNTS

Based on the survey of existing thrust stand design, a torsion balance design was chose as the most suitable option. The thrust stand, built to characterize the FMEJ microthruster, aims to resolve forces smaller than 1 micronewton, preferably down to several nanonewtons (~50 nN). Figure 6-2 shows a 3D rendering of the Applied Physics Research Group μNewton Thrust Stand (APRG μNTS) along with a dimensioned schematic. The two flexure pivots at the vertical ends of the cross-beam form the torsion spring providing the restoring torque. The cross-beam is laterally unsymmetrical to optimize the sensitivity within the space constraints (the entire system must fit inside a vacuum chamber sized 10” x 10” x 22” with enough clearance).

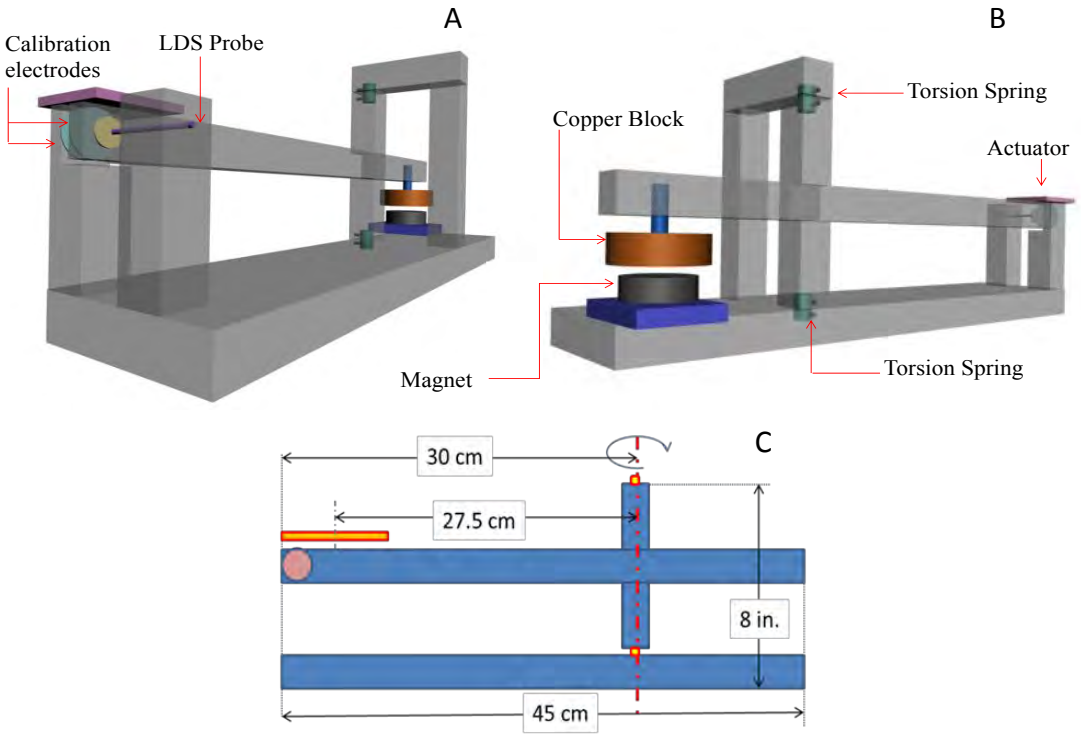

Figure 6-2. Design details of the APRG μNTS. A, B) 3D illustration. C) Dimensional schematic (Soni & Roy, 2013).

The flexure pivots at either vertical end of the cross-beam, as a pair, act as the torsion spring. The copper block acts as a counterweight and balances the asymmetrical beam. A pair of aluminum disc electrodes provides a known force or controlled displacement for calibration. An optical linear displacement sensor (Philtec Model D-63) measures the displacement of the balance arm at a distance to calculate the angular deflection.

6.2.1 Torsion Balance Dynamics

The μNTS is essentially a torsion pendulum. The statics and dynamics of an undamped torsion balance can be completely characterized by two parameters: the torsion spring constant k_θ, and the Moment of Inertia (MI) of the system I_θ, which govern the natural frequency of the system as,

$$\omega_n = \sqrt{\frac{k_\theta}{I_\theta}} \tag{6-1}$$

However, for practical concerns, damping is desired to bring the system to a steady state, facilitating quick readings. For such a damped system, the equation of motion is

$$\ddot{\theta} + 2\varsigma\omega_n\dot{\theta} + \omega_n^2\theta = \frac{f(t)l_T}{I_\theta} \tag{6-2}$$

where $\theta(t)$ is the deflection angle, ς is the damping coefficient, $f(t)$ is the time dependent force, and l_T is the distance from the pivot at which the force forms a torque (moment arm).

For a constant force $f(t) = F$, the solution to Eq. 6-2 is (Ziemer J. K., 2001),

$$\theta(t) = \frac{Fl_T}{I_\theta\omega_n^2}\left[1 - e^{-\varsigma\omega_n t} \times \left(\frac{\varsigma}{\sqrt{1-\varsigma^2}}\sin\left(\sqrt{1-\varsigma^2}\,\omega_n t\right) + \sin\left(\sqrt{1-\varsigma^2}\,\omega_n t\right)\right)\right] \tag{6-3}$$

the steady state solution to which is

$$\theta\left(t \to \infty\right) = \frac{F \cdot l_T}{k_\theta} \tag{6-4}$$

Solving for *F*,

$$F = \frac{\theta\left(\infty\right) \cdot k_\theta}{l_T} = \left.\frac{x}{l}\right|_s \cdot \frac{k_\theta}{l_T} \qquad \because \theta\left(\infty\right) = \left.\frac{dx}{l}\right|_s \tag{6-5}$$

Hence, knowing the steady state deflection $\theta(\infty)$, the spring constant k_θ, and the moment arm l_T, the unknown force *F* can be readily calculated.

For the current design, both the sensor and the calibration electrodes are located at a distance of 28.5 cm from the pivot axis ($l_s = l_T$). The torsion springs, procured from Riverhawk Company, have a rated spring constant of 0.0016 Nm/deg each, with an accuracy of ±10%. In the given configuration, the two torsion spring act in parallel, hence the total spring constant is just a numerical sum giving a mean total spring constant for the system of around 0.0032 Nm/deg. Having these two parameters fixed by design, the resolution of the stand is limited only by the resolution with which the displacements *dx* can be measured, and the accuracy with which the system can be calibrated.

6.2.2 APRG μNTS: Damping Mechanism

Damping a dynamical system is of critical importance to counter noise and reduce the time required to reach a stable deflection of the balance arm. In the absence of damping, the balance arm vibrates for a significant duration (Figure 6-3(A)), with ambient air providing only minimal damping, apart from structural/thermal dissipation at the torsion springs. To make the system more damped, a magnetic damper was introduced based on eddy current damping. A similar concept was demonstrated for damping structural vibrations of a beam (Sodano, Bae, Inman, & Belvin, 2006). For the

μNTS damper, a cylindrical copper block (2 ½ “ dia. x 1” height) of high conductivity was mounted on the balance arm, with a permanent magnet placed under it in close proximity (Figure 6-3(B)).

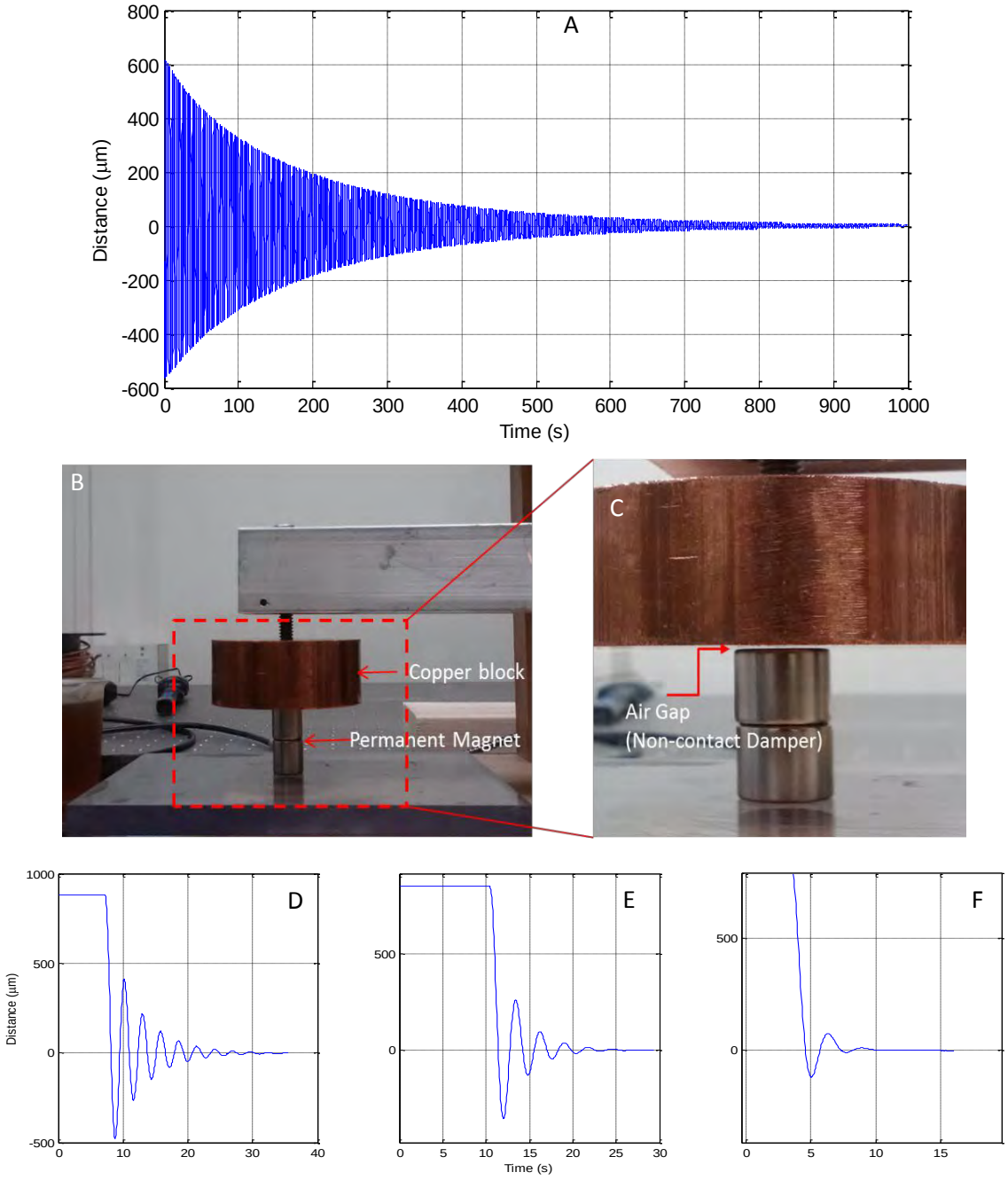

Figure 6-3. μNTS Damping Mechanism. A) Undamped oscillations. B,C) Magnetic damper. D,E,F) Damped oscillations with increasing damping.

As the beam oscillates, the relative motion of the copper block and the magnet produces eddy currents in the block, which generate their own magnetic field counter to the applied magnetic field. The applied and induced magnetic fields interact to produce a force proportional to the relative motion, essentially providing damping. The amount of damping can be controlled by controlling the gap between the copper block and the permanent magnet (Figure 6-3(C)), and close-to-critical damping can be achieved. Magnetic damping has inherent advantages of being a non-contact damper (as opposed to a viscous damper), and of not requiring a power source (as opposed to an electromagnetic/electrostatic damper).

6.2.3 APRG μNTS: Calibration

As reported in Table 6-1, several methods of calibration have been reported in literature. Most of these rely on a device which can produce an accurately known force, against which the system is calibrated, with the exception of the Impact pendulum used (Ziemer J. K., 2001) which relies on applying a known impulse instead of a steady-state force to back out the system dynamics. The orifice thruster (Jamison, Ketsdever, & Muntz, 2001) itself is calibrated using DSMC methods, which introduce a certain amount of uncertainty in the force that the thruster delivers. The electrostatic force calibration method (Gamero-Castano, Hruby, & Martinez-Sanchez, 2001; Gamero-Castaño, 2003) has its own disadvantages. The following error analysis shows that this method inherently introduces multiple sources of error, necessitating a better calibration method.

Consider the electrostatic force calibration. The force between two parallel plate electrodes separated by a distance L and having an area A is given by (Griffith, 2012)

$$F = \frac{1}{2}\varepsilon\left(\frac{V}{L}\right)^2 A \tag{6-6}$$

Combining Eq. 6-5 and 6-6, the calibration constant k_θ can be written as,

$$k_\theta = \frac{\varepsilon}{2}\cdot V^2 \cdot \frac{1}{L^2}\cdot A \cdot l^2 \cdot \frac{1}{dx} \tag{6-7}$$

Applying error propagation analysis to this equation yields the following equation for relative uncertainty in k_θ,

$$\frac{\partial k_\theta}{k_\theta} = \sqrt{\left(\frac{2dV}{V}\right)^2 + \left(\frac{2dL}{L}\right)^2 + \left(\frac{dA}{A}\right)^2 + \left(\frac{2dl}{l}\right)^2 + \left(\frac{dx}{x}\right)^2} \tag{6-8}$$

As can be seen, there are five sources of error in the above calibration method, some of which can be controlled more precisely than others. The applied voltage *V*, electrode area *A*, and the moment length *l* can be controlled to a fair degree of accuracy. However, the electrode gap *L* (typically 1mm), and the sensor resolution *dx* (50 nm) present the biggest challenge in controlling the spread of the calibration data. Moreover, Analysis suggests that a 10% error in *L* alone leads to nearly 20% error in k_θ. Accounting for errors from the other sources would increase this figure further.

To overcome this limitation, the system was calibrated using three different approaches, and the uncertainty and error sources in these methods were analyzed to choose the optimal method. The first method entailed observing the natural frequency of the undamped system to back out the spring constant using the relation Eq. 6-1 reformulated as

$$k_\theta = \omega_n^2 \cdot I_\theta \tag{6-9}$$

The moment of inertia (MI) I_θ of the system is computed by superposition of the MIs of the component shapes and parallel axis theorem. This gives an estimate of I_θ =

0.0385 Kg-m^2. The natural frequency for the undamped system is observed to be 2.240 rad/s from the Figure 6-3(A). These values, in conjunction with Eq. (6-9), give an estimate for k_θ of around 0.0034 N-m/deg, close to the stipulated value of 0.0032 and within the 10% error margin quoted by the manufacturer. Of course, this value of k_θ would only be an approximation of the actual value to a certain error, since the system is not really undamped, as the air around the system provides a small but finite amount of damping. The log-decrement method is used next to calculate exactly how much damping the air provides, and to compute a more precise estimate of k_θ.

The log decrement method (Soni & Roy, 2013) backs out the damping ratio of the system based on successive peaks of damped oscillations, which, in conjunction with the observed damped frequency, provides an estimate of the spring constant. For n cycles of a damped oscillation, the logarithmic decrement δ is defined as

$$\delta = \frac{1}{n} \ln \frac{x_0}{x_n} \tag{6-10}$$

where x_0 and x_n are the amplitudes of the first and nth peaks respectively. The damping ratio ζ is then found using the relation

$$\varsigma = \frac{1}{\sqrt{1 + \left(\frac{2\pi}{\delta} \right)^2}} \tag{6-11}$$

From the observed damped frequency ω_d and the damping ratio, the natural frequency ω_n can be estimated as

$$\omega_n = \frac{\omega_d}{\sqrt{1 - \varsigma^2}} \tag{6-12}$$

Finally, the spring constant then can be estimated as

$$k_\theta = \omega_n^2 \cdot I \tag{6-13}$$

Applying this method to the data extracted from Figure 6-3(A), we get an average value of k_θ = 0.003379 N-m/deg based on several values of n, demonstrating that neglecting air damping results in a nominal error of approximately 0.7 %. The damping ratio in this case is found to be around 0.0028, justifying the undamped assumption.

The same analysis is applied to the system when it is damped using the magnetic damper. Since this is the configuration in which the setup will be used for future force measurement, a comprehensive set of calibration reading are taken at varying displacements, to ensure linearity of the spring constant over the desired range of displacement. Increasing displacements are produced using electrostatic force exerted by the parallel electrodes, and the system is set to vibrate by turning off the force. As evident in Figure 6-4, calibration values from both the electrostatic force and log decrement method are seen to converge around a value of 0.00345 N-m/deg, with a standard deviation of just over ~ 0.07%. The spread in the data at lower displacements has to do with the fact the LDS signal-to-noise ratio decreases at lower displacement, leading to higher uncertainty in the results. Moreover, a slightly higher value than the nominal 0.0032 Nm/deg is to be expected since the axial and radial loading that the springs are under alters the spring constant slightly. This was further confirmed by a Riverhawk technical representative.

The log-decrement method offers the unique advantage that it is free from any errors in the source used to generate the displacement, and depends only on the response of the system itself. This greatly reduces the uncertainties associated with calibration process, with the only source of errors being the lower limit on the sensor resolution (which determines the uncertainty in ω_n, and the accuracy with which the

Moment of Inertia of the system can be calculated. The uncertainty propagation relation for Eq. 6-13 would be

$$\frac{\partial k_\theta}{k_\theta} = \sqrt{\left(\frac{2d\omega_n}{\omega_n}\right)^2 + \left(\frac{dI_\theta}{I_\theta}\right)^2} \tag{6-14}$$

The Moment of Inertia I_θ can be computed to a high degree of certainty using precision a weighing scale and Vernier calipers. A simple uncertainty analysis suggests a good conservative estimate for dI_θ would be 5%. The relative uncertainty estimate for ω_n is not so straightforward since it depends on the way the errors in x_0 and x_n propagate through Eq. 6-10 through 6-12, resulting in an estimate which depends on the actual values of δ, ζ, and ω_n. Reasonable estimations based on typical values of ζ (~0.14) suggest a 10% spread in ω_n. These error estimates gives an error estimate of 20.6% for k_θ. Figure 6-4 suggests the statistical scatter in k_θ is also of the same order; hence the data obtained using the μNTS is quoted with this level of the statistical error. The μNTS setup for thrust measurement of microactuators (Zito, Durscher, Soni, Roy, & Arnold, 2012a) thus validating its resolution.

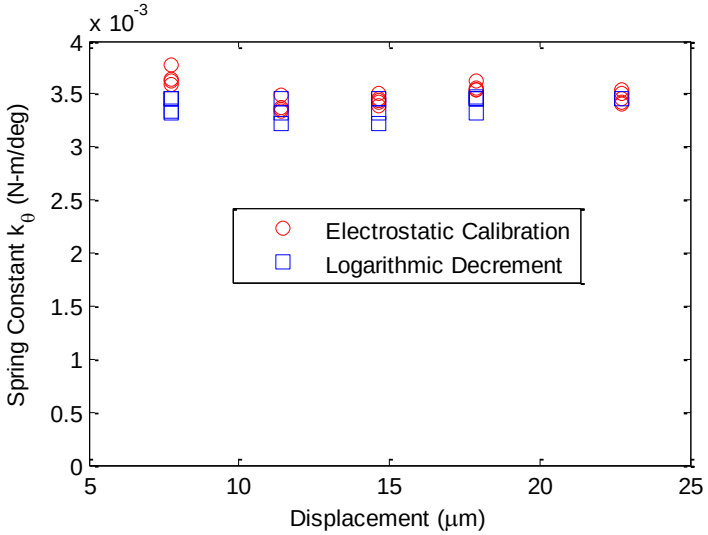

Figure 6-4. μNTS Calibration : Comparison between electrostatic force calibration and log decrement method

To check how the μNTS compares against a commercial balance, a test actuator was designed and tested on both the μNTS, and a commercial precision balance (Ohaus Adventurer ProTM AC313C, 1 mg resolution). The actuator consisted of 1.5mm thick acrylic with 5mm powered electrode and a 20mm ground. The upstream edge of the powered electrode was covered to prevent reverse discharge, and the ground electrode was covered with several layers of electrical tape. The actuator mounted on the commercial precision balance was 95mm long (to produce enough force to assure a high signal-to-noise ratio), whereas the actuator mounted on the μNTS was 20mm in length due to space and displacement constraints on the μNTS. The force data from the μNTS, shown in Fig. 6-5, suggests decent agreement with between the two balances. We see that direct force measurement from the μNTS start diverging at higher voltage (above 15 kVpp). This might have to do the different downstream plate lengths of the two actuators, being shorter in case of the 20mm actuator. It has been reported in literature that indeed a shorter downstream plate length leads to a higher force (by upto 20%) due to decreased drag loss along the plate surface (Durscher & Roy, 2012).

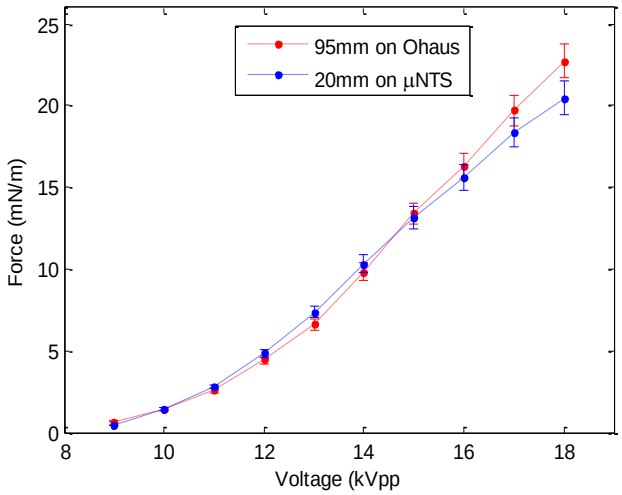

Figure 6-5. Comparison of force measurement from commercial precision balance and μNTS

6.2.4 APRG μNTS Noise Characterization

The useful resolution of any real-world device is incompletely defined without specifying the acceptable signal-to-noise ratio of the signal being measures. The device may be able to ‘resolve’ the changes in the signal, but if the change is just of the order of the noise, specifying the resolution is not sufficient unto itself. For this purpose, we define the resolution of the μNTS at a specified expected SNR. A resolution of 1 μN at a SNR of 10 implies that the μNTS successfully resolves a force of 1 μN at a SNR of at least 10 or better. Thus the minimum resolution is taken to be a measurement that is at least 10 times the background noise.

The targeted resolution of the thrust stand renders it susceptible to a myriad of external and internal noise sources. The external sources include any external mechanical disturbance transmitted to the force balance by seismic or pressure disturbances. To alleviate these, the thrust stand is housed inside a transparent isolation chamber to prevent from air drafts, and stationed on top of a heavy optical bench to emolliate seismic disturbances. Internal sources primarily include electrical noise in the LDS optical amplifier and electronics.

To characterize the internal μNTS noise, the signal from the linear displacement sensor pointed to a stationary target (a polished aluminum surface) is monitored over several different durations to identify and characterize any noise patterns. Figure 6-6 show the sensor output over several different time scales. The plots suggest that in the absence of mechanical noise (fixed target), the electrical noise of the sensor is of the order of 0.01 μm, which corresponds to a force of about 0.02 μN. The plot of displacement over several hours shows that the sensor reading drifts by upto 1.5 μm, which corresponds to a force of about 3 μN.

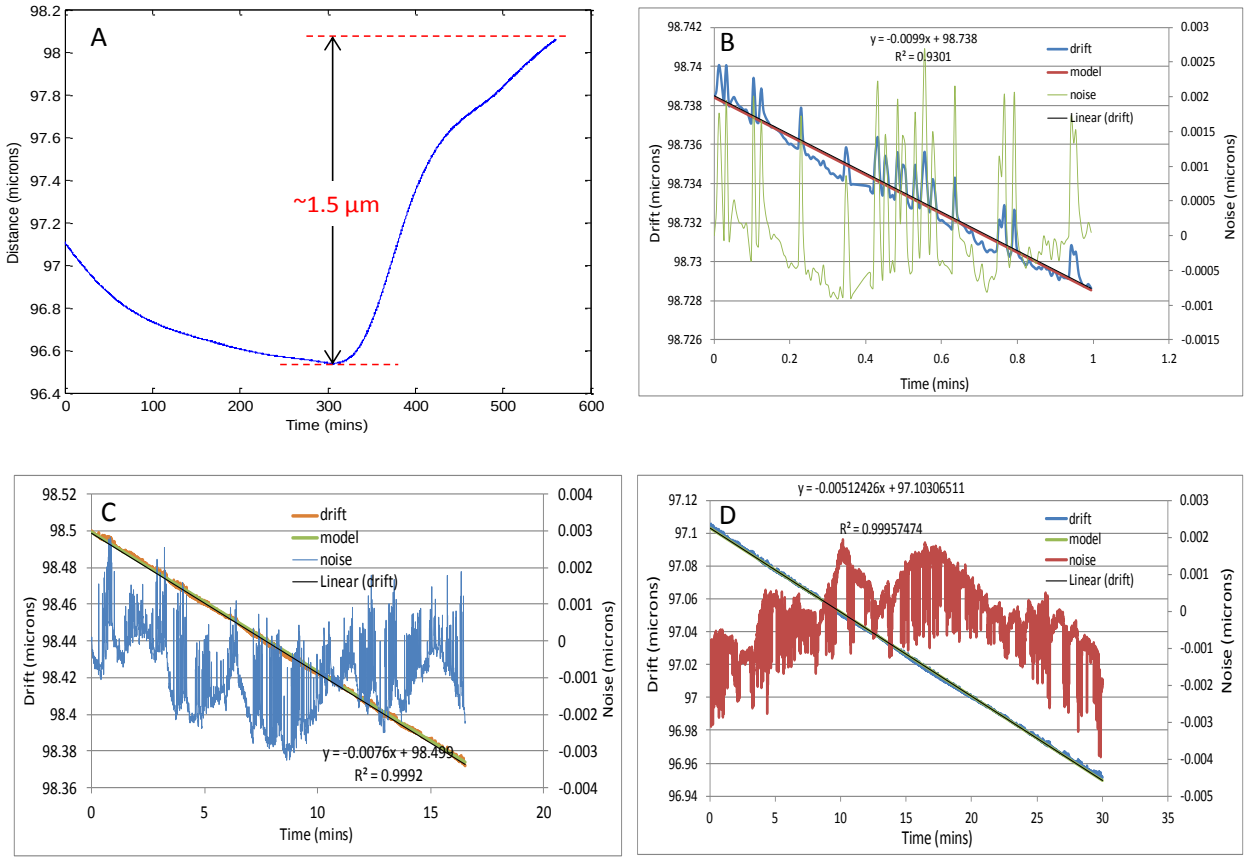

Figure 6-6. Sensor noise and drift over several different timescales. A) 8 hours. B) 1 minute. C) 15 minutes. D) 20 minutes.

The drift is found to be extremely linear over short timescales, simplifying the task of drift subtraction since a typical force measurement lasts only a few minutes. However, for the sake of completeness, an investigation was done to identify the source of the drift, and thermal expansion of the target block resulting from ambient temperature fluctuations was identified as one possible cause. Hand calculations considering the size and coefficient of thermal expansion of the aluminum target block over the measured temperature fluctuation further support this hypothesis.

To characterize the external noise, the sensor was integrated with the thrust stand, and readings taken without any force producing device mounted on the stand. The following shows a 30 minute plot of the sensor. The trend suggests a periodic noise

superimposed on the linear drift. Subtraction of the linear drift from the original signal reveals a highly sinusoidal noise profile (Figure 6-7).

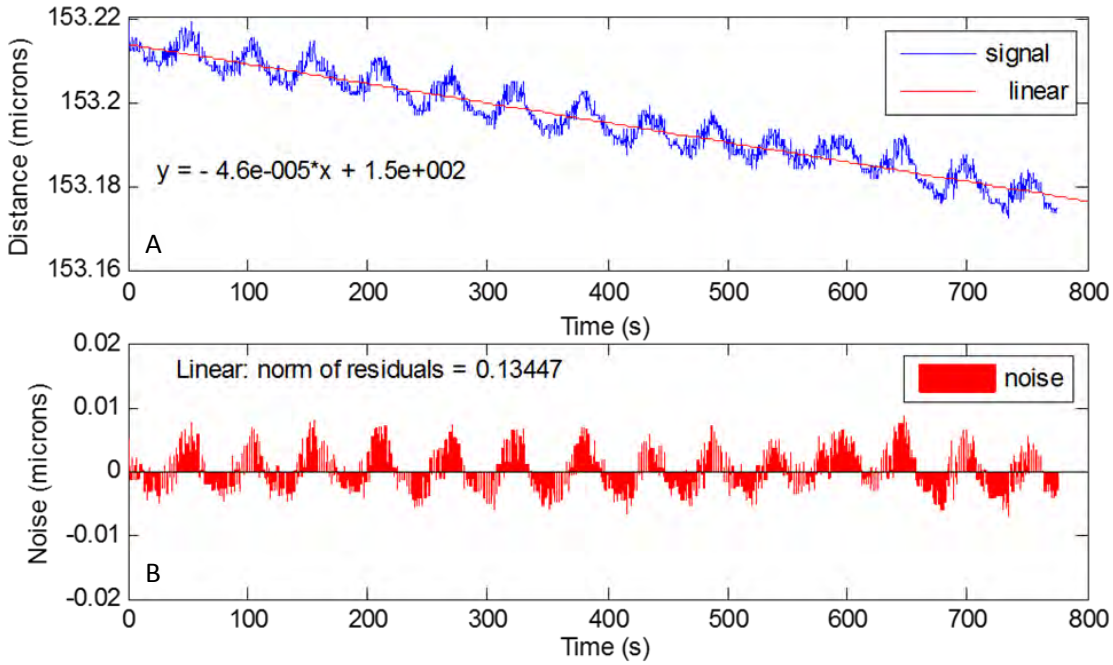

Figure 6-7. Sensor noise profile. A) Sensor drift. B) Mean noise about the drift.

Autocorrelation analysis of the noise produces a weak delta function coupled with superimposed sinusoidal noise, which is in agreement with the observed noise profile. To capture the frequency of the sinusoidal components, both the original signal, and the autocorrelation function are analyzed using Fast Fourier Transform. Figure 6-8 shows the Fast Fourier Transform of the autocorrelation function, which identifies the frequency component in the autocorrelation function, which corresponds to the frequencies in the original signal. The frequency-amplitude spectrum shows a major peak at 0.01864 Hz, and two minor peaks at 0.01678 Hz, and 0.001243 Hz.

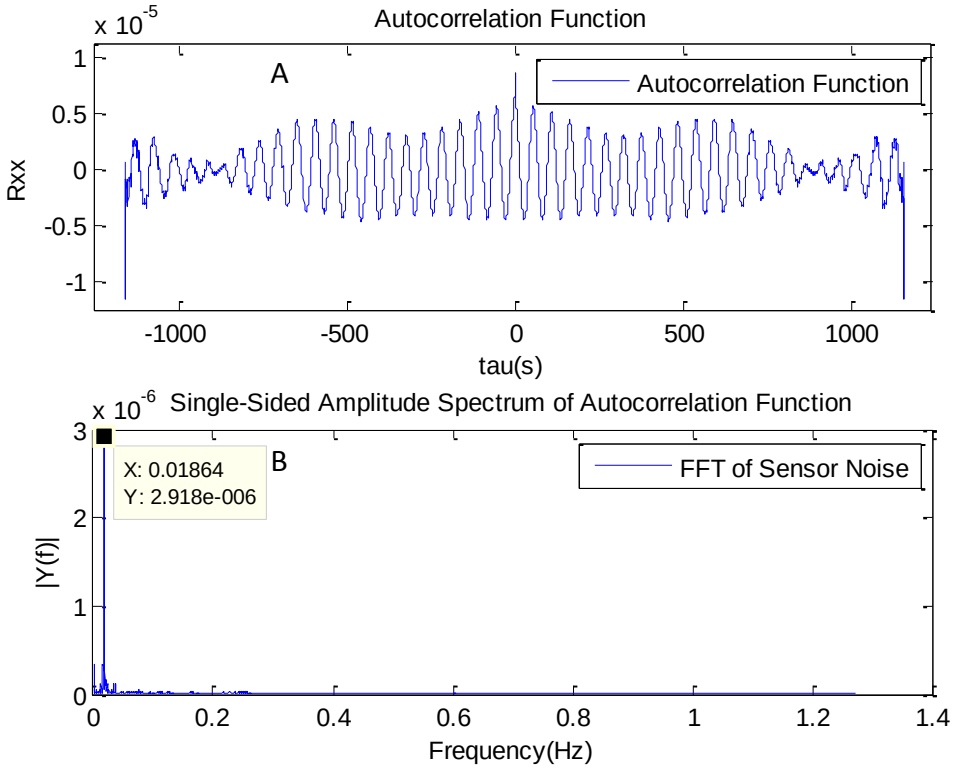

Figure 6-8. Sensor noise signal analysis. A) Autocorrelation of sensor noise profile. B) Fast Fourier Transform of the Autocorrelation function.

As a confirmation of the above plot, an independent FFT of the original signal was performed and the result compared with the FFT of the autocorrelation to see if the frequency peaks match between the two. Figure 6-9 shows the original drift-subtracted noise, and the frequency-amplitude spectrum of this noise profile. This plot confirms the frequency peak at 0.0864 Hz, along with some minor peaks in the same vicinity as the FFT of the autocorrelation function.

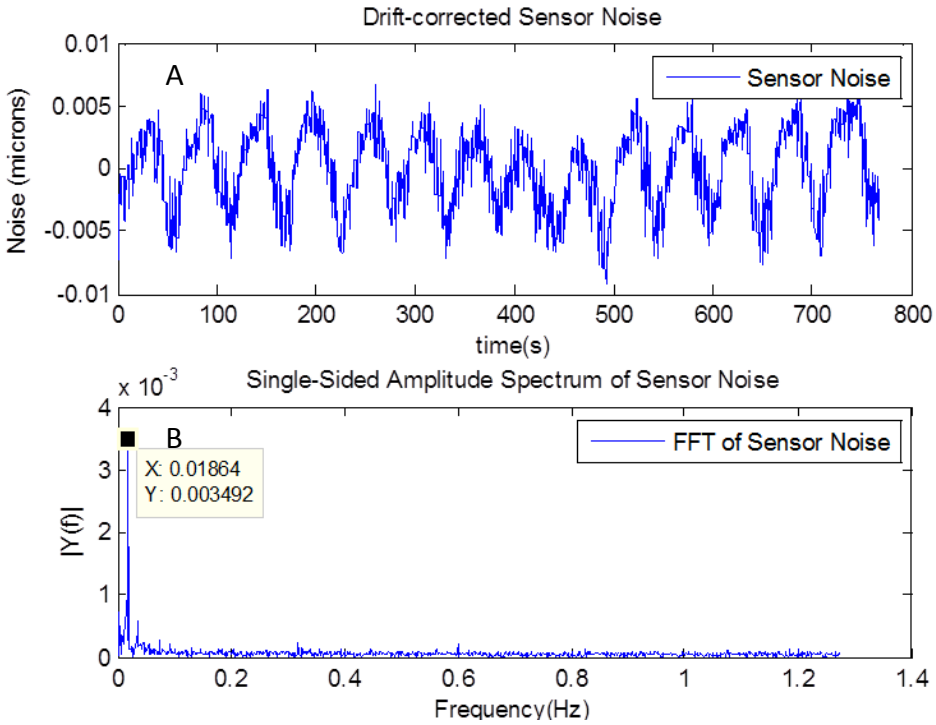

Figure 6-9. Sensor noise characteristics. A) Drift-subtracted sensor noise. B) Fast Fourier Transform of this noise.

Although presence of a noisy sine wave in the sensor standalone output is confirmed, this frequency is 2 orders of magnitude lower than the 60 Hz main noise that is a possible suspect. This might be due to the fact that the sampling frequency for this time series (2.5 Hz) is 24 times less than the signal frequency itself, which will inevitably lead to aliasing.

The Nyquist frequency f_N for a sampling frequency f_s of 2.5 Hz is 5 Hz. The apparent frequency f_{app} from the above FFT plots is 0.01864 Hz, giving f_{app}/f_N ratio of 0.007456. From the folding diagram, f_{act}/f_N can take values $2n + 0.007456$, where n is an integer, i.e. f_{act} can take values of $5n+0.01864$. Figure 6-10 below is a plot of f_{act} for various values of n.

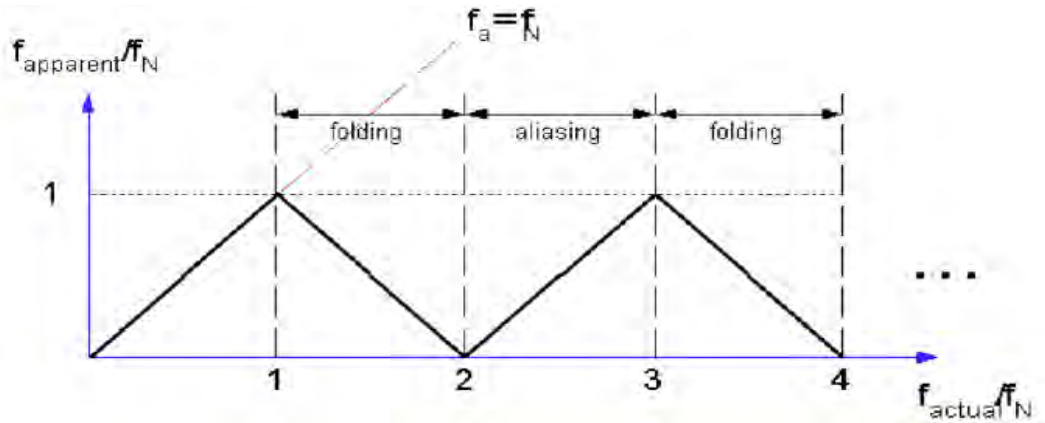

Figure 6-10. Frequency Folding Diagram showing the regions of folding and aliasing

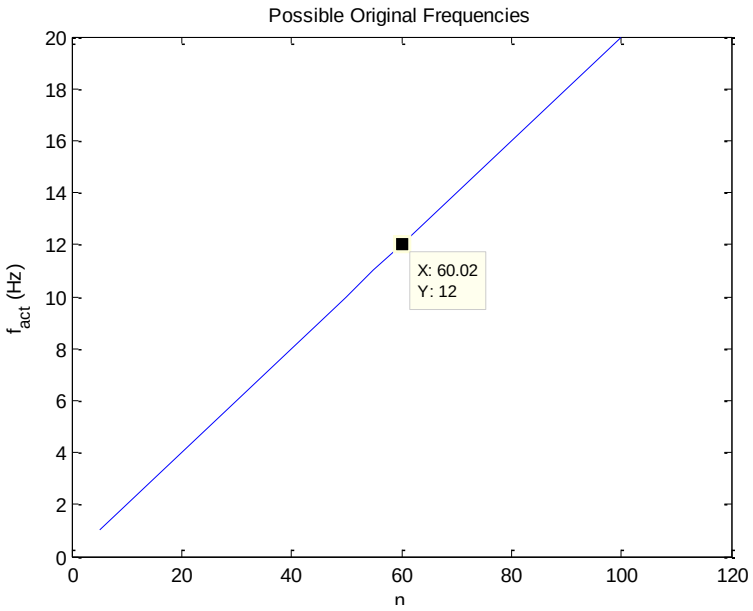

Figure 6-11. Possible Source Frequencies for the aliased frequency of 0.01864 Hz

From the plot of Figure 6-11, we see that for n =12, fact takes on a value of 60.02 Hz, which is very close to the frequency of the mains hum that we were looking for. The difference is only 0.03% assuming the main frequency is exactly 60 Hz, which it generally is not due to non-linearities and other disturbances. Philtec representative later revealed the noise maybe due to stray light from fluorescent lighting, which is known to flicker at line frequency (60 Hz). To rectify the situation, a noise-corrected version of the sensor was procured.

The quality of results of an experiment depends directly on the quality of the instrument used to obtain them. The purpose of this chapter was to present the design and characterization of a thrust stand capable of resolving the forces that the FMEJ is intended to produce. The stand was build around the tried and tested principle of torsion balance, with some novel techniques for damping and calibration. Eddy current damping is demonstrated to be at par with other damping methods while being simpler in design and operation. The log decrement method was proposed and demonstrated to have certain advantages over the previous reported calibration methods. Extensive noise characterization was done to establish the SNR and limiting resolution of the stand.

CHAPTER 7
LOW PRESSURE DBD ACTUATION

The force production mechanism of DBD actuators borrows heavily from the collision dynamics between charges particles and neutrals. Both the concentration of these species, and the collision dynamics, are related to ambient conditions, specifically pressure. The ionizability of gases is a strong function of gas pressure, with increasing ionization as the pressure decreases. For the case of parallel plate electrodes separated by a distance, the relation between the breakdown voltage and the product of the electrode gap and the pressure is given by Paschen's Law, given as (Raizer, 1987)

$$V_B = \frac{Bpd}{\ln(Apd) - \ln\left[\ln\left(1 + \frac{1}{\gamma_{sc}}\right)\right]} \tag{7-1}$$

where V_B is the breakdown voltage, p is the pressure, d the distance between electrodes, γ_{sc} is the secondary ionization coefficient, and A and B are constants that depend on the gas. The breakdown voltage as a function of pd is plotted in Figure 7-1 for various gases.

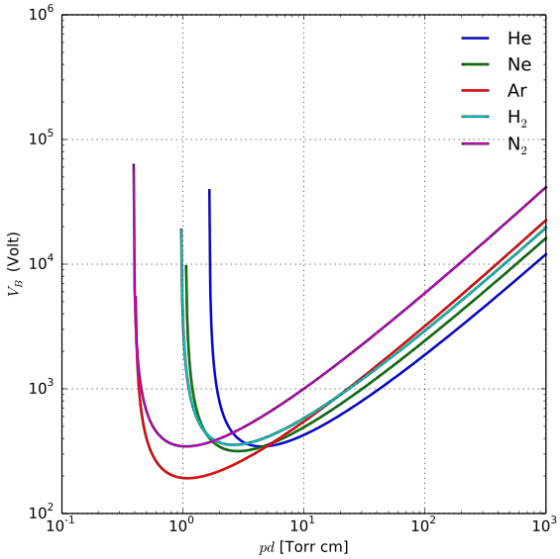

Figure 7-1. Electrical breakdown voltage as a function of gas pressure and electrode gap

The reduction in pressure also means a proportional reduction in the densities of respective species. Since collision frequencies of species pairs are a function of the specie density, a reduction in pressure generally leads to a change in collisional interactions and resulting macroscale effects. For DBD actuators, this manifests as a change in the momentum transferred from the charged species to the neutral species, resulting in changes in induced velocities and thrust.

Most of the studies on DBD actuators over the last decade have focused on the effect of various parameters at atmospheric operation. Few publications sufficiently address low pressure performance over a wide range of operating parameters, or attempt to understand the change in the physics as the pressure is decreased. The following sections will review the publications that do delve into this area.

7.1 Literature Review of Low Pressure DBD Actuation

One of the earlier attempts to understand the force production mechanism proposed a theoretical model based on collisional theory (Gregory J. W., 2007). The mode suggested that, at constant power, the net force generated by the actuator decreases linearly with pressure. The force was shown to be independent of the neutral number density, but dependent on ion density and the volume of plasma. The model was supplanted with experimental results between a pressure range of 141 and 584 Torr with good agreement (Figure 7-2).

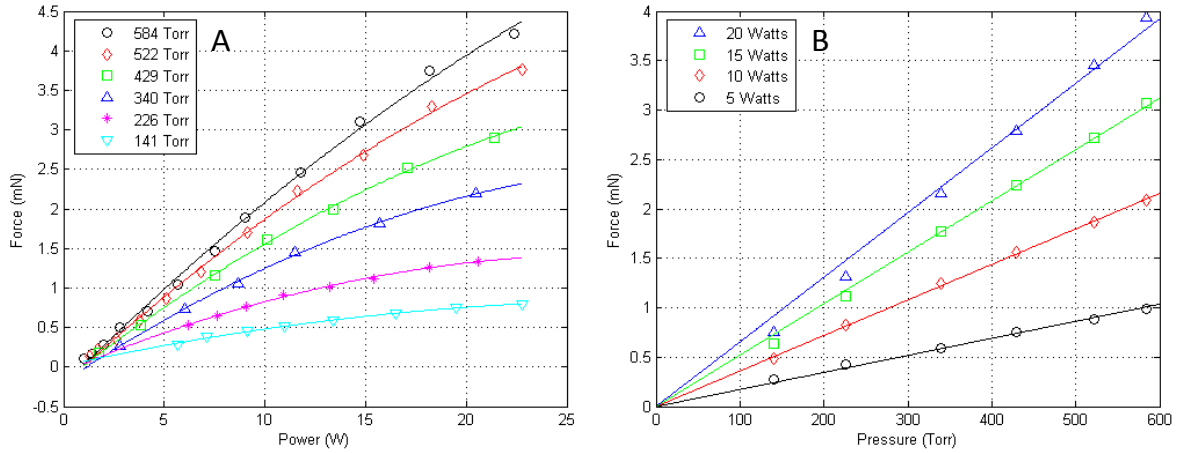

Figure 7-2. Force generated by the plasma actuator. A) As a function of pressure. B) As a function of power dissipation (Gregory, Enloe, & Font, 2007).

However, when the pressure was reduced from atmospheric pressure at a constant voltage, it was found (Abe, Takizawa, & Soto, 2008) that the force first slightly increased before reducing and tending to zero as the pressure was reduced further (Figure 7-3 (A)). The amount of force increase, and the pressure at which the force peaks, was found to be a function of the gas composition (air, CO_2, N_2), electrode material (Cu vs. SS), and electrode topography (metal tape vs. wire mesh). The induced velocity was found to exhibit similar trends, while the power was found to increase more or less linearly as the pressure was reduced (Figure 7-3 (B)).

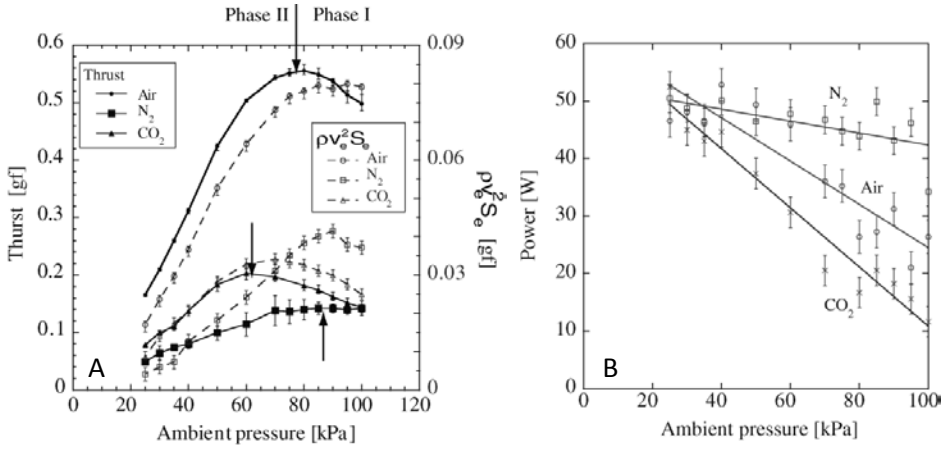

Figure 7-3. Actuators force as a function of pressure. A) Actuator thrust. B) Power consumption (Abe, Takizawa, & Soto, 2008).

Investigation into the effects of elevated pressures and temperatures has also been reported in literature. One such study (Versailles, Gingras-Gosselin, & Duc Vo, 2010) assessed the performance of DBD actuators over a range of 100 to 690 kPa. It was found that the plasma density and extend reduced with increasing pressure, and the induced velocity and body force diminished non-linearly with increasing pressure (Figure 6-4 (A)). The effect of ambient temperature between the range of 30 to 200 ˚C at atmospheric pressure was also investigated, and it was found that the induced force increase almost linearly with increasing temperature over this range of temperatures (Figure 7-4 (B)).

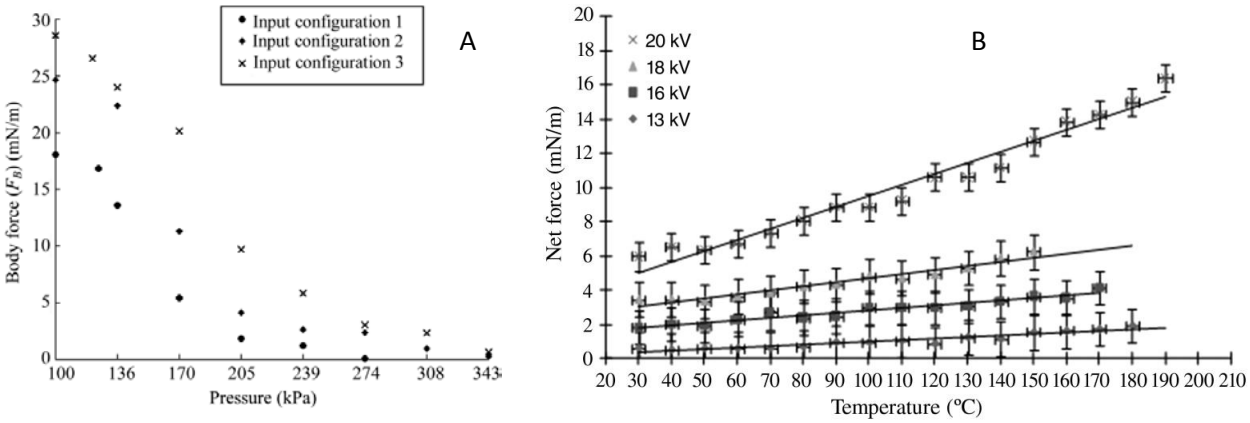

Figure 7-4. Effect of ambient conditions on actuator thrust. A) Elevate ambient pressure. B) Elevated ambient temperature (Versailles, Gingras-Gosselin, & Duc Vo, 2010).

Another study investigated the effect of dielectric constant, dielectric thickness, and pressures on the average initiation voltage (the voltage at which plasma initiation takes place) (Valerioti & Corke, 2012). The effect of the three parameters was lumped into the dielectric capacitance of the actuator. Their indicated a negative power relationship between the average initiation voltage and capacitance per unit area (Figure 7-5). The relationship is anticipated as a thinner dielectric with higher dielectric constant 'ignites' easier than a thicker dielectric with a lower dielectric constant.

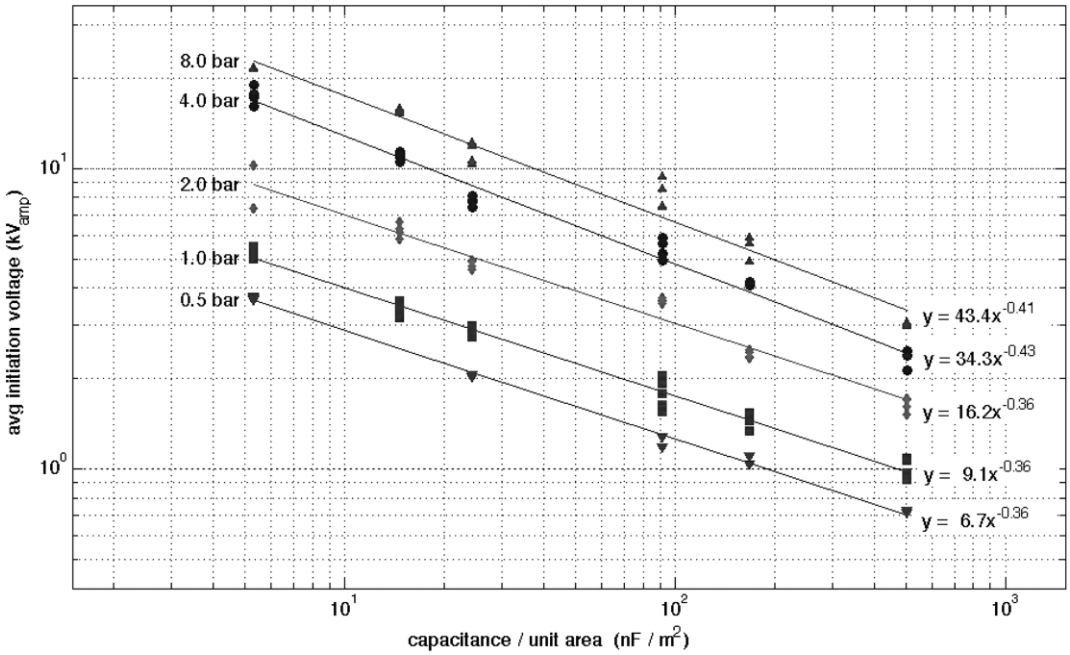

Figure 7-5. Average initiation voltage as function of pressure and capacitance per unit area (Valerioti & Corke, 2012).

In the same study, the induced force was found to increase with pressure upto a certain point, after which it started tapering off (Figure 7-6 (A)). For sub-atmospheric pressures, the force showed similar trend as previous study (Abe, Takizawa, & Soto, 2008), with the force initially increasing upto a certain pressure, followed by a decrease (Figure 7-6 (B)). This inflexion point, however, was only observed above a threshold voltage, below which, the force monotonically reduced with pressure. The pressure at which the force peaked and the amount of increase were both found to be a function of operating voltage, with higher voltages resulting in a peak thrust at ever lower pressures.

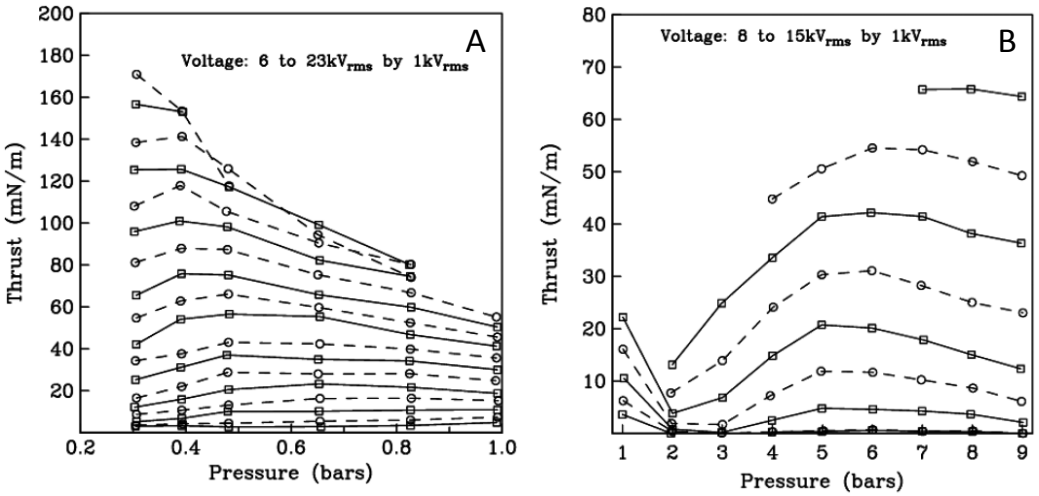

Figure 7-6. Induced body force as a function of pressure. A) At above atmospheric pressures. B) At sub-atmospheric pressures (Valerioti & Corke, 2012)

None of the aforementioned literature, however, sufficiently addresses the effect of dielectric material, and thickness on performance at low pressures. This creates an urgent need for a more comprehensive investigation into DBD actuator performance at reduced pressures.

7.2. Experimental Setup for Current Study

7.2.1 General Experimental Setup

The actuators tested in this study had varying lengths; hence versatility of setup was required for reliable force measurement. The forces from relatively long actuators are well above the resolution of commercial precision balance, and one such balance was used for the long actuators. The force from the shorter actuators, on the other hand, is below the resolution of commercial precision balances. Consequently, a custom high precision thrust stand was built and characterized to characterize the smaller actuators, as presented in (Soni & Roy, 2013). Both these force measuring devices are placed inside an acrylic chamber 22” x 10” 9” in size.

The setup used to measure force from the long actuators consists of a high precision electronic balance (Ohaus Adventure ProTM AV313C) with a resolution of 1 mg (~10 μN). The balance is placed in a 40L capacity acrylic vacuum chamber (23” x 11” x 10”) connected to a 3 CFM vacuum pump. A relief valve is used to regulate the level of vacuum inside the chamber by controlled leakage. A pressure gauge (MKS 910 Piezo Pirani) fitted to the side of the chamber reads the pressure to within 1% error. For measuring forces smaller than the resolution of the commercial balance, the μNTS is used. The force stand is placed inside the vacuum chamber, with power supplied to the actuators via AWG 36 magnetic wire to reduce external disturbance due to power connections. Figure 7-7 illustrates the setup for both the cases.

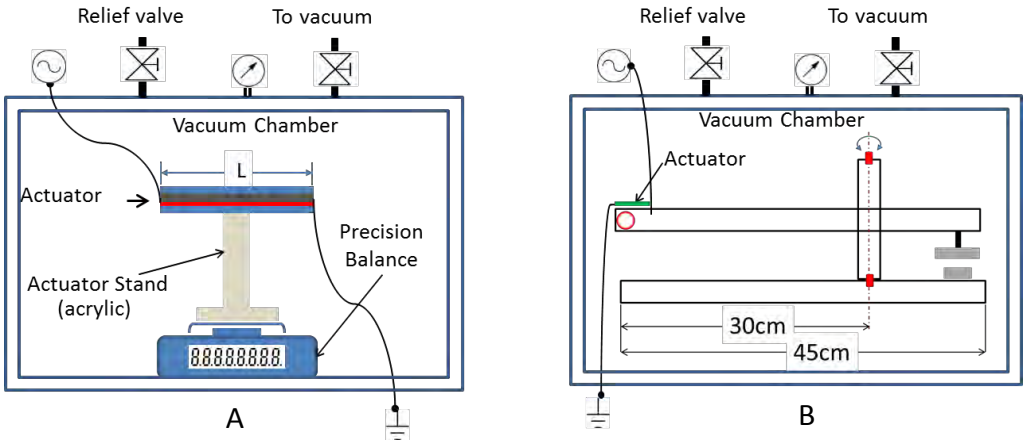

Figure 7-7. Experimental setup. A) Commercial Ohaus balance. B) APRG μNTS

7.2.2 Power supply setup

DBD actuators typically require an alternating potential of several kilovolts at kilohertz frequencies across the electrodes to initiate a discharge. To achieve this, a signal of desired shape and frequency (sine in this case) is generated using a Tektronix AFG3022B function generator. This signal is stepped up using a Crown CDi4000 audio amplifier for a gain of around 24. Further amplification by a gain of 220 takes place

through a high-voltage transformer (Corona Magnetics, Inc. CMI 5523). A current probe (Pearson Electronic 2100) and a high voltage probe (Tektronix P6015A) capture the current and voltage data through a digitizing oscilloscope (Tektronix DPO2014). Figure 7-8 schematically illustrates this setup. Power consumed was post processed using the current and voltage signals acquired through a LABVIEW interface.

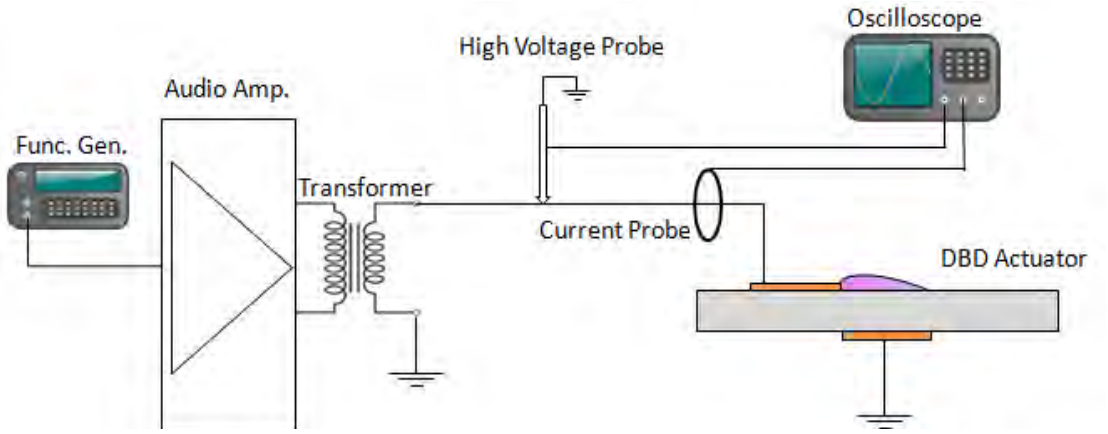

Figure 7-8. Two-stage amplification scheme used for powering the actuators

7.3.3 Actuators

In the present work, two types of actuators have been tested due to different space constraints on the two for measurement setups. For the Ohaus balance setup, the actuators are 30cm in length, with 5mm wide powered electrodes and 12.5mm wide ground electrode. The actuators tested on the μNTS setup are 4cm in length, with 5mm wide powered and ground electrodes. In all cases, the upstream edge of the powered electrode is covered with Kapton tape to prevent reverse discharge, and the ground electrode is covered with either several layers of insulation tape or hot glue, depending on operating voltage. The electrodes themselves made of 40 micron thick copper tape. Figure 7-9 illustrates the configuration of the two designs, and Tables 7-1 and 7-2 provide details of the dielectrics tested and the parameters studies.

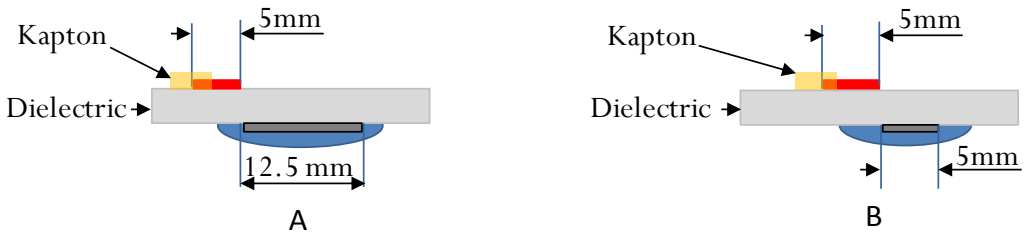

Figure 7-9. Electrode configuration for the actuators. A) Ohaus balance setup. B) μNTS setup.

Table 7-1. Details of the actuators tested on the Ohaus balance

Material	Thickness (mil, mm)	Length (cm)	Voltage (kVpp)	Frequency (kHz)
Teflon	10 mil 31.25 mil 62.50 mil 125.0 mil	30	6 8 12 15, 16, 17, 18, 20	14
Garolite*	1.56 mm	12	20	5

* The Garolite actuator has 15mm powered and ground electrodes with 1mm gap to match reference actuator

Table 7-2. Details of the actuators tested on the μNTS

Material	Thickness (mil, mm)	Length (cm)	Voltage (kVpp)	Frequency (kHz)
Kapton	2 mil	4	3	14
Teflon	5 mil 10 mil		6	
Glass	1 mm		10	

To ensure reliability, the experimental setup was benchmarked again published results. The benchmark case (Abe, Takizawa, & Soto, 2008) used 1.8mm thick fiberglass epoxy strip as dielectric, with 15mm wide powered and ground electrodes with 1mm gap. The actuator length was 30cm. The current actuator is a strip of 1.56mm thick fiberglass (Garolite, grade 10), with the same electrode configuration, except length, which is 12cm. The operating voltage and driving frequency are identical (20 kVpp, 5kHz). Figure 7-10 shows the actuator force with varying pressure.

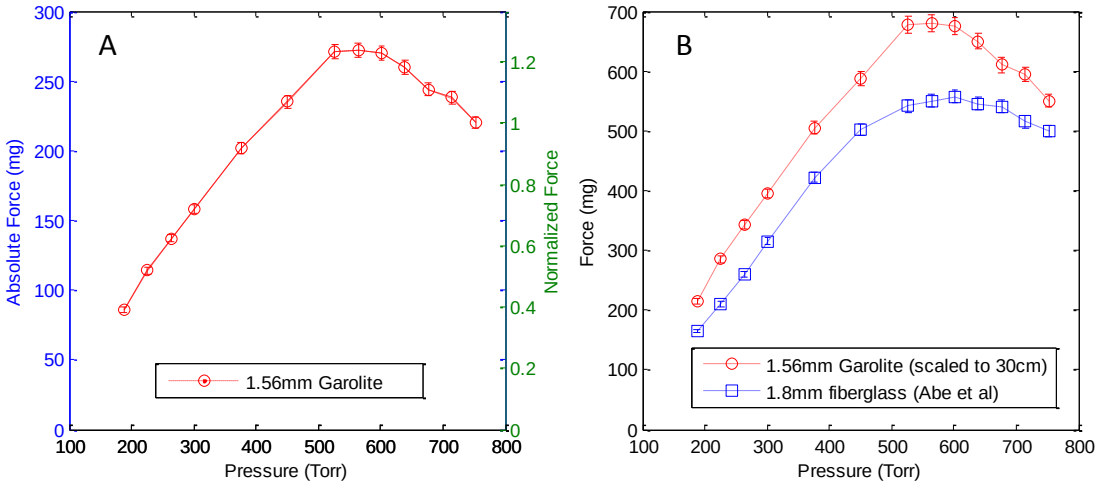

Figure 7-10. Benchmark Force v. Pressure trend for Garolite dielectric. A) Absolute and normalized force. B) Comparison with Abe et al (2008)

7.3 Results for Low Pressure DBD Actuation

From the results of the benchmarking experiment, it is seen that the force versus pressure trend agrees quite well with published literature (Abe, Takizawa, & Soto, 2008), However there are two quantitative differences. First, the increase in force (before it starts reducing again) is more pronounced in the present case (23% vs. 10%). Second, the thrust values obtained herein are higher overall by 100mg or more. This anomaly may be due to the difference in the dielectric thickness, length of the actuator, and the dielectric material itself (benchmark actuator uses glass-fiber-reinforced epoxy, whilst the actuator tested herein uses Garolite grade G-10). This has been further confirmed by results presented in subsequent paragraphs.

Having verified the benchmark case, tests were conducted on the actuators listed in Table 7-1. Teflon was chosen as the dielectric due to easy availability in varied thicknesses easiness to work with. Figure 7-11 below shows the force versus pressure trend for 4 different thicknesses of Teflon.

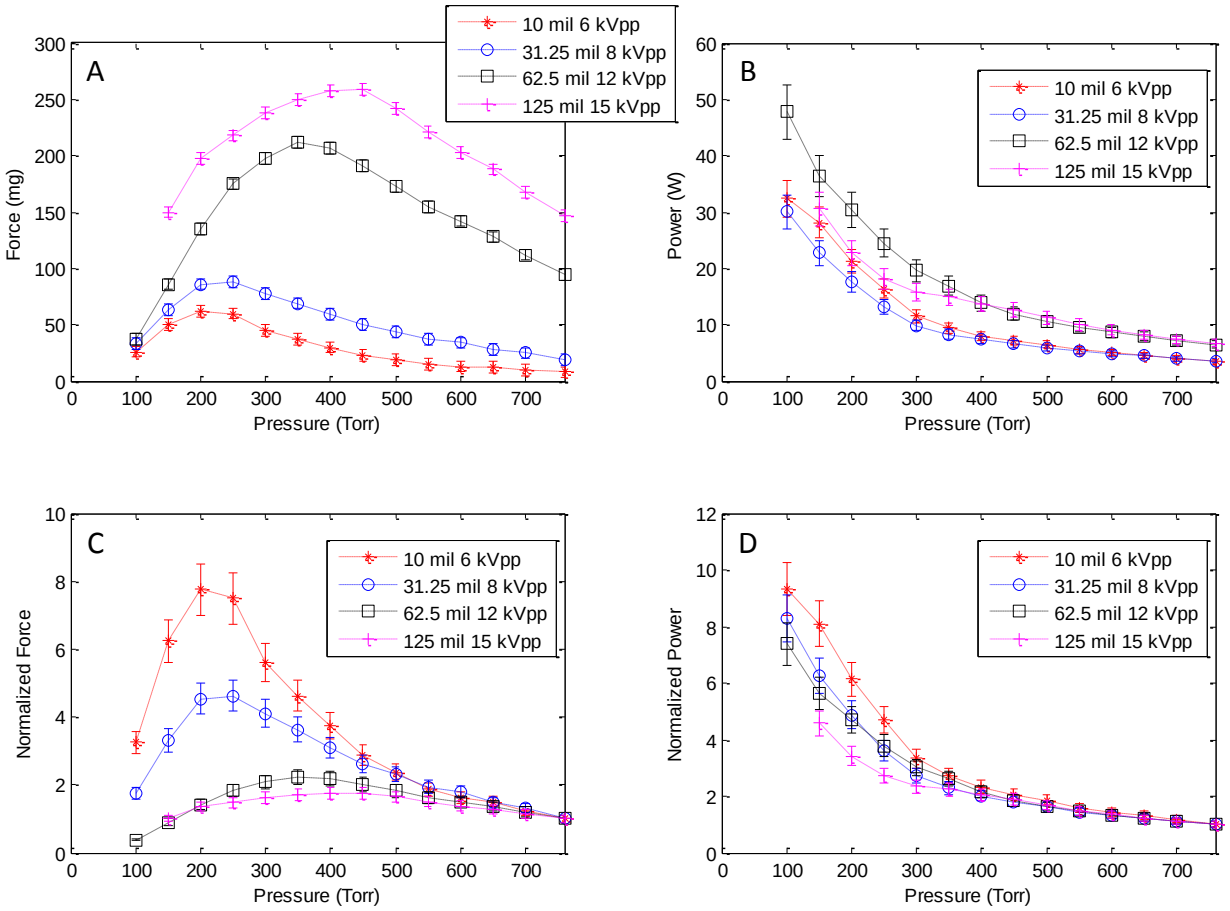

Figure 7-11. Force and Power trend for various thickness of Teflon dielectric. A, B) Absolute force and power. C,D) Normalized force and power

The following conclusions can be drawn from the above plots:

- For each thickness, the force reaches a maxima at a pressure lower than atmospheric. However, the pressure at which this maxima occurs shift lower as the dielectric thickness decreases. For instance, for 123 mil thick Teflon, maximum force occurs at a pressure of about 425 Torr, whereas for the 10 mil thick Teflon, this occurs at about 200 Torr.

- The percentage increase relative to the force at ambient pressure (called the ambient force henceforth) increases with decreasing thickness, reaching several-fold for thinner dielectric. For instance, for 125 mil Teflon, the peak force is only about 1.23 times the ambient force, whereas for 10 mil Teflon, the peak force is almost eight-fold.

- The power consumption increases at lower pressure, as predicted by Gregory and confirmed by Gregory and Abe. However, how much the power increases is a function of the dielectric thickness. For 125 mil Teflon, the power increases over 4-fold as the pressure goes down from ambient down to 1o Torr, however

for 10 mil thick Teflon, there is a 9-fold increase in power over a pressure range of atmosphere down to 100 Torr.

It is interesting to note that from current data, the power consumption is not seen to increase in proportion to thickness. However this conclusion is susceptible to the fact that the operating voltages are not the same for all the dielectric thicknesses. The experimental setup has constraints on the upper and lower limits on the voltage determined by the power supply arrangement (arcing), the dielectric strength (electrical breakdown), and minimum voltage needed to produce a readable force. This excluded the possibility of operating the actuators at a uniform voltage.

However, a closer look at the power consumption data allows us to draw some useful conclusion about the effect of thickness on power consumption at lower pressures. The dielectric thicknesses of 10 mil and 31.25 mil have similar power consumption at ambient pressures, as do the thicknesses of 62.5 mil and 125 mil. However, as the pressure reduces, the thinner of the two dielectrics in either pair undergoes a higher increase in power consumption than the thicker one. This is corroborated by the fact that the force increase at lower pressures is more pronounced in thinner dielectrics.

Since the force has an inflexion point while the power increases continually, this suggests the effectiveness (ratio of thrust to power) might also exhibit a local maximum. Figure 7-12 shows the absolute and normalized effectiveness for the four dielectric thicknesses tested.

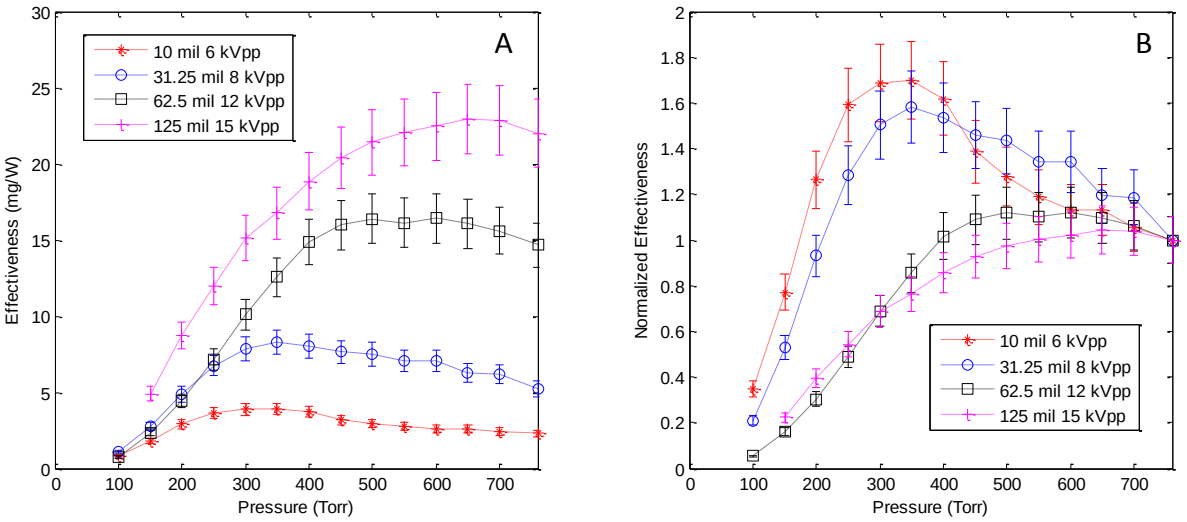

Figure 7-12. Effectiveness v. pressure trend for various thickness of Teflon dielectric. A) Absolute effectiveness. B) Normalized by reference values.

We see that, as expected, the effectiveness has a maxima, the pressure location of which depends on the dielectric thickness. Also, as observed in the force trend, the gain at peak effectives is lower for higher dielectric thicknesses, reflecting the force trend. The thickest dielectric (125 mil) sees barely a 5% improvement at force maxima, but the thinnest (10 mil) dielectric sees an improvement of upto 70% at the pressure corresponding to force maxima.

The presence of a force and effectiveness optima suggests that DBD actuators can be optimized base on anticipated operating conditions. For instance, the plot of absolute effectiveness suggests that at pressures less than 250 Torr, a 31.25 mil thick Teflon actuator operating at 8 kV has the same effectiveness as a 62.5 mil actuator operating at 12 kV.

Figure 7-13 shows the force-versus-pressure trend for a given dielectric thickness (125 mil Teflon) at varying operating voltages.

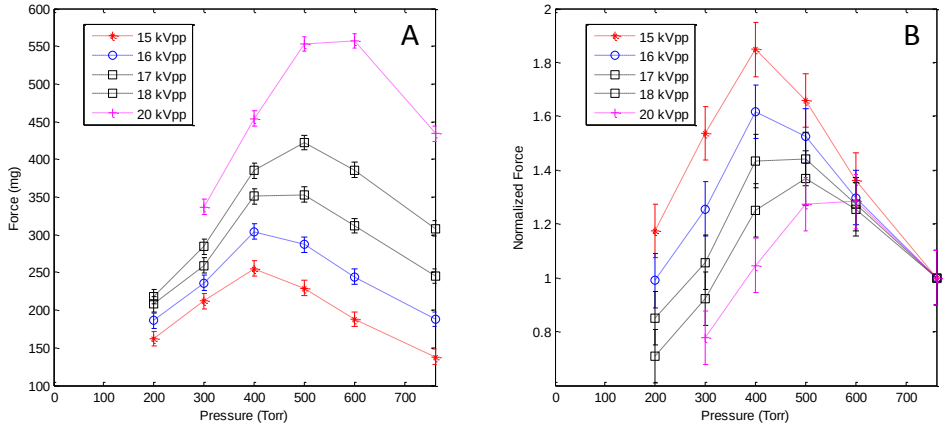

Figure 7-13. Force v. pressure trend for operating voltages for 125 mil Teflon dielectric. A) Absolute. B) Normalized by ambient values.

The plots suggest a voltage dependence on the pressure at which the force maxima occurs. This pressure shift more towards the ambient pressure as the voltage increases (400 Torr at 15 kVpp vs 575 Torr at 20 kVpp). Also, the gain in the force reduces as the voltage increases (80% at 15 kVpp vs 30% at 20 kVpp), as apparent from the normalized force plots. Of particular interest is the 1.58 mm thick Teflon actuator operating at 12 kVpp, which is under a similar nominal electric field as the 3.17 mm Teflon operating at 20 kVpp (3.80 MV/m vs. 3.15 MV/m). The thinner dielectric of the two is found to undergo higher force amplification (220% vs. 30%), suggesting thinner dielectrics might be better suited for high-altitude/low-pressure operation.

The results presented so far were for longer actuators (~30 cm) tested on a commercial precision balance with a resolution of 1 mg. For actuators only a few centimeters long, the force produced is either less or just of the order of the resolution of the balance, leading to unacceptable error margins. To this end, a couple of smaller actuators (listed in Table 7-2) were tested on the μNTS. The resolution of the thrust stand has already been validated by measuring thrust from microactuators (Zito, Durscher, Soni, Roy, & Arnold, 2012a).

Figure 7-14 shows the force versus pressure trend for the μNTS actuators. The trend seems to agree with the one from the commercial balance. The force peaks at a sub-atmospheric pressure before dropping down again. Of particular interest is the plot for 10 mil Teflon actuator operated at 6 kV. This actuator (4 cm length) has a similar configuration to the one tested on the commercial balance (30cm length). The force trend on the commercial balance suggested a nearly eight-fold increase at a pressure of 200 Torr. The results from μNTS validate this gain in force, albeit at a different value of pressure in this case (300 Torr). This hints towards a dependence on either the length of the actuators or the width of the ground electrode, which needs experimental verification.

The power consumption, on the other hand, keeps increasing non-linearly before tending to slope off at lower pressures. This is in contrast to the larger actuators where the power keeps increasing non-linearly as the pressure goes down. This might have to do with the length of the ground electrode, which is 5mm for the shorter actuators, as against 12.5mm for the longer actuators. As the pressure goes down, the plasma grows in extent (as shown in Fig. 7-15). However, once the plasma completely covers the extent of the ground electrode, it can expand no further, and instead grows stronger locally; evidently, this happens earlier for a shorter ground electrode than a longer one.

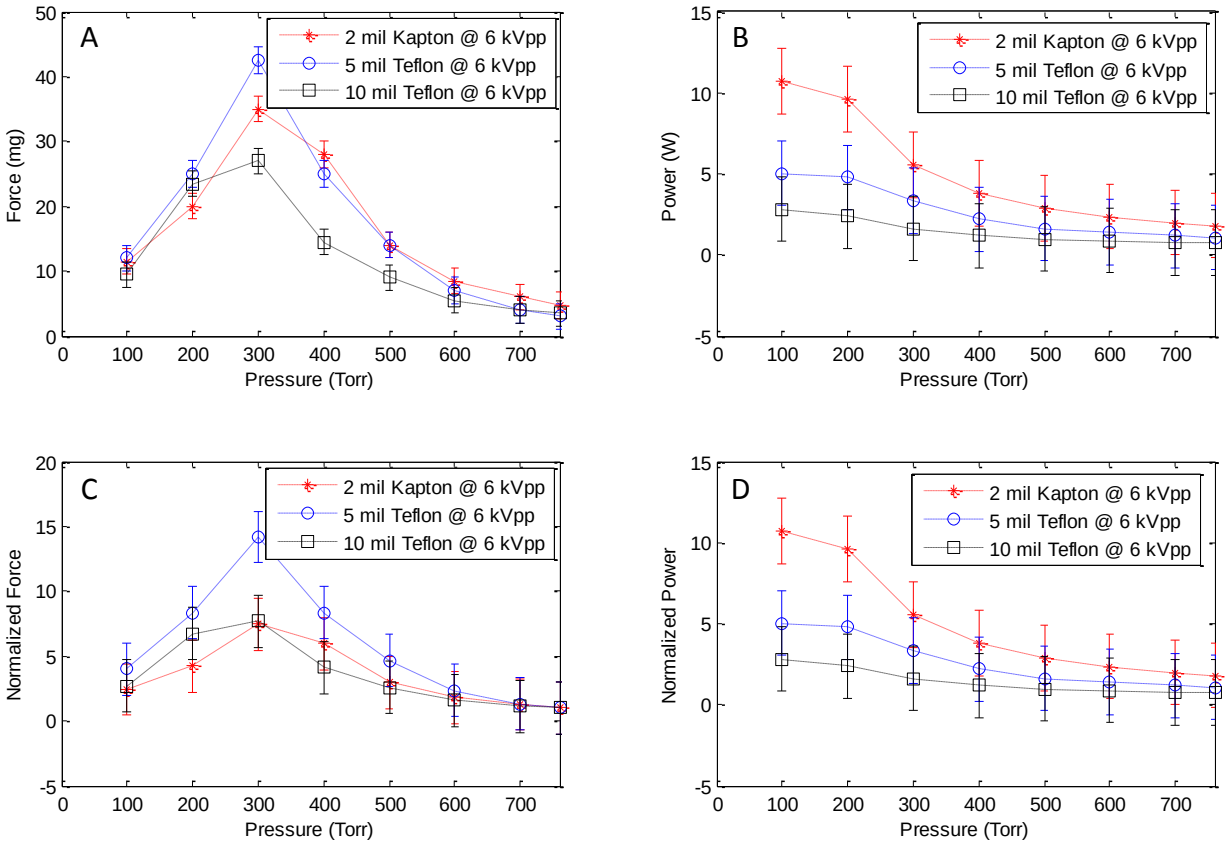

Figure 7-14. Force and Power trends for μNTS setup. A,B) Absolute. C,D) Normalized by reference values

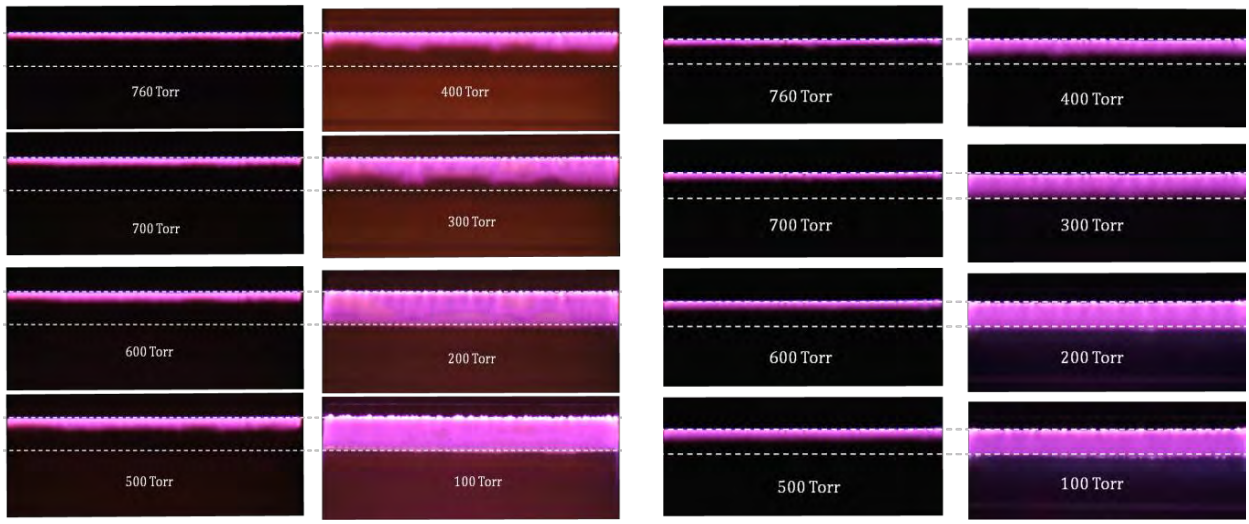

Figure 7-15. Plasma extent as a function of pressure. A) 2 mil Kapton. B) 5 mil Teflon

This trend is even more prominent in the case of glass dielectric, where the power starts flattening out much sooner, due to early spatial saturation of plasma (at ~

400 Torr) as evident form Fig. 7-16. The slight anomaly in the power at 100 Torr is due to the fact that at 10 kV at that pressure, the power supply arrangement is susceptible to direct plasma arcing between the powered electrode and the ground wire (bright plasma spot on the right), leading to higher power dissipation than expected. The bluish hue beyond the ground electrode is merely light dispersion/reflection from the glass plate.

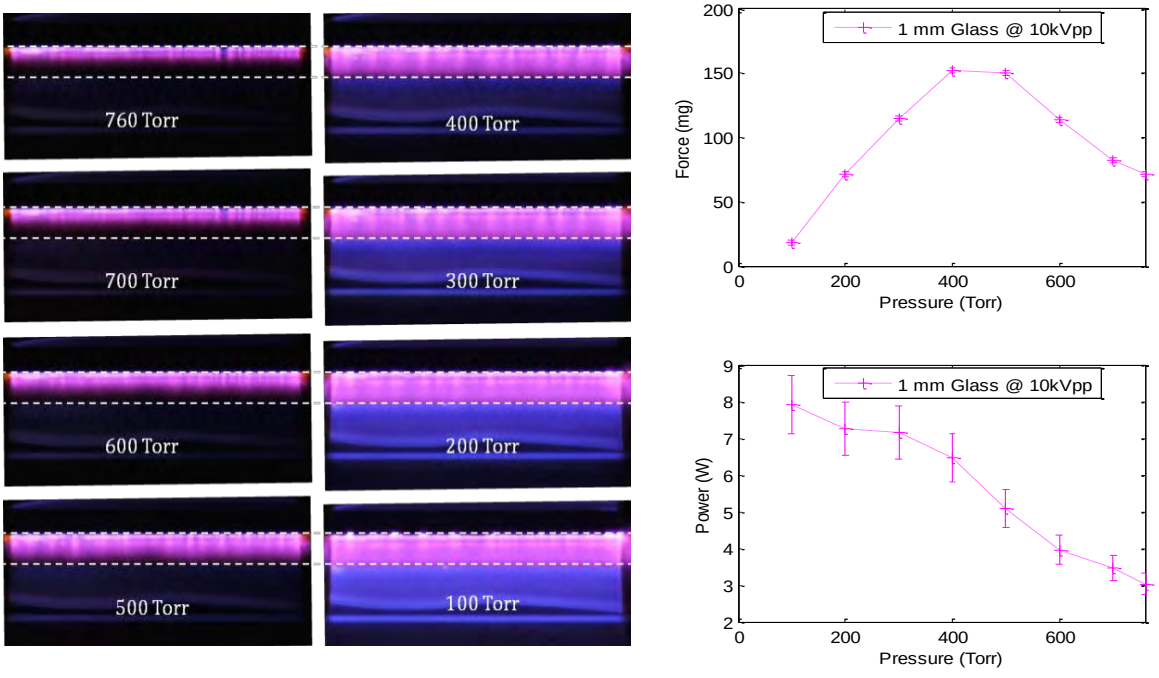

A B

Figure 7-16. Glass dielectric, 1 mm thickness. A) Plasma extent. B) Force and Power.

Figure 7-17 shows the absolute and normalized effectiveness of the actuators tested on the μNTS, which suggests the same qualitative trend as results from the commercial balance. Quantitatively, however, there is a noticeable difference over the two actuators tested over two balances.

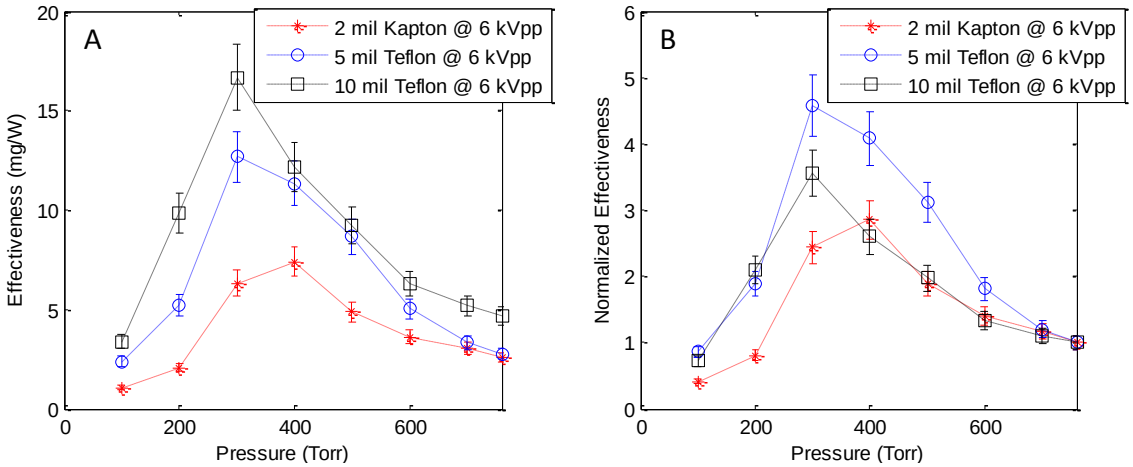

Figure 7-17. Actuator effectiveness as a function of pressure. A) Absolute. B) Normalized by reference values.

Figure 7-18 shows the absolute and normalized effectiveness for 10 mil Teflon dielectric actuators with two different ground electrode configurations (5mm ground vs. 12.5mm ground). Firstly, the absolute effectiveness for the actuator with 5mm ground is noticeably lower compared to the actuator with 12.5mm ground. Secondly, the gain in effectiveness at lower pressure is more pronounced for the actuator with a shorter ground electrode. This might due to the face that once the plasma extent completely covers the ground electrode, instead of expanding downstream, it grows stronger locally, increasing the degree of ionization in the region of relatively stronger electric field, leading to a higher increase in force than a wider ground electrode, where the plasma keeps expanding further downstream until it completely covers the electrode.

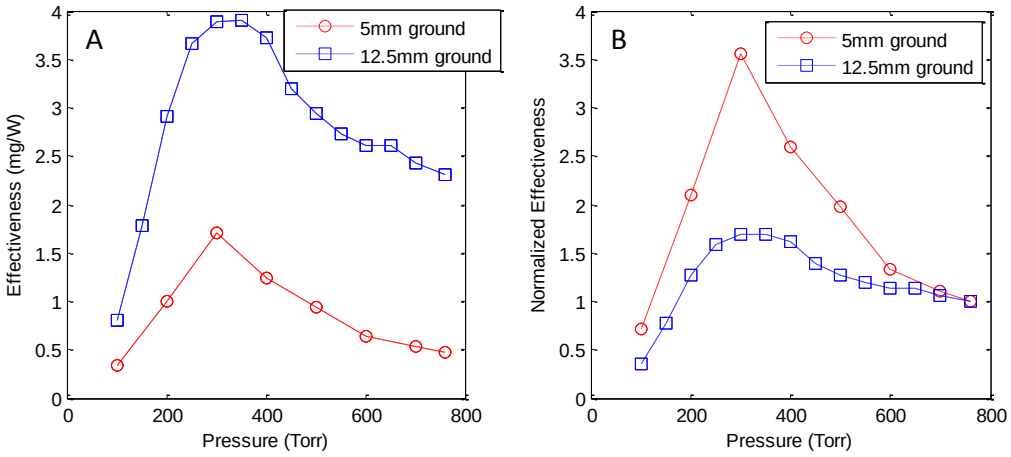

Figure 7-18. Effect of ground electrode width on effectiveness. A) Absolute. B) Normalized.

The systematic dependence of peak actuator thrust on dielectric thickness, and the pressure at which this occurs, hints towards a causal relationship. An attempt is made to capture this trend in a unified equation which relates these variables. Multivariate analysis in conjunction with curve-fitting suggests the following empirical relationships among the various parameters (Soni & Roy, 2013b):

$$P_{\mathrm{m}} = 11.43E \tag{7-2}$$

$$T_{\max} = 0.4e^{0.0437P_{\mathrm{m}}} + 0.585e^{0.428E} \tag{7-3}$$

$$T_{\max} = 6\left(\varepsilon_n^{0.5}\right)\left(1-e^{-w_n^{1.25}}\right)\left[0.4e^{0.0437P_{\mathrm{m}}t_n} + 0.585e^{0.428Et_n^{0.85}}\right] \tag{7-4}$$

Here P_m is the pressure (kPa) at which the thrust peaks, E is the nominal electric field (MV/m), T_{max} is the peak thrust per meter length (mN/m), t_n is the normalized thickness (t/t_{ref}), w_n is the normalized ground electrode width (w/w_{ref}), and ε_n is the normalized dielectric constant ($\varepsilon_r/\varepsilon_{ref}$). The reference values are t_{ref} = 3.17 mm, w_{ref} = 50 mm, ε_{ref} = 2.1.

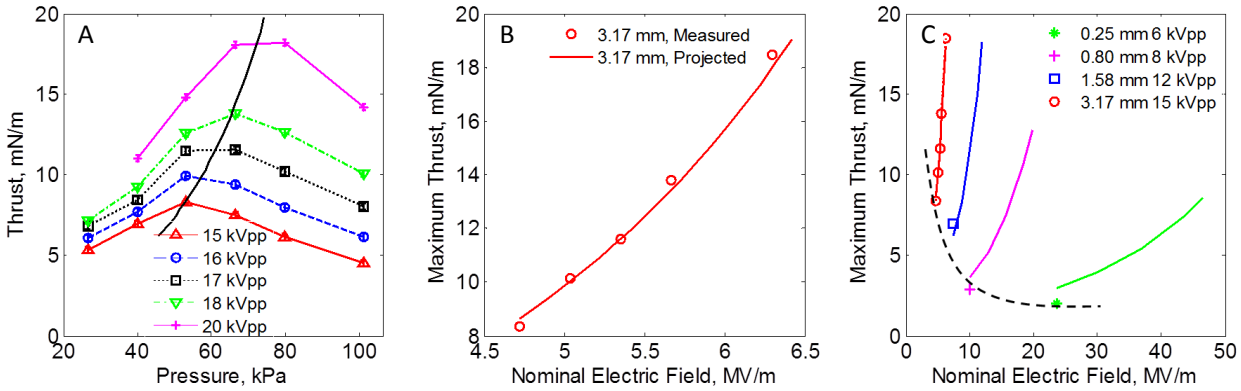

Figure 7-19. Comparison of empirical model with experimental data. A) Thrust per length at varying voltages for 3.17 mm thick Teflon dielectric (Solid black like represents Eq, 7-3). B) Maximum thrust as a function of nominal electric field, as captured by Eq. 7-3. C) Extension of this trend for various dielectric thicknesses using Eq. 7-3 (dashed black line represents approximate behavior of Eq. 7-4 for varying thickness; solid lines represent projections; marker locations represent experimental data (Soni & Roy, 2013b).

Equation 7-3 is plotted in Figure 7-19(A) (solid black line). The curve seems to mimic the peak force trend fairly well. For a given thickness (3.17 mm), the projected values from Eq. 7-3 match within 5% of the measured values (Figure 7-19(B)). To account for variation in thickness, dielectric constant, and ground electrode width, Eq. 7-3 is modified by introducing the normalized quantities t_n, ε_n, and w_n (Eq. 7-4). The projected values for 0.25 mm, 0.80 mm, and 1.58 mm Teflon dielectric using this revised equation (Figure 7-19(C)) are found to be within 16%, -4%, and -33%, respectively. The projected value for a different dielectric material, thickness, and ground electrode width (Garolite, 1.58 mm, 15 mm) are found to be within 14% of the measured value. Similar projections (Teflon, 0.13 mm and 0.25 mm thick, 5 mm ground, and Kapton, 0.05 mm thick, 5mm ground) are seen to be within 20% of the respective measured values, with the exception of Kapton, where Eq. 7-4 over-predicts the force by about 45%. This deviation can be explained considering the extremes of thickness (0.05 mm) and electric field (59 MV/m) that this actuator is under. Thrust saturation for

0.16 mm Kapton at 12 kVpp and identical frequency (14 kHz) has been reported in literature (Durscher & Roy, 2012). This corresponds to an electric field of approximately 36 MV/m. The electric field for the Kapton actuator in the current study is 60% higher than this value, suggesting the actuator is already operating in or beyond the thrust saturation region. Equation 7-4 does not account for any saturation phenomena, thus over predicting the value.

Figure 7-20 shows the current and voltage plots at various pressures. As the pressure goes down, the discharge spikes are seen to grow slightly in magnitude and frequency (upto 500 Torr), before become shorter and sparse at lower pressures. The phase angle at which the discharge spikes initiate also shift towards the left as the pressure goes down. At ambient pressures, the spikes begin at approximately 90° into the current signal phase. However at 100 Torr, this initiation takes places upto 45° earlier in the phase. This is complimented by another observation that the diffuse discharge present during the negative half cycle at ambient pressures is nearly absent at lower pressure. This suggests that ambient pressures, strong plasma is produced for the entire duration of the positive-rising voltage pulse, whereas only a weak discharge is produced during the negative-going duration of the cycle. At low pressure however (100 Torr), plasma starts forming while the voltage is still negative but rising, and lasts till the voltage reaches the peak value. There is no significant discharge during rest of the cycle.

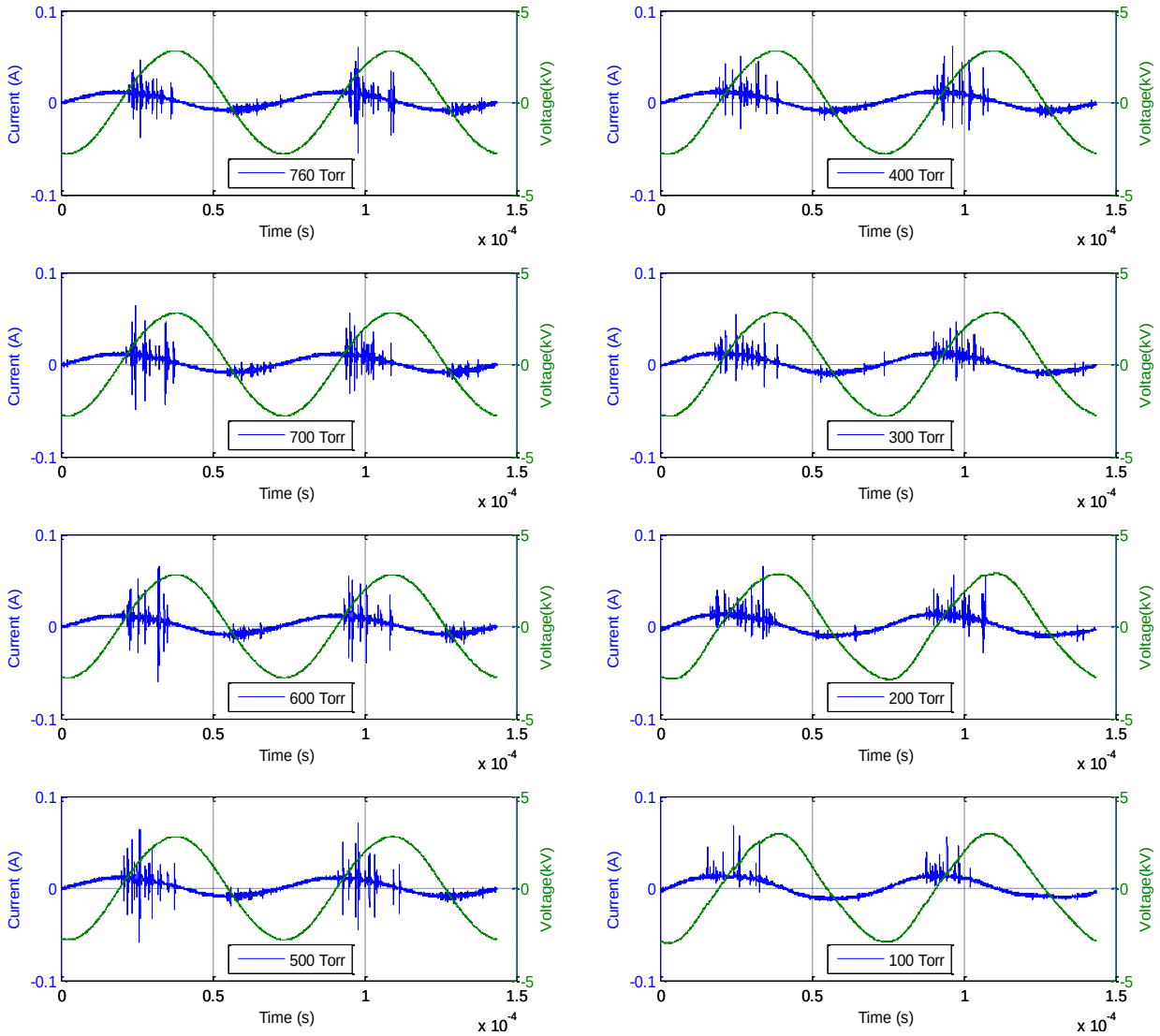

Figure 7-20. Current and Voltage profiles art different pressures for a 10mil Teflon dielectric, 14 kHz, 6 kVpp.

The FMEJ intends to use principles of DBD actuators to achieve flow acceleration for thrust generation. Existing literature does not sufficiently address the behavior of DBD actuators under the operating conditions of interest to FMEJ, primarily low pressure. It is towards this end that low pressure characterization of DBD actuators has been carried out. Results suggest decreasing efficiency of DBD actuators at reduced pressures. In view of these findings, it may be of interest to investigate methods to increase the low pressure performance of these devices.

CHAPTER 8
EFFECT OF TEMPERATURE ON DBD ACTUATOR PERFORMANCE

DBD actuators have found possible applications in a wide avenue of aerospace applications. Actuators have been demonstrated to alleviate flow separation and stall over airfoils, which lends them to direct application to aircrafts. The operational regime of aircrafts subjects them to atmospheric temperature variations with varying altitude. To adapt DBD actuators meant for high altitude operations, it is imperative to understand their performance under varying ambient temperatures

8.1 Role of Temperature on Actuator Performance

The force/flow inducement mechanism for DBD actuators can be compartmentalized into two processes. The first one is ionization which is responsible for the production of force carrying species. The second is the fluid interaction which transfers the momentum from charged to neutral species, and in case of force measurement, onto the dielectric surface by viscous interactions. Temperature variations effect both these phenomenon.

The Paschen breakdown voltage for a gas is known to be a strong function of temperature. A study conducted on corona discharge (Uhm, Jung, & Kim, 2003) found the breakdown voltage to be an inverse function of the gas temperature. The linear relationship was found to follow the relationship

$$V = \frac{T_0}{T} V_0 \tag{8-1}$$

Where V is the breakdown voltage and T is the gas temperature in Kelvin, and the subscript 0 denotes reference condition, which in the cited study was the ambient temperature of 300 K. This was experimentally verified for air (Figure 8-1) as well as nitrogen.

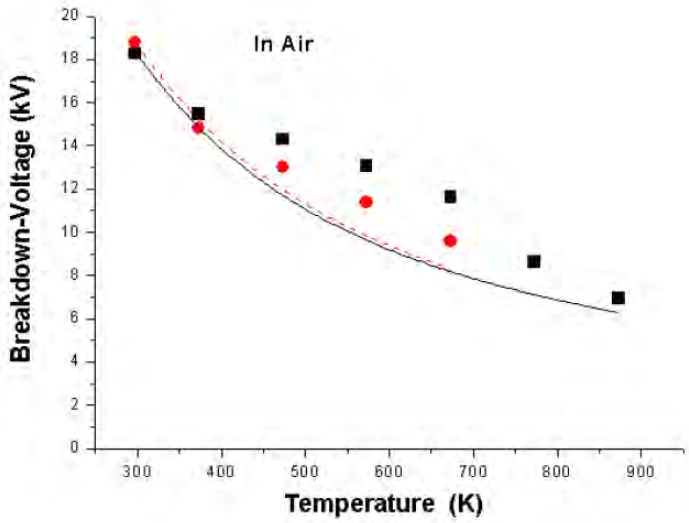

Figure 8-1. Effect of gas temperature on breakdown voltage for air (Uhm, Jung, & Kim, 2003).

The other mechanism by which temperature affects the flow/force characteristics of plasma actuators is via viscosity. The air viscosity determines the peak velocity and the boundary layer profile for a given amount of momentum energy dumped into the system by the wall jet. The net induced actuator force that is measured is the plasma force less the wall shear. This wall shear is a direct function of the viscosity since the induced force is given by

$$F_{induced} = F_{plasma} - \mu \left. \frac{\partial u}{\partial y} \right|_{wall} \tag{8-2}$$

The viscosity of a gas is an aggregate measure of the momentum dissipation by inelastic collisions. The parameters of these collisions such as collision cross sections, frequency, and mean free path depend on the average velocity of the molecules, of which temperature is an aggregate measure. The temperature dependence of viscosity of a gas is given by the Sutherland law, which is expressed as

$$\mu = \mu_{ref} \left(\frac{T}{T_{ref}} \right)^{3/2} \frac{T_{ref} + S}{T + S} \tag{8-3}$$

where μ and T are the viscosity and temperature of the gas respectively, S is the Sutherland constant, and the subscripts *ref* refers to reference condition. Figure 8-2 shows the variation of dynamic viscosity for air between the temperatures of 200-300 K.

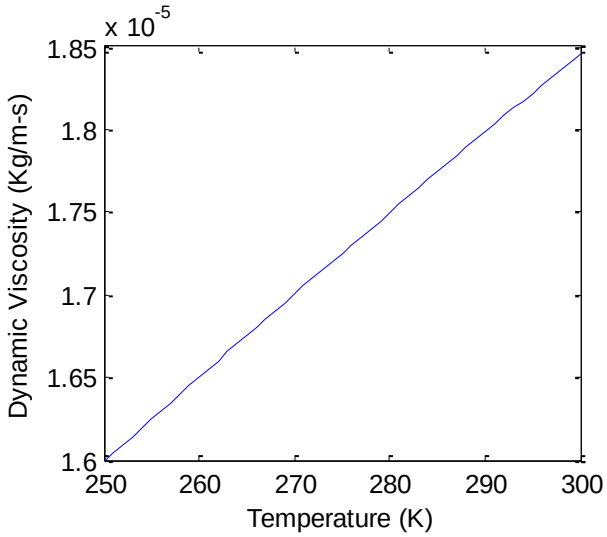

Figure 8-2. Dynamic viscosity of air as a function of temperature.

Apart from ambient temperature, the temperature of the dielectric itself plays a crucial role in the actuator performance. An oscillating electric field applied to a dielectric results in heating due to molecular polarization and hysteresis. As the actuator runs for a long time, the dielectric temperature increases gradually until it reaches steady-state with the heat generated balanced out by conductive, convective, and radiative losses. The amount of this heating depends directly on the applied electric field. In case of plasma actuators, the presence of plasma close to the dielectric is an additional source of heating. As discussed, the electron temperature in DBD actuators is of the order of several eVs. A strong plasma close to the dielectric can cause significant localized heating by heavy electron bombardment.

The effect of dielectric temperature on actuator performance has been reported in literature. One such study (Wilkinson, et al., 2014) measured the change in frequency

dependent dielectric constant of actuators materials with increasing temperatures. The results, reproduced in Figure 8-3, suggest that the dielectric loss tangent (tan δ) could be a strong function of temperature depending of the dielectric under question. The power loss in a dielectric can be shown to depend on the loss tangent as (Durscher R. J., 2012)

$$P_{loss} = 2\pi f \varepsilon_r \varepsilon_0 E^2 \tan\delta \tag{8-4}$$

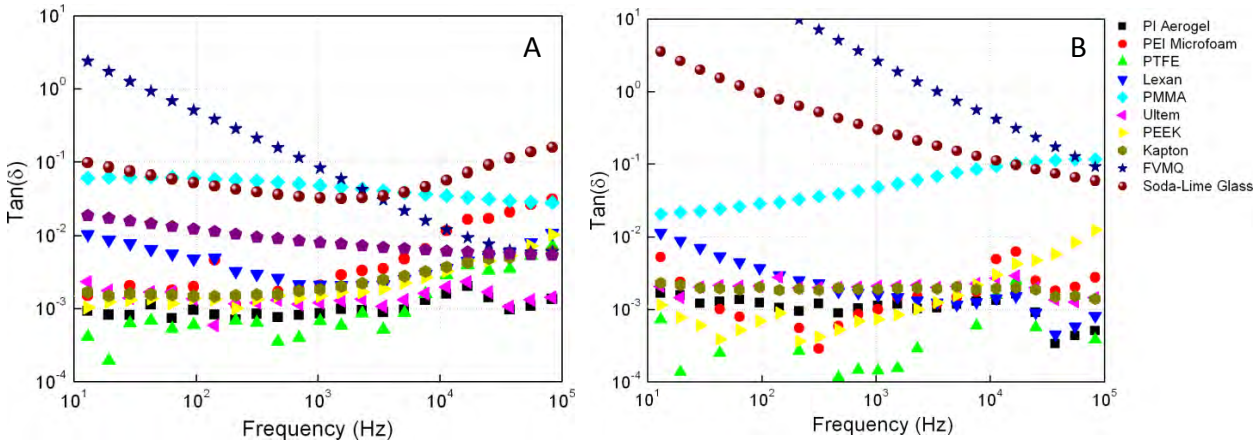

Figure 8-3. Loss tangent for various dielectric as a function of frequency and temperature. A) at 30 °C. B) at 120 °C (Wilkinson, et al., 2014).

8.2 Literature Review of Temperature Effects on Plasma Actuators

There has been limited quantitative research on the role of temperature in plasma actuator performance. Several researchers have studies self-induced dielectric heating (no external heat source) and have reported spatial and temporal temperature evolution over the dielectric surface using IR imaging. Results indicate that at atmospheric pressure, the dielectric surface does not heat up by more than 20 °C for the dielectrics tested (Figure 8-4).

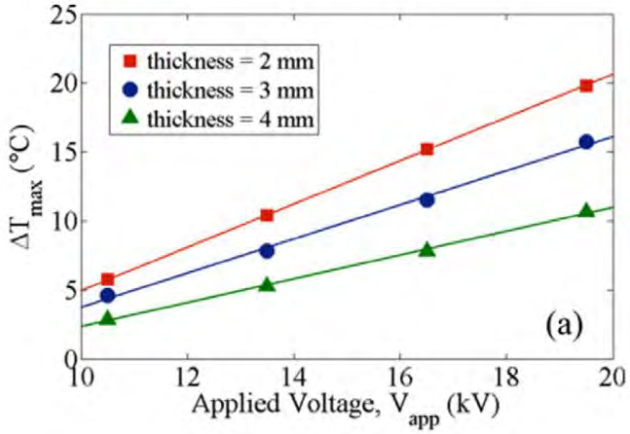

Figure 8-4. Steady-state dielectric temperature as a function of dielectric thickness and operating voltage (Tirumala, et al., 2014)

The effect of externally-induced dielectric heating has been reported in literature. In one such study, the dielectric was either cooled or heated with dry ice or a Peltier module respectively, and the induced velocity was measured using PIV. Results indicated a strong dependence of velocity on dielectric temperature, with increasing temperature resulting in increased velocity (Figure 8-5).

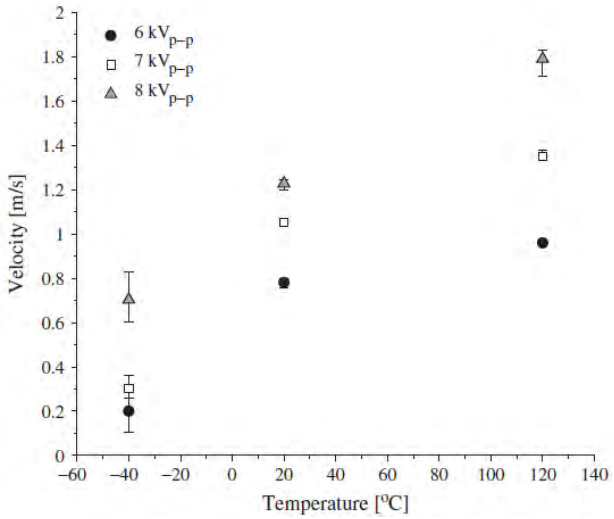

Figure 8-5. Effect of dielectric temperature on induced velocity at different operating voltages. (Erfani, Zare-Behtash, & Kontis, 2012)

The effect of ambient temperature on actuator performance has been reported in literature. Increasing the ambient temperature was found to increase the induced force significantly, with the increase seen to be a linear function of temperature (Figure 8-6).

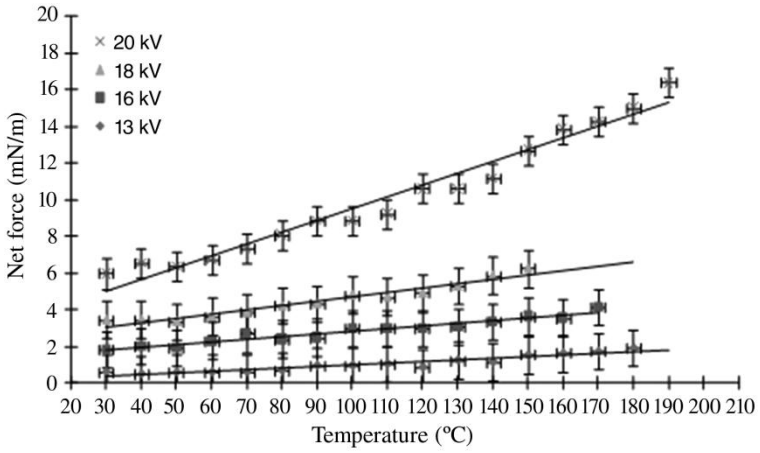

Figure 8-6. Effect of ambient temperature on induced force at different operating voltages. (Versailles, Gingras-Gosselin, & Duc Vo, 2010).

However, literature about the effect of dielectric heating at reduced pressures as well as the effect of ambient air temperature on induced thrust has not been reported anywhere. Self-induced dielectric heating at reduced pressures is important due to several reasons. It is known that, for a fixed voltage, the actuator draws more current, as evinced by increased power consumption and stronger plasma region (Soni & Roy, 2013b).Furthermore, the reduced ambient air density alters the free convection on the rear surface and the forced convection by the wall jet on the front surface. Since the dielectric constant is known to be a function of temperature, it's important to assess the change in dielectric temperature at reduced pressure under prolonger operation. Furthermore, the effect of reduced ambient air temperature on the induced thrust also needs to be assessed.

8.3 Effect of Ambient Temperature on Actuator Performance

To assess the effect of ambient air temperature on the induced thrust, a conventional SDBD actuator with 3mm thick acrylic dielectric (ε_r = 3) was mounted on an Ohaus precision balance (Adventurer Pro 3133C, 1 mg resolution). The powered and ground electrodes were made of copper tape 5mm and 20mm wide respectively. The actuator was powered using the two-stage amplification scheme of Figure 7-8. The operating frequency was 5 kHz and the voltage was varied between 14 and 26 kVpp. The actuator was connected electrically with 36 AWG leads to reduce the influence on force measurement. The entire setup was placed inside the Thermal Vacuum Test Facility on an insulating bed to prevent direct contact with the cooling plate to minimize thermal stresses on the balance. The Thermal Vacuum Test Facility is essentially a cylindrical vacuum chamber (1m diameter x 2m length) with a thermal heating/cooling place the bottom inside the chamber. Cooling of the chamber is achieved by passing liquid nitrogen through the cooling pipes whilst maintaining the plate at a fixed temperature. The air inside the chamber cools primarily by convection, however at very low pressures radiation becomes the dominant mechanism. During cooling, the location of the plate at the bottom establishes a thermal gradient as the cold air settles down and the warm air remain at the top. To alleviate this, a small 12 V fan was installed inside the chamber and turned on periodically to promote homogenization. A surface thermocouple was used to measure the cooling plate temperature while an ambient thermocouple monitored the air temperature close to the plasma actuator. The plate was cooled to a fixed temperature (-60 °C) and force measurements were taken at various ambient temperatures as the air temperature dropped. The mixing fan was

switched off during force measurements to avoid turbulence inside the chamber from effecting the measurements. The temperature was found to fluctuate within 1 ˚C of intended temperature during readings. The whole setup is illustrated in Figure 8-7 schematically.

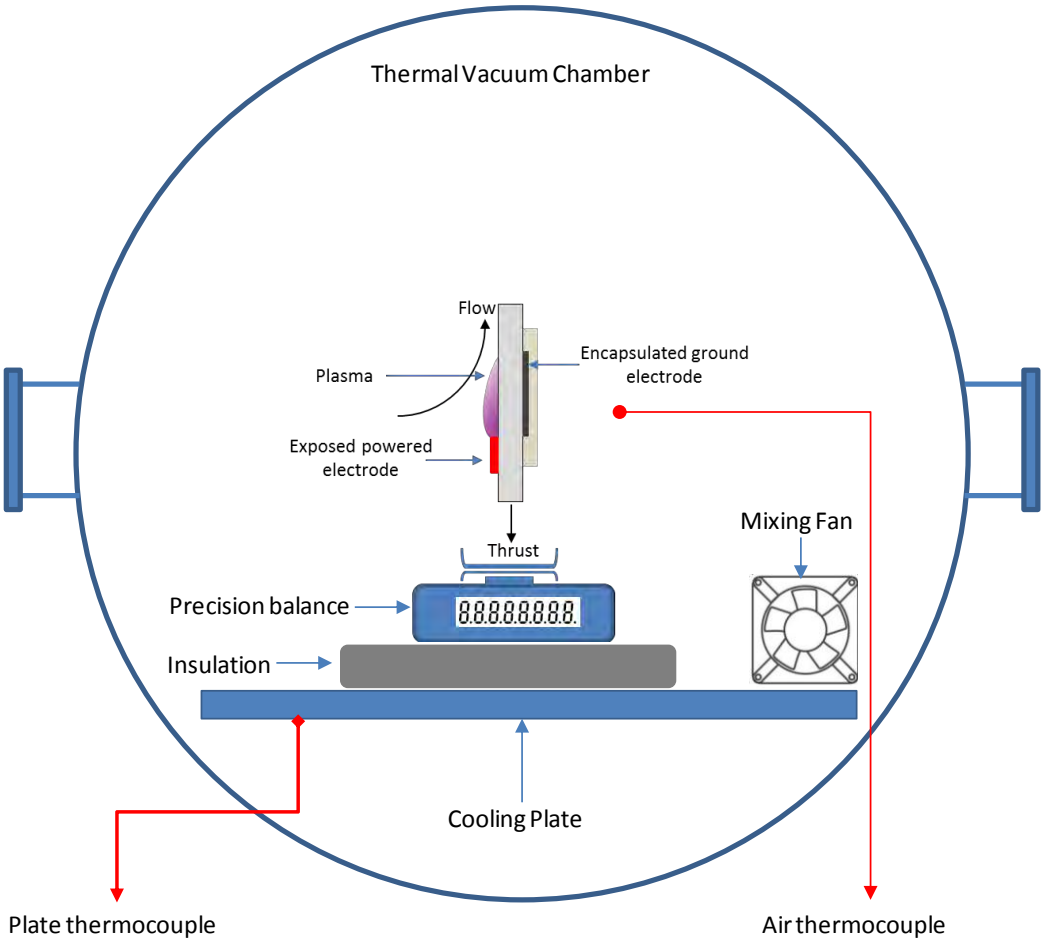

Figure 8-7. Schematic of the experimental setup for thermal tests.

Results from the experiment are shown in Figure 8-8. Force measurements were made at temperatures of ranging from 0 to 20 °C and at voltages from 14-26 kVpp. Results suggest a mild but proportional dependence of actuator force on air temperature. The force is seen to decrease with decreasing temperature. The change is barely evident at low voltages but more pronounced at higher voltages, suggesting a non-linear effect of temperature depending on operating voltage. For instance,

operation at 14 kVpp showed no change in induced thrust, whilst at the two highest voltages of 24 and 26 kVpp, the force dropped by 20% and 15% respectively as the temperature dropped from 20 °C to 0 °C.

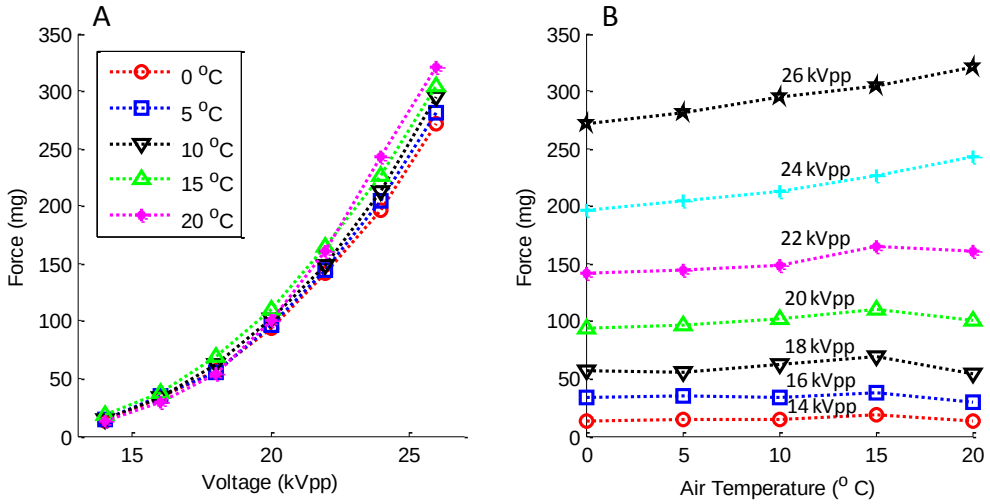

Figure 8-8. Effect of ambient air temperature on induced thrust at different voltages. A) Force v. voltage at constant temperature. B) Force v. temperature at constant voltage

Based on Eq. 8-1, as the temperature drops from 20 to 0 °C, the breakdown voltage of air increases by about 8%. Considering that the relationship between induced thrust and voltage is highly nonlinear ($F \propto V^{\sim 3.5}$), an 8% increase in the breakdown voltage could easily set back the thrust by a higher margin. Simultaneously, the viscosity of air decreases by about 5% based on the Sutherland law. The change in viscosity also has a non-linear effect on wall shear since it changes the velocity profile and hence the velocity gradient at the wall.

Based on the trend of breakdown voltage, and the results from induced thrust at reduced air temperature, it is evident that the thrust from plasma actuators suffers noticeably. Considering that the FMEJ is expected to operate in an orbit where the

temperatures could be significantly lower than atmospheric, this behaviors should be kept in mind for any actuators design to operate at high altitudes or in orbit.

8.4 Effect of Pressure on Dielectric Heating

To study the effect of dielectric heating as a function of pressure, three different thicknesses of Garolite (62.5 mil, 93.75 mil, and 125.0 mil) were tested at pressure ranging from 760 down to 200 Torr. The actuators were made of 2” x 6” dielectric plates, with 5mm powered and 20mm powered electrodes. The temperature of three plasma actuators was monitored as a function of time at different pressures. The temperature was monitored using a K-type thermocouple (accuracy ±0.75 ˚C) mounted on the backside of the actuator 1 cm downstream from the edge of the ground electrode as shown in Figure 8-9. The actuators were placed inside an acrylic vacuum chamber (22” x 10” x 9”), which was connected to a mechanical vacuum pump. Desired level of vacuum was maintained using a flow control valve between the pump and the chamber. The pressure was monitored using a MKS 910 Piezo Pirani pressure gauge and was maintained within ±5 Torr at any given pressure.

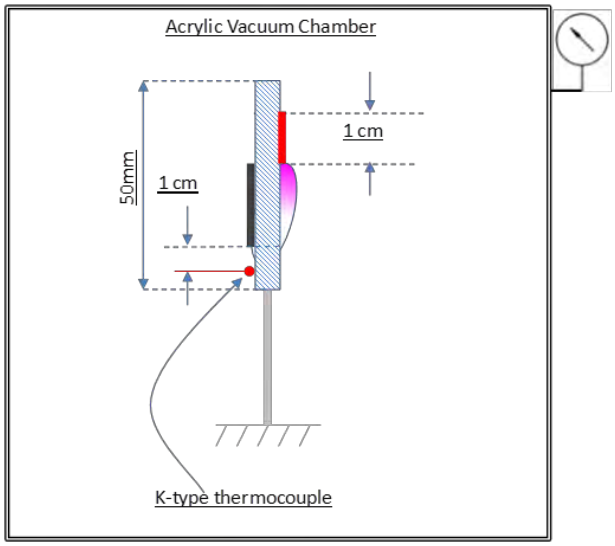

Figure 8-9. Experimental arrangement for measuring dielectric temperatures at low pressure.

The results from this experiment are shown in Figure 8-10. The temperature is plotted as a function of time at different pressures for the three different thicknesses. It is seen that, as expected, the steady state dielectric temperature increases as the pressure goes down. Visual evidence corroborates that the plasma grows stronger while drawing a higher current, leading to a higher joule heating of the dielectric. Concurrently, the reducing gas density diminishes convection losses hence trapping the heat generated inside the dielectric.

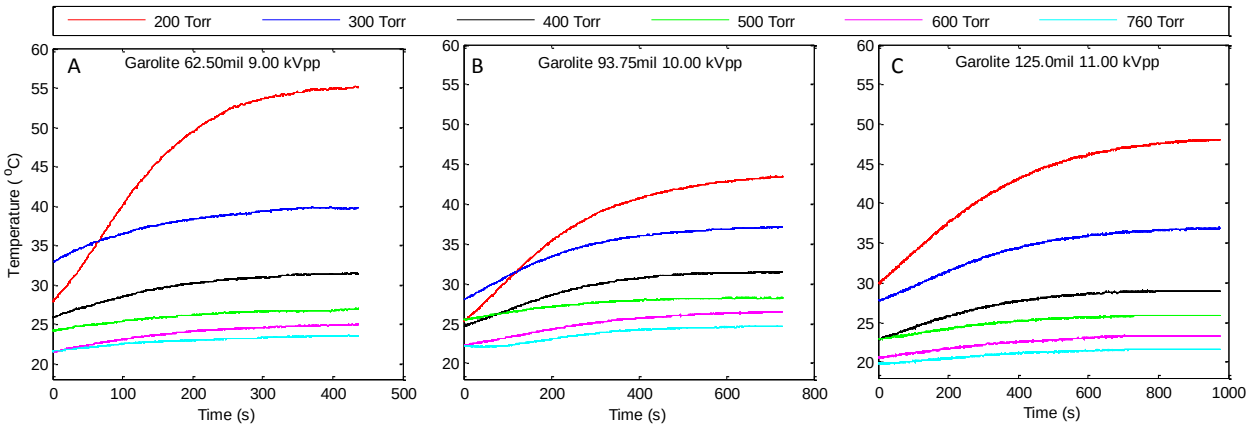

Figure 8-10. Dielectric temperature as a function of time for Garolite at different pressures. A) 62.50 mil at 9.00 kVpp. B) 93.75 mil at 10.00 kVpp. C) 125.0 mil at 11.00 kVpp.

Figure 8-11 shows the steady-state temperature of the three thicknesses of the dielectric. The temperature is seen to increase non-linearly as the pressure goes down, which corroborates with the fact that the power consumed grows in a similar manner.

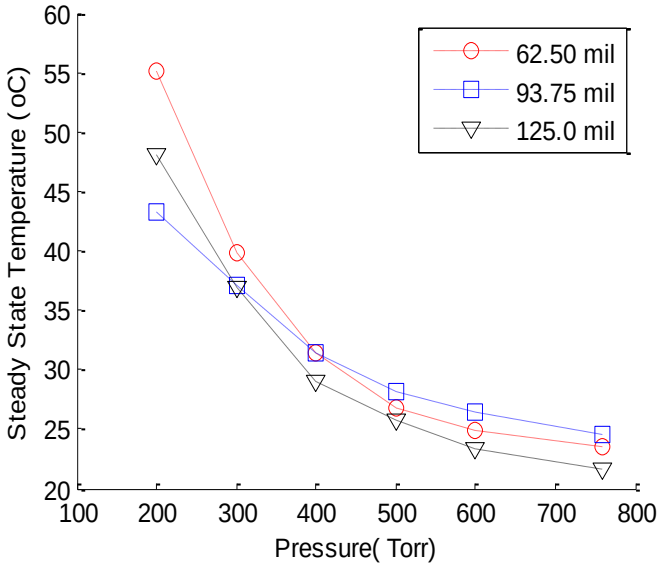

Figure 8-11. Steady state temperature for three different dielectric thicknesses as a function of pressure.

In any case, however, the temperature is not found to increase more than a few 10s of degrees, suggesting that the change in the loss tangent and hence power lost in the dielectric may not be significant to effect actuator performance for the range of design parameters tested.

The data presented in Figures 8-10 and 8-11 was obtained from actuators which were run at different voltages. For a more one-on-one comparison to get a better idea of the trends, two thicknesses of Garolite (93.75 mil, 125.0 mil) were tested at the same voltage (12 kVpp, 14 kHz). Figures 8-12 shows the results.

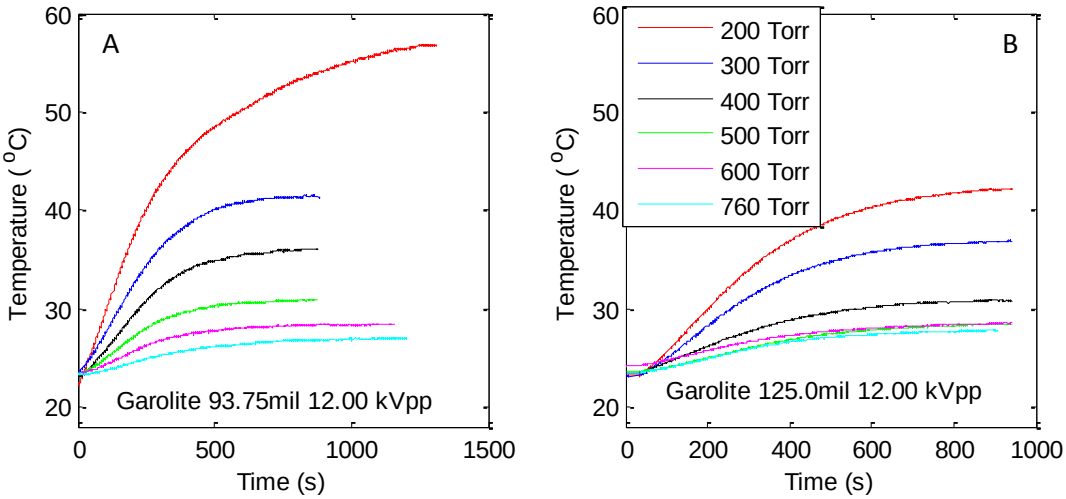

Figure 8-12. Dielectric temperature as a function of time for Garolite at identical operating voltage. A) 93.75 mil at 12 kVpp. B) 125.0 mil at 12.00 kVpp.

The time-temperature plots are as expected. The temperatures reach a steady state values that are higher for the thinner of the two dielectrics. The non-linear increase in temperature with decreasing pressures is better evident in Figure 8-13, which resembles the power consumption plots of Figure 7-11.

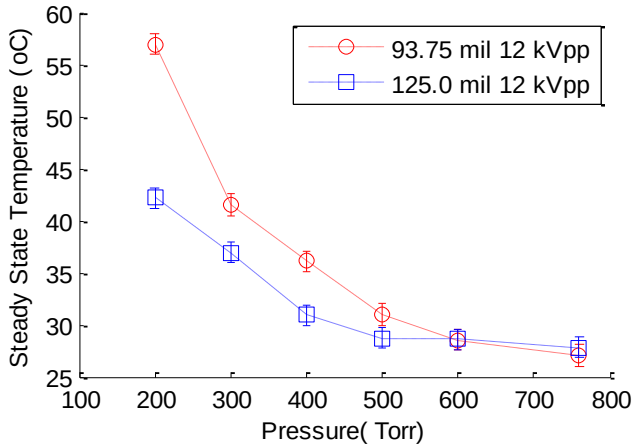

Figure 8-13. Steady sate temperature for three different thicknesses as a function of pressure

These results suggest that dielectric heating is not significant enough to affect dielectric performance at the conditions (operating voltage, ambient pressure) tested. However this may not be true for all actuators. Dielectric with lower heat capacity

operated at high enough voltages may reach temperatures where the change in the loss tangent might become significant. On the other hand, the heating of the dielectric over time enhances its performance as demonstrated by (Erfani, Zare-Behtash, & Kontis, 2012). In light of these finds, actuators designed for prolonged operation should take dielectric heating into account, since the performance of the actuator could drift significantly over time depending on the severity of the heating and change in loss tangent of the dielectric.

CHAPTER 9
EFFECTS OF MAGNETIC FIELDS ON DBD ACTUATORS

One of the many losses in DBD actuators is due to low ionization efficiency. This essentially has to do with the number of neutrals an electron ionizes before it drifts out of the high electric field region either due to thermal motion or on account of collision with energetic ions/neutrals. Accordingly, the ionization efficiency can be increased if electrons could be trapped in the region of high electric field, possibly using magnetic confinement. This concept is similarly used in Hall effect thrusters, where a virtual cathode is created by a ring of circulating electrons that are trapped in their path by radial magnetic field (Goebel & Katz, 2008). The virtual cathode mitigated the short life times of gridded ion thrusters on account of erosion by high energy electrons.

9.1 Plasma Actuators with Externally Applied Magnetic Field

A similar magnetic confinement can be implemented for DBD actuators in theory. Since the $\vec{E} \times \vec{B}$ drift is always perpendicular to both the E and the B fields, this necessitates a radial geometry of flow. One such possible arrangement is shown in Figure 9-1.

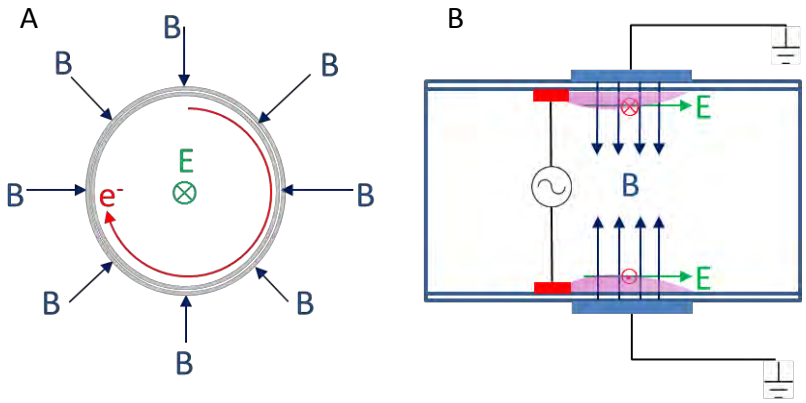

Figure 9-1. Schematic of DBD actuator enhancement using radial magnetic field. A) Looking into the tube. B) Side view.

To assess the impact of externally imposed magnetic field, a test actuator was constructed as shown in Figure 9-2. The actuator is made of 1 inch OD x 1/16 inch thick acrylic tube, with 5mm powered and ground electrodes, separated laterally by a 5mm gap 5mm. The magnetic ring is made of small neodymium (Grade N52, surface field ~6000 Gauss) magnets 3 mm x 3mm x 3mm in size, procured from K&J Magnetics. The magnets are held together in a radial configuration on the outer surface of the tube with hot glue. Two arrangements were tried, with the north poles of the magnets pointing radially inside in one case, and going out in another. The actuator was mounted on the μNTS and connected with AWG 36 copper lead to reduce external influence on force measurement. Thrust and power data was recorded for the two cases.

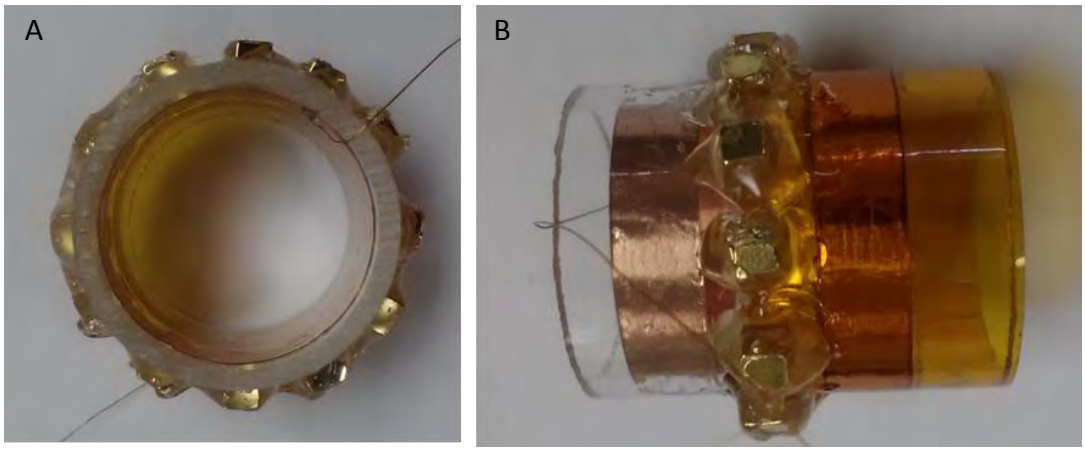

Figure 9-2. Tubular plasma actuator with radial magnetic field arrangement. A) Looking into the tube. B) Side view.

9.2 Effect of Magnetic Field on Plasma Actuator Performance

Figure 9-3 shows the plasma discharge pattern with and without magnets. From visual evidence, the presence of magnets seems to alter the discharge characteristics. In the absence of magnets, the plasma shows local hotspots, which are regions of relatively stronger plasma. When the magnets are introduced, the plasma seems to become more diffuse and uniform across the circumference.

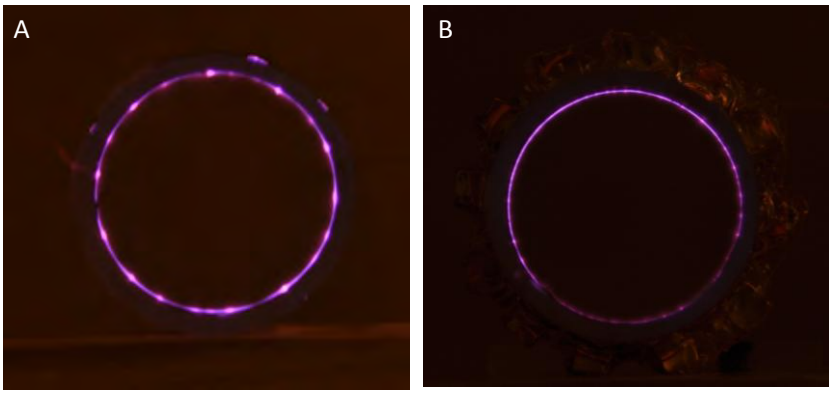

Figure 9-3. Effect of magnetic field on actuator discharge at 18 kVpp 14 kHz. A) Without magnets. B) With magnets.

Figure 9-4 shows the thrust for the cases of no magnetic field, North going in, and South going in. It is seen that the change in force falls within the error margin of ±10% for the μNTS. The power consumption for the three cases was found to be 7.51, 8.4, and 7.76 W respectively, which is within error margin of each other. This indicates that the effect of magnetic field, if any, is too small to be resolved with the current setup.

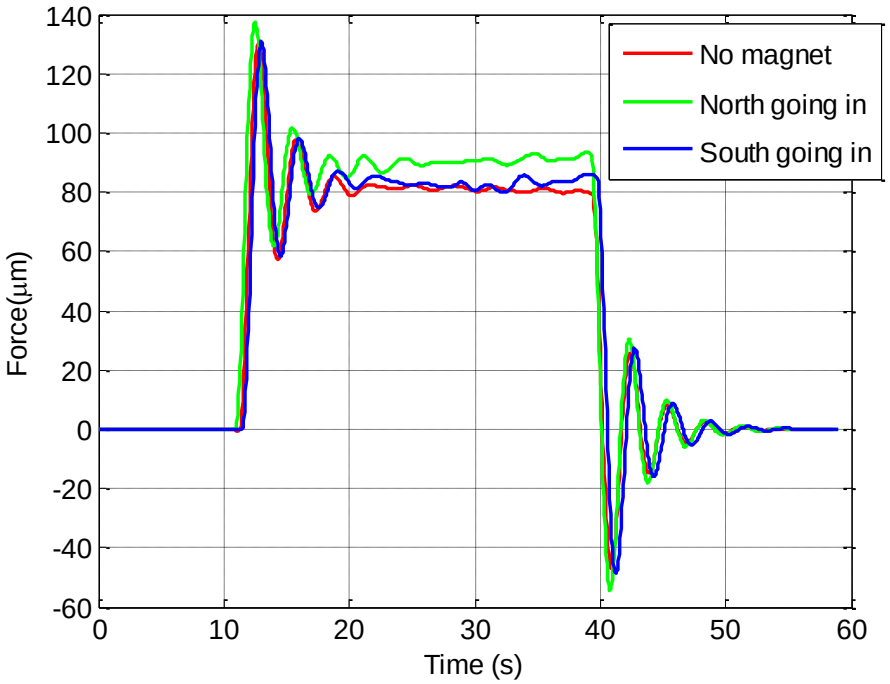

Figure 9-4. Effect of radial magnetic field on actuator thrust at 18 kVpp 14 kHz

Figure 9-5 shows an alternate magnet arrangement that was tried. The magnetic ring was made of 6 circular arc magnets with alternating polarity. As in the previous case, the visible plasma characteristics was noticeably different in the two cases, being more diffuse and uniform in the case with magnets. This might be due to the fact that the material of the magnet acts as a floating potential electrode in the vicinity of a strong magnetic field, and acts as a ground, this effectively bridging the gap between the electrodes, resulting in a more uniform plasma region. However, no noticeable change in thrust was observed (Figure 9-6).

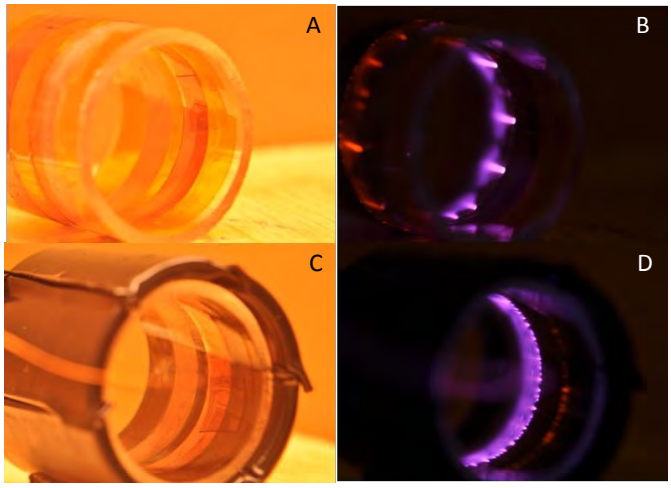

Figure 9-5. Visual Plasma characteristic. A,B) without magnets. C,D) With magnets.

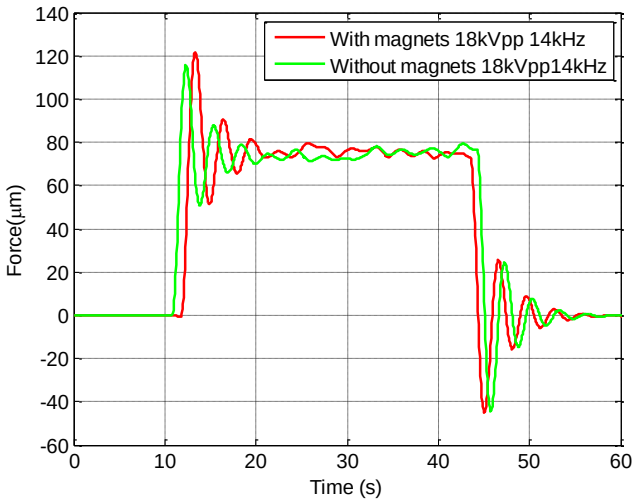

Figure 9-6. Effect of arrangement of Figure 9-5 on thrust at 18 kVpp 14 kHz

Figure 9-7 shows the current profiles for the two cases. It is seen that the discharge profiles are significantly different. For the case without magnets, the discharge sparks are fewer but stronger, but for the case with magnets, the spikes are more in number but weaker. This corroborates well with the visual evidence. The power dissipation, however, was found to be the same in either case (~7.2 W) within expected error bounds, suggesting the presence of magnets is altering the energy/potential distribution in the plasma formation region.

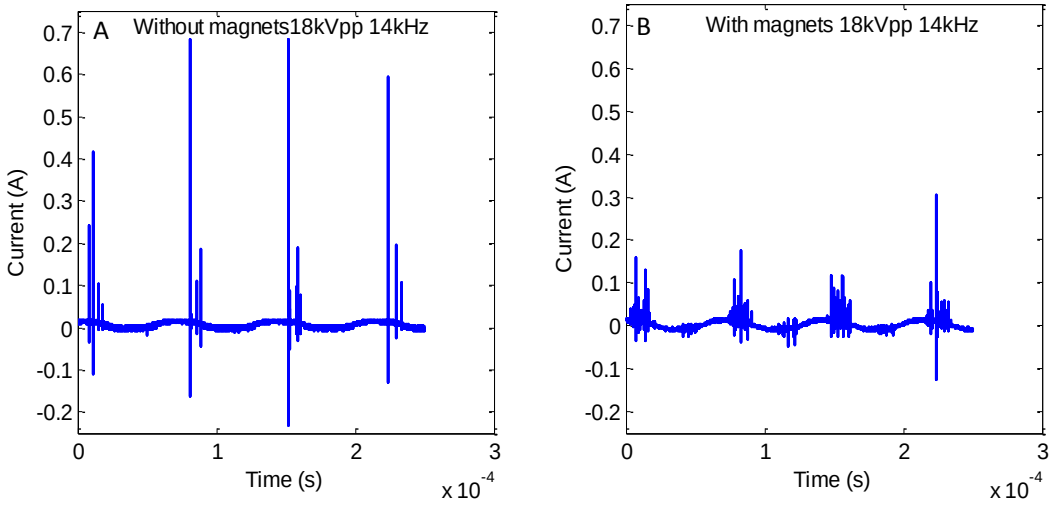

Figure 9-7. Current profiles for arrangement of Figure 9-5. A) Without magnets. B) With magnets.

Based on the above results, it is seen that the presence of magnets alter the visible, and electrical characteristics noticeably. This, however, could be merely due to presence of the magnets which act as a floating metal reservoir of electrons. To test this hypothesis, the magnets were demagnetized by heating them over an alcohol flame. The arrangement was then reconstructed and the setup run at identical conditions as before demagnetization. The discharge pattern was found to be identical to the one before demagnetization. This suggests the visible, and hence the discharge

characteristics observed with magnets were likely due to the presence of a floating potential surface than the magnetic field itself.

To investigate why the magnetic field had no impact on the functioning of the actuator, the magnetic field distribution for the arrangement was numerically computed using the open-source Finite Element Method Magnetics software. The resulting B-field distribution for the two arrangements (for quarter of the circle) is shown in Figure 9-8. This suggests the magnetic field at the distance from the surface where the plasma originates is only of the order of a few 100 Guass. This field strength may not be sufficient to cause any electron trapping to increase their residence times and ionization efficiency. The primary challenge in testing the effect of magnetic fields has been isolating the effect of the magnets as a floating electrode. Increasing the separation of the magnets simply results in further drop in the magnetic field strength, presenting a dilemma.

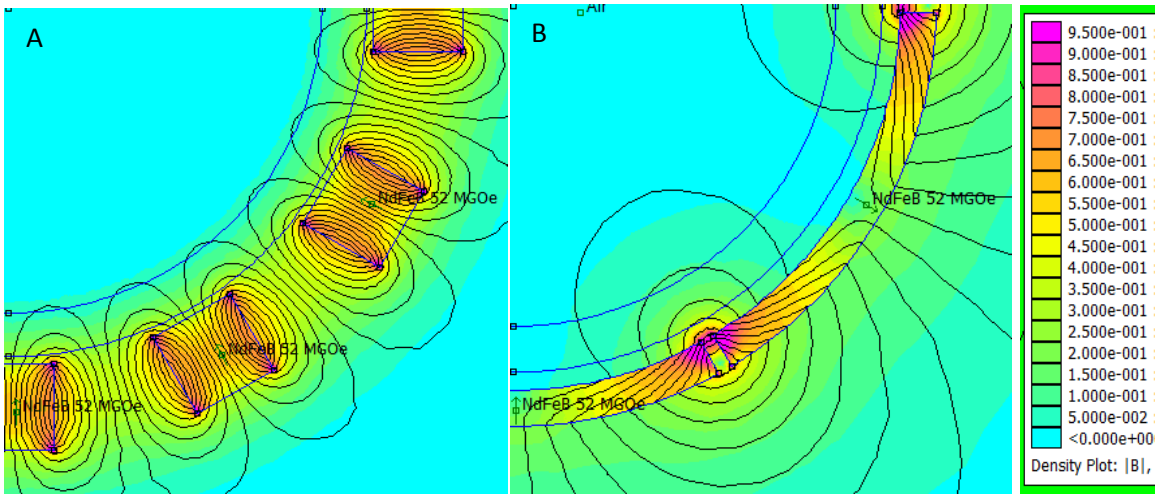

Figure 9-8. Magnetic field distribution for the two arrangements. A) For arrangement of Figure 9-2. B) For arrangement of Figure 9-5.

Based on the results of the current data set, magnetic field does not seem to help force production at the field strengths achieved with current configurations. The change

if any, is below the thrust stand resolution to be noticeable. Further, it remains to be seen if the effect, if any, is due to the magnetic field or just due to the stronger plasma as evident from visual observations.

CHAPTER 10
EXPLORATION OF VOLUMETRIC DBD ACTUATORS

10.1 Limitation of Surface DBD Actuators

Traditional configuration of SDBD actuators implies the plasma is generated right at the edge of the powered electrode next to the wall. This translates to most of the momentum being transferred to the fluid in a region very close to the wall. This is evident from the velocity profiles for such actuators, which suggests peak velocity occurring within a few millimeters from the wall. With higher induced velocities, the velocity gradient close to the wall become significant, resulting in increased wall shear and hence momentum loss. Furthermore, interaction with the stationary air results in free-shear which results in further momentum dissipation. Moving the region of plasma production and hence momentum transfer away from the wall could possibly alleviate these losses to an extent, improving the induced thrust.

10.2 Volumetric DBD Actuators

Moving the plasma production region away from the air entails separating the powered electrode from the wall, hence leaving it suspended at a distance. Such a design would involve a channel with a powered wire electrode suspended at the centerline and ground electrodes on the outer surfaces of the channel walls. One such design, shown in Figure 10-1, has been demonstrated to produce appreciable velocities (Campbell & Roy, 2014). This design was shown to have a 700% improvement in electrical to kinetic energy conversion efficiency with exit velocities reaching over 5 m/s spanning across the channel width of 5mm. These results suggest that volumetric DBD actuators might have certain inherent advantages over SDBD actuators for thrust production.

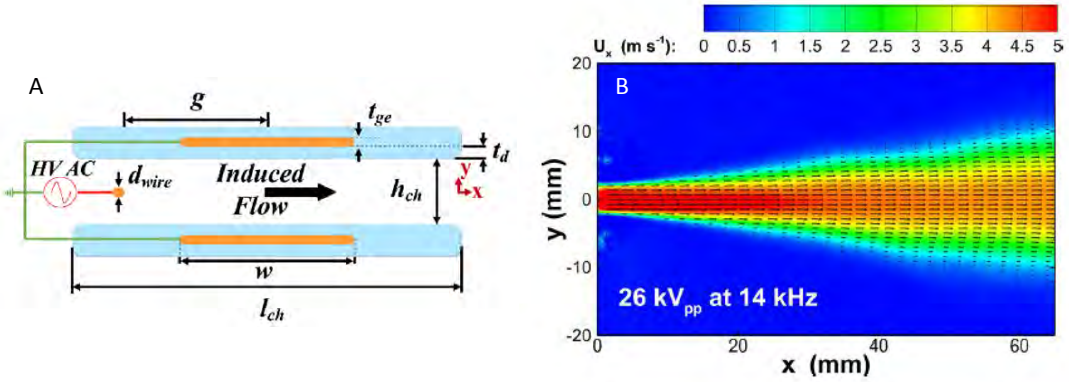

Figure 10-1. Volumetric DBD actuator concept and demonstration. A) Design schematic. B) Flowfield results at 26 kVpp 14 kHz (Campbell & Roy, 2014).

10.3 Volumetric DBD Nozzle Thrusters

To explore the design space further, two nozzle shaped volumetric DBD channels were built and tested. Figure 10-2 provides details of these two designs. The two channels had differing inlet and exit areas as well as dielectric thickness. The placement of the powered electrode also meant different powered-to-ground electrode separation. Design 1 had an inlet width of 20mm and exit width of 5mm with 2.5mm thick acrylic dielectric, whereas design 2 has inlet and outlet width of 6mm and 3mm respectively, with 1.5mm thick acrylic dielectric. In both cases, the lateral (in the direction of flow) electrode separation was 5mm, while the absolute electrode separation (shortest connecting path) was 9mm and 6.5mm respectively. The powered electrode was a 0.005" diameter SS wire, and 20mm wide copper tapes acted as ground electrodes

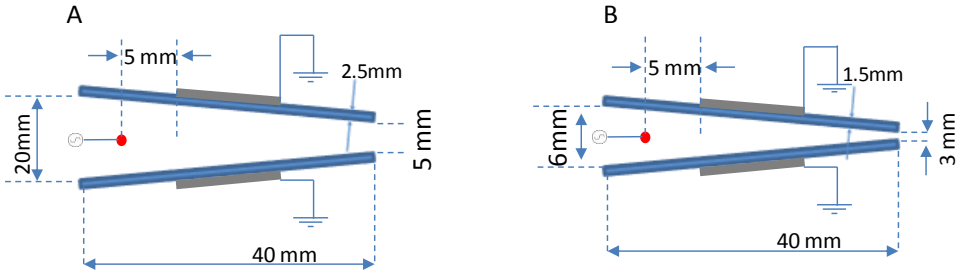

Figure 10-2. Details of the volumetric DBD nozzle channels. A) Design1. B) Design 2.

The channels were operated at a frequency of 5 kHz and voltages ranging from 16-26 kVpp. The velocity flowfield downstream of the nozzle exit was captured using a PIV setup which consisted of Nd:YAG 532 nm pulse laser and 800x600 pixel Phantom 7.3 high speed imaging system. Ondina oil was used to generate a seeding particle mist using an atomizer. The data was captured and processed using LaVision DaVis 7.2 PIV software. Averaging over 100 image pairs provided a good compromise between flow field convergence and postprocessing time. The results from the PIV runs are shown in Figure 10-3.for design 1 and Figure 10-4 for design 2.

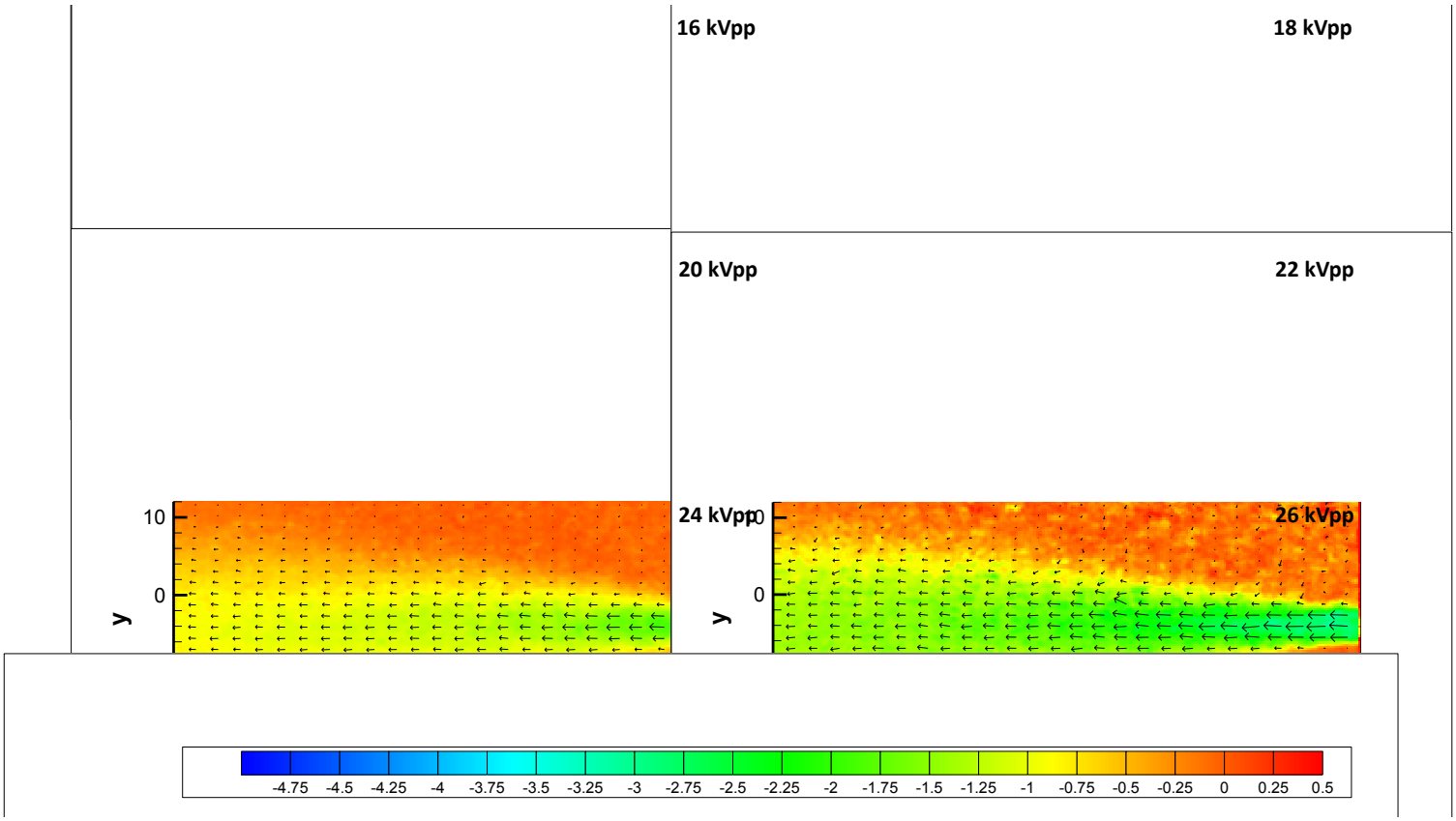

Figure 10-3. Flow field results from nozzle design 1 at 16-26 kVpp, 5 kHz.

The two designs are seen to generate exit plane velocities of upto 3 m/s and 5 m/s respectively. The better performance of design 2 should not be surprising on account of smaller exit area, thinner dielectric, and smaller electrode separation.

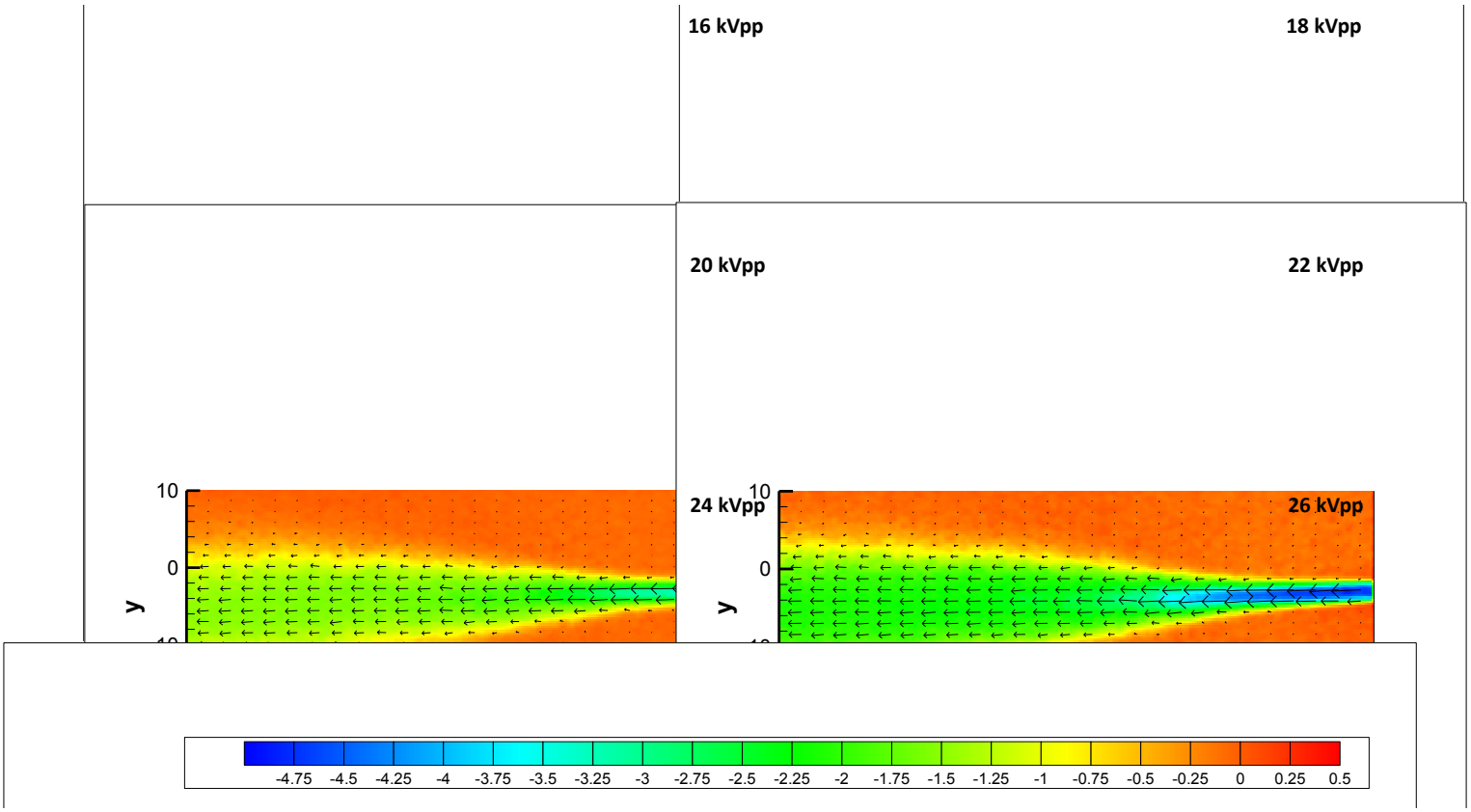

Figure 10-4. Flow field results from nozzle design 2 at 16-26 kVpp, 5 kHz.

Velocity profiles at the exit plane of the two nozzle designs at varying voltages are shown in Figure 10-5. Results suggest that design 1 has more of a plug flow profile compared to design 2, which has a more parabolic profile reminiscent of fully developed Hagen-Poiseuille flows. Since the downstream lengths of the two nozzles are the same, this indicates that the momentum transfer distribution for the two designs is dissimilar, likely on account of different electrode separation. For nozzle design 2, the velocity profile seems to saturate as seen from the velocity profiles for the two highest voltages, which seem to overlap. The peak velocities for the two designs as a function of voltage are plotted in Figure 10-6. It is seen that design 2 generates significantly higher velocities than design 1, an increase of almost 100% in most cases. Again, this is to be

expected given the difference in design parameters (electrode separation and dielectric thickness).

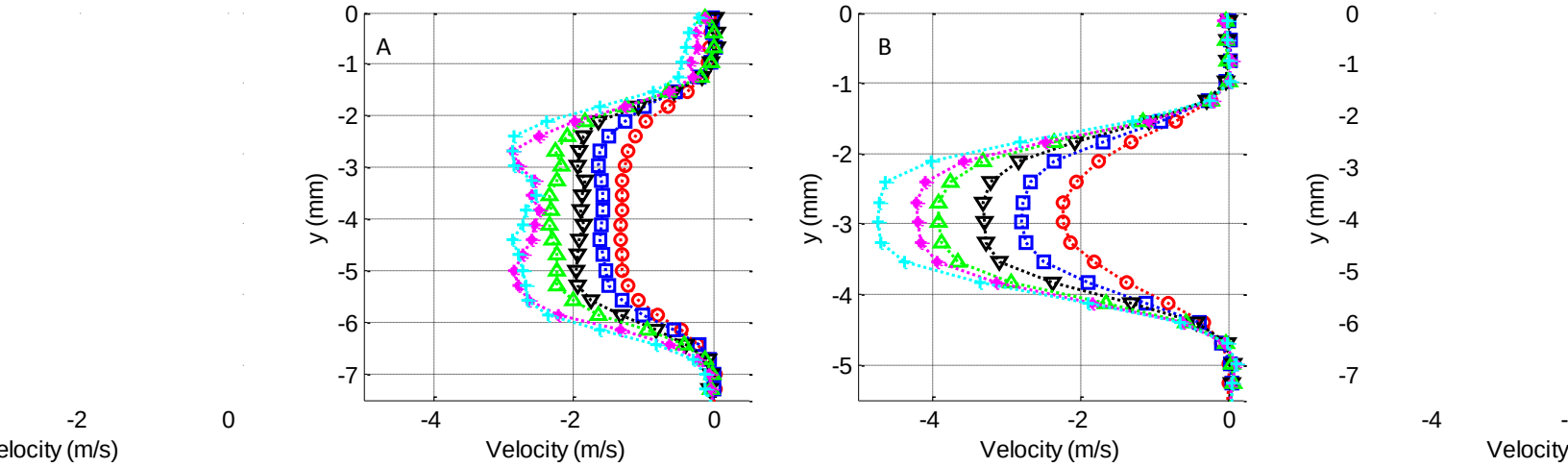

Figure 10-5. Velocity profiles for the two nozzle designs at 16-26 kVpp, 5 kHz. A) Design 1. B) Design 2.

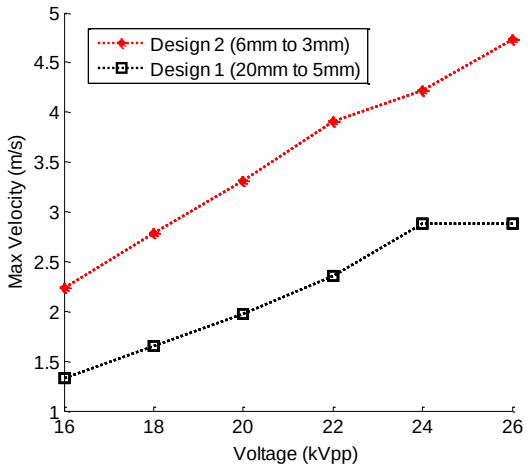

Figure 10-6. Peak velocities for the two nozzle designs at 16-26 kVpp, 5 kHz

A true comparison of the two designs vis-a-vis performance for a thrust producing device should take into the account the power consumed to produce a given amount of thrust. To quantify this metric, the thrust from the two nozzles was measured using the Ohaus precision balance, and the power recorded using the setup mentioned in Chapter 7. Figure 10-7 shows the thrust, power and effectiveness (thrust per power) for the two designs.

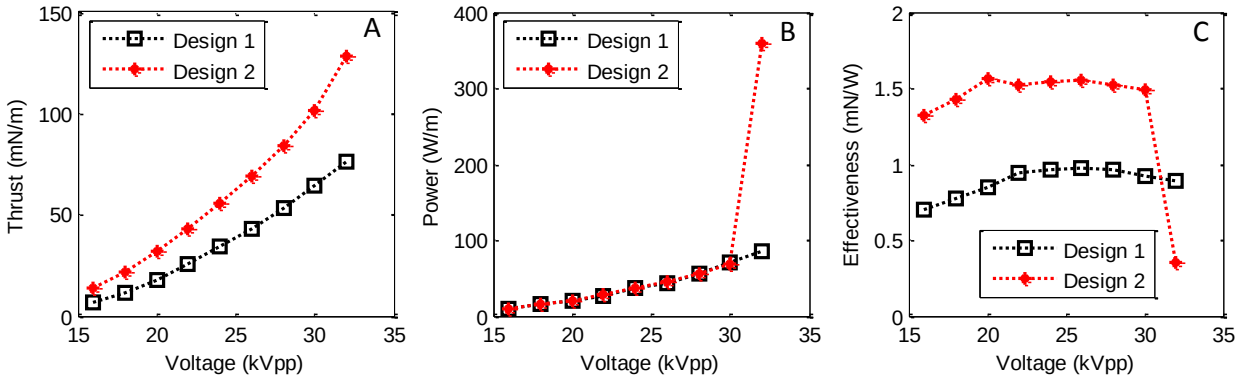

Figure 10-7. Thrust, power and effectiveness for the two designs at 16-32 kVpp, 5 kHz. A) Thrust. B) Power. C) Effectiveness.

It is seen that design 2 produces a higher thrust, ranging from 100% to 68% higher than design 1 depending on voltage. More importantly, however, the power consumption remains quite identical throughout the voltage range, except at 32 kVpp, at which design 2 goes into streamer mode. Consequently, the effectiveness is significantly higher for design 2 (except at 32 kVpp), with improvement ranging from 87% at 16 kVpp to 67% at 28 kVpp. These numbers are much higher (over 200%) than those reported in literature for conventional SDBD actuators, as reproduced in figure 10-8 (Durscher R. J., 2012).

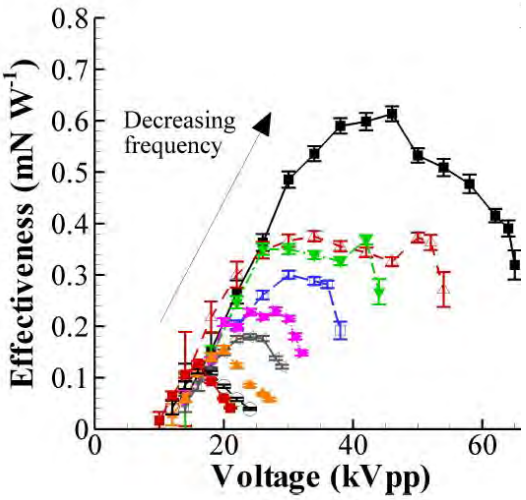

Figure 10-8. Effectiveness of SDBD actuators as reported in literature (Durscher R. J., 2012)

Conventional SDBD actuators are known to exhibit a saturation phenomenon, whereby the force increases with voltage upto a certain value, after which it drops with increasing voltage. The voltage at which this occurs is found to be a strong function of frequency and dielectric constant. The onset of saturation is accompanied by the formation of strong plasma streamers. Figure 10-9 demonstrates the nature of DBD plasma in an actuator under normal operation and when it reaches saturation (streamer formation). Streamers essentially unfavorably change the energy deposited by the plasma to the ambient fluid. The pre-saturation uniform glow ensures an almost even deposition of energy and hence momentum into the fluid. The streamers, however, drastically alter this distribution, instead creating a few localized hot-spots of energy and momentum deposition. This change in momentum distribution has been shown to adversely affect the induced thrust (Durscher, Stanfield, & Roy, 2012).

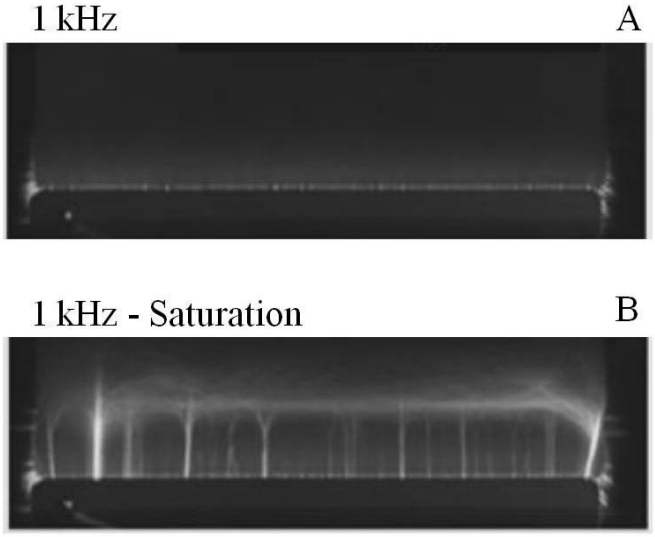

Figure 10-9. Change in plasma characteristics at the onset of saturation. A) No saturation. B) Saturation (Durscher R. J., 2012).

The mechanism of streamer onset and formation is understood to be thermal ionization overheating instability, which is set up by a feedback loop established

between plasma heating and increasing ionization. (Durscher R. J., 2012). The role of dielectric temperature was confirmed by externally induced heating of the dielectric, which resulted in early onset of saturation (Durscher R. J., 2012). Considering the similarities between the SDBD and VDBD actuators, such a glow-to-filamentary transition should be anticipated at a given threshold voltage, possibly accompanied by thrust saturation. Figure 10-10 shows images of the plasma around the powered electrode at increasing voltages for design 1. It can be seen that from 16 up to 28 kVpp, the flow is fairly uniform with multitudes of microdischarges characteristic of DBD glow plasma. Between 30 and 32 kVpp however, the plasma transitions to strong filamentary in nature, with a few strong streamers originating at the powered electrode all the way till the dielectric surface. The discharge current at this point increases significantly from 10s of mAs to almost 1 A (Figure 10-10) resulting in a sharp increase in power consumption from 7.87 W at 30 kVpp (glow mode) to 41.24 W at 32 kVpp (streamer mode). These streamers are also found to be dynamic, appearing and disappearing at different places over time.

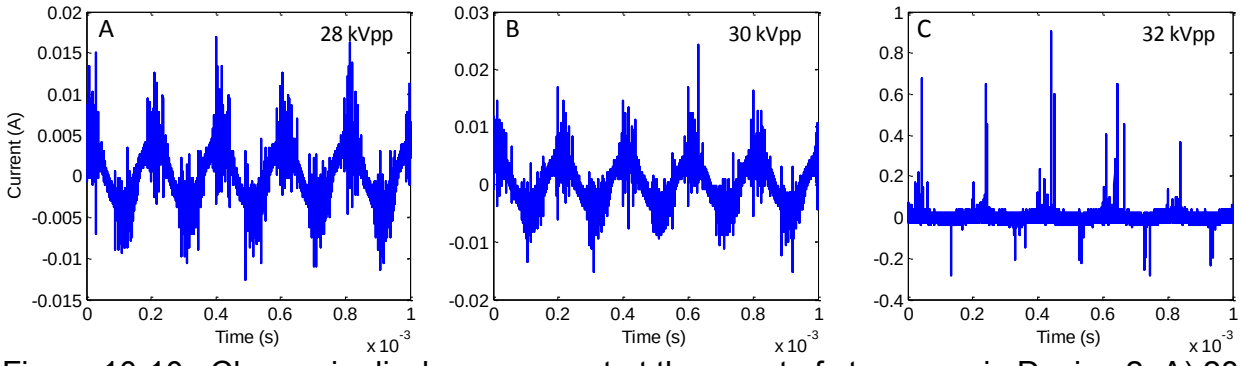

Figure 10-10. Change in discharge current at the onset of streamers in Design 2. A) 28 kVpp. B) 30 kVpp. C) 32 kVpp.

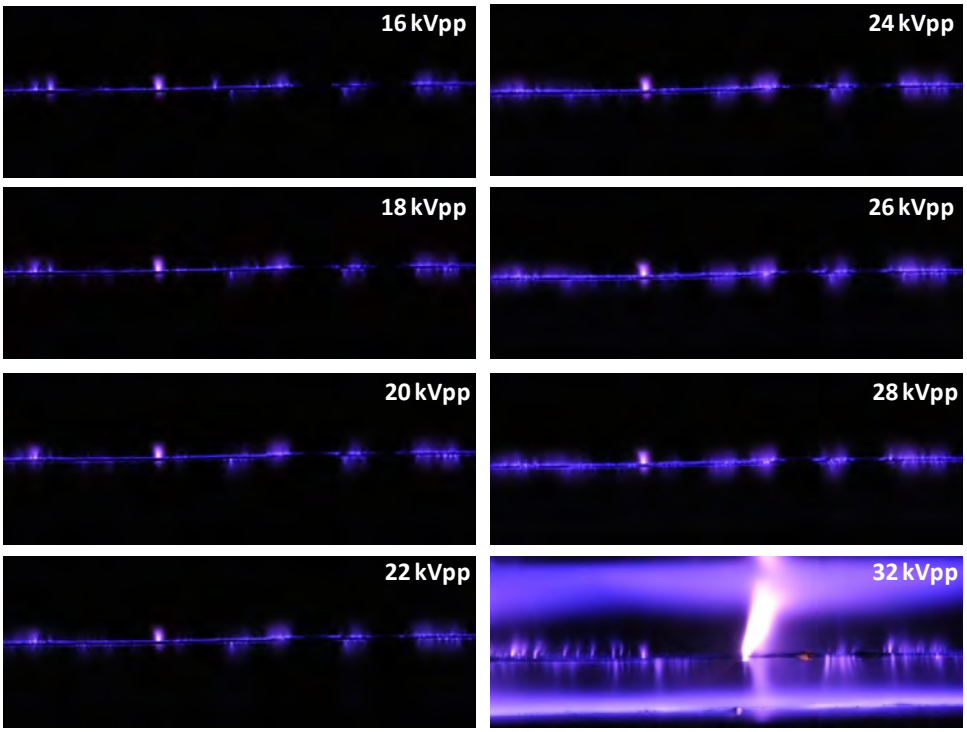

Figure 10-11. Visual characteristics of VDBD plasma at various voltages showing glow and filamentary modes for design 2.

The effectiveness drops sharply for design 2 at the onset of streamers, dropping nearly 75 % from 1.48 mN/W at 30 kVpp to 0.35 mN/W at 32 kpp. The induced thrust, however, shows an absence of any saturation effect, as evident from the thrust data in Figure 10-7. This suggests that volumetric DBD actuators may respond differently to ionization heating instabilities than SDBD actuators as far as momentum distribution is concerned. The current set of data is not sufficient to confidently make a general claim in this regard or propose a hypothesis.

Regardless of streamer formation and absence of saturation in the design tested, it is clear that volumetric DBD actuators offer significant increase in thrust and effectiveness over their SDBD counterparts, warranting exploration of VDBD based thrusters for high altitudes.

CHAPTER 11
EXPLORATION OF NON DBD DESIGNS

The performance of DBD actuators depends on the efficacy of momentum transfer from charged particles to neutrals through collisions. At reduced pressures, the reduction in the overall number density translates into a reduction in actuator force. The relative proportions of charged and neutral species also undergo change as the reduced electric field (E/n) increases as pressure decreases, leading to a higher degree of ionization. Once the degree of ionization crosses a certain threshold, the charged particles keep oscillating between the two halves of the voltage cycle without a net transfer of momentum to the fluid in one direction. Given this, DBD actuators may have an inherent limitation when it comes to low pressure performance. This opens up the possibility of using electrostatic and electromagnetic acceleration instead of DBD actuators for thrust production.

11.1 Electrostatic Channel Thruster

Electrostatic acceleration of charged particles for thrust generation requires a DC voltage. Accordingly, a switch was made from AC-driven surface DBD plasma to DC-driven volume glow plasma to assess the feasibility of a DC glow plasma channel thruster. A generic design of such a device consists of a 2D channel with 2 pairs of electrodes embedded in the channel walls. The electrodes are electrically biased so as to create a laterally (axially) directed electric field. In the regions of high E-field close to the electrode edges, ions are produced via Townsend ionization, and are accelerated towards the cathode located near the channel exit. The expulsion of heavy ions from the thruster and the electrostatic space-charge effects result in a net thrust on the device.

To test the concept and explore the design space, several design iterations were carried out. In all iterations, the thruster length (electrode length) was 50mm.

11.1.1 Design Iteration I

The first iteration of the design involved a 2D channel made of two glass plates as channel walls (Figure 11-1). The total length along the direction of anticipated flow was 25mm and the total channel width was 60mm. The channel height was chosen to be 2mm, corresponding to free-molecular flow regime Knudsen number of ~10 at an ambient pressure of 3 Pa. The operating pressure point was approximated based on Paschen minimum for air, which occurs at 327 Volts at a *pd* of 0.57 Torr-cm. For a given electrode distance, the operating pressure was estimated subject to this condition. Deviation from Paschen's Law was noticed, as anticipated, since the electrodes in the current geometry are not really parallel plates facing each other. To isolate thrust force from stray electrostatic force, the device was run with reversed polarity as well as physically flipping the thruster to reverse the thrust direction, if any force was noticed in the initial runs.

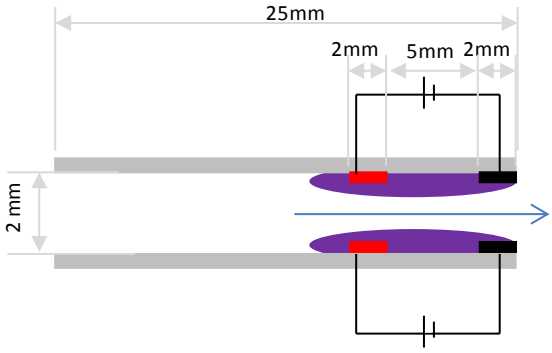

Figure 11-1. Electrostatic channel thruster design iteration I

The μNTS was placed inside a bell jar vacuum chamber (18" ID x 72" H), which was mounted on top of a heavy optical bench (Melles Griot) to isolate seismic

vibrations, which have been demonstrated to deteriorate the SNR for force measurements. The setup is shown in Figure 11-2.

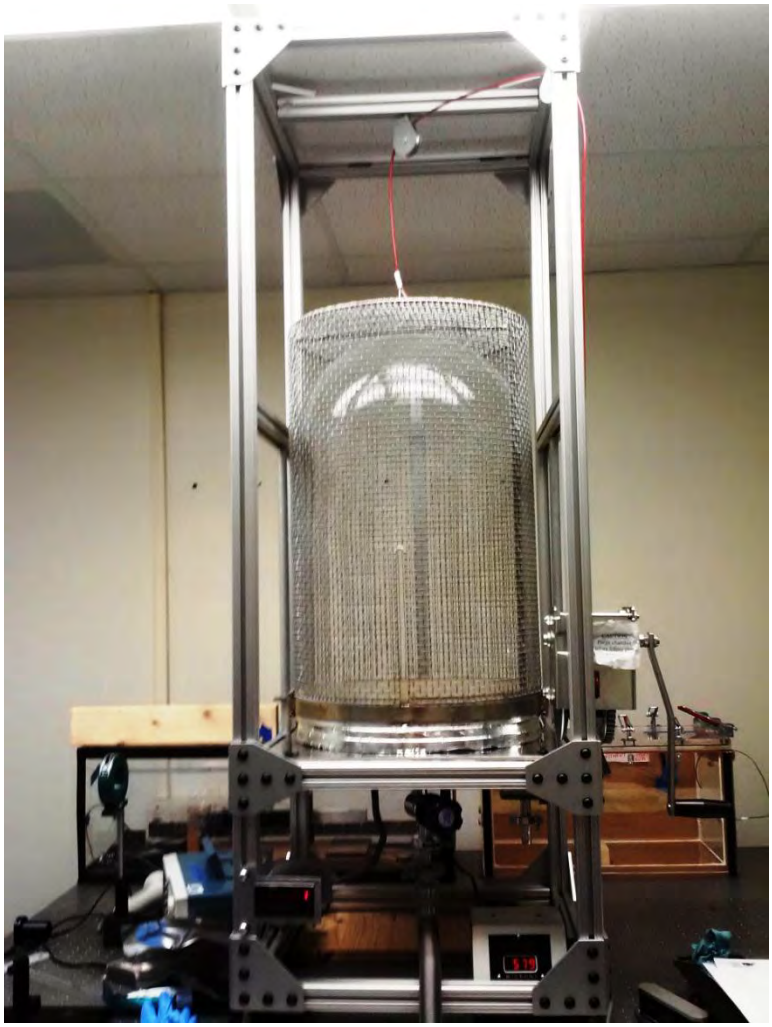

Figure 11-2. Bell-jar setup used for testing design iteration 1

Figure 11-3 shows the force plot for design iteration I at operating conditions of 1.5 Torr at 400 Volts. The device was fired 3 times for repeatability and statistical analysis. The thrust stand seemed to register a force of around 0.3 μN at the aforementioned operating conditions. The device drew a current of around 13 mA, leading to a power dissipation of 5.2 Watts. The device was then run with reversed polarity. Although the magnitude of the force in this case was comparable, the anticipated reversal in direction of thrust was not seen. The thruster was then physically

flipped to reverse the thrust vector, and fired again with positive as well as negative bias. The results in Figure 11-4 show the same trend, where the magnitude of the force is consistent, but not the direction. This led to the possibility of stray electrostatic forces interfering with the force measurement since the bell jar walls were unavoidably close to the thruster due to the size constraints. Charge deposition on the glass surface of the bell jar could easily cause electrostatic interaction with the device sitting on the thrust stand only a few centimeters away

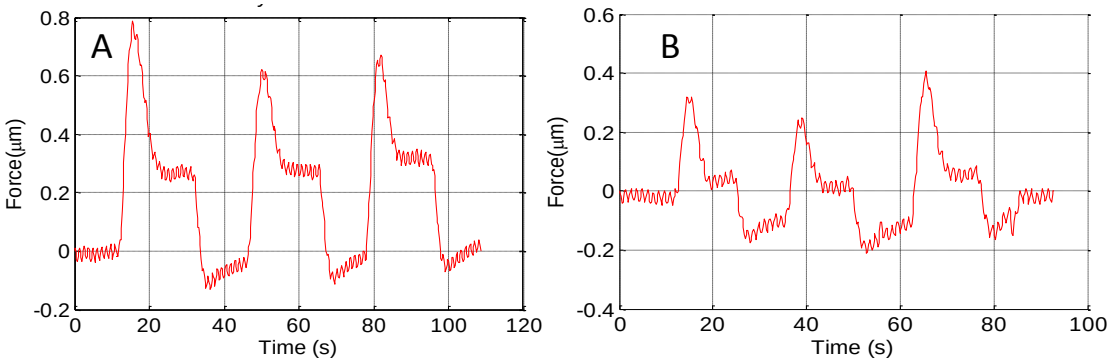

Figure 11-3. Force data for design iteration I, 320 V at 1.5 Torr. A) Positive bias. B) Negative bias.

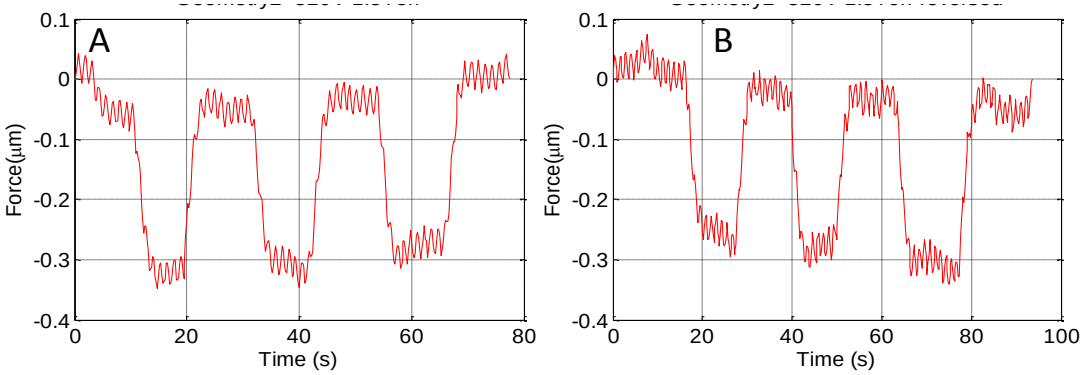

Figure 11-4. Force data for design iteration I, 320 V at 1.5 Torr with thruster direction reversed. A) Positive bias. B) Negative bias.

11.1.2 Design Iteration II

To eliminate this issue, the whole setup was moved into the Thermal Vacuum Test Facility (TVTF), which is a horizontal cylindrical vacuum chamber (1m dia x 1.5m

length). The spacious interior allowed position of the thruster such that electrostatic interferences could be eliminated. This setup is shown in Figure 11-5.

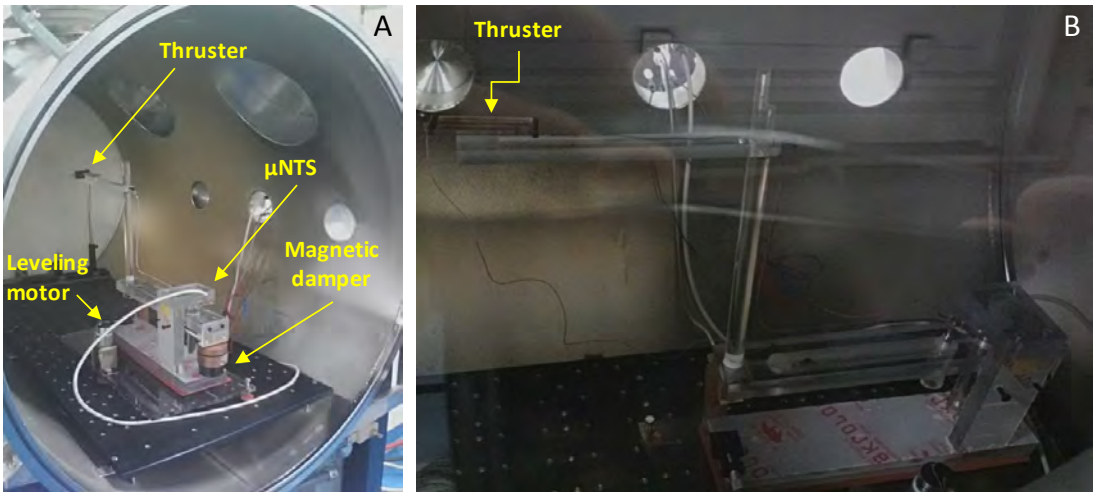

Figure 11-5. Details of the Thermal Vacuum Test Facility and the nanoNewton. A) Looking into the chamber. B) View through the observation window.

The thrust stand was modified to mount the thruster as away from any structural components as possible. The thruster design itself was slightly modified: the electrodes were made wider to increase thermal dissipation which was leading to electrode deformation/peeling off, and the electrode pairs were moved to the center of the channel to shield and even out electrostatic interference from external surfaces. Geometrical details of this iteration are presented in Figure 11-6.

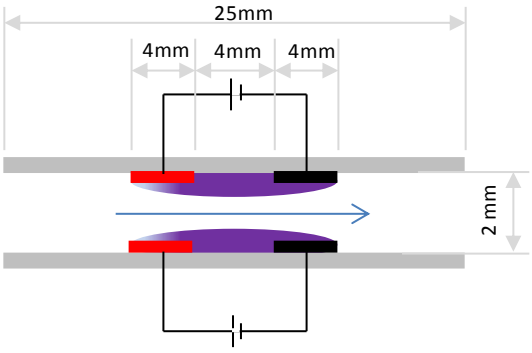

Figure 11-6. Electrostatic channel thruster design iteration II details

Unlike the bell-jar, the TVTF is not mounted on an optical bench to isolate seismic vibrations, resulting in poor signal-to-noise ratio. Of particular concern was thrust-stand drift which, unlike the bell-jar setup, was found to be highly unpredictable. To circumvent this issue, force measurements could be taken only over short intervals of a few seconds to discern clear trends. The following protocol was followed: the force was monitored with the thruster off for 20 seconds, then the thruster was fired for 20 seconds, after which data was recorded for another 20 seconds to act as buffer. To ensure independent trials, the data was recorded independently 5 times. The device was found to ignite uniformly at around 320 Volts at 1.5 Torr. Figure 11-7 shows that no clear force was noticeable in the 4 trials that were recorded without excessive noise. The signal with excessive noise (green) is representative of the drift and noise issues encountered while trying to measure sub-micronewton level force. The device was seen to draw a current of about 13 mA, resulting in a power dissipation of 4.16 Watts. No corresponding thrust, however, was observed above the noise levels.

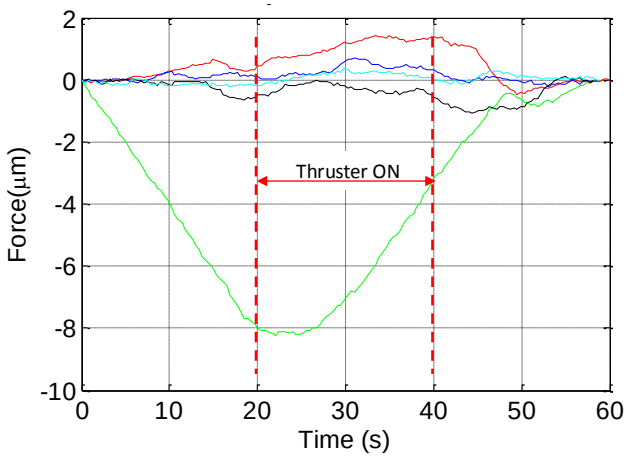

Figure 11-7. Force data for design iteration II, 320 V at 1.5 Torr

11.1.3 Design Iteration III

Based on the results from design iterations I and II, a change in electrode configuration was implemented. Numerical simulation conducted at APRG using the in-house finite element code MIG predicted non-optimal ion trajectories for previous iterations: the sharp wall-directed electric field at the cathode would result in the ions being accelerated more towards the channel wall than along it. To rectify this, the cathode was changed from a planar wall-electrode to a wire electrode that was suspended at the channel exit. The resulting electric field would be much well-contoured for ion acceleration along the channel walls than towards them. Figure 11-8 below provides details of design iteration III.

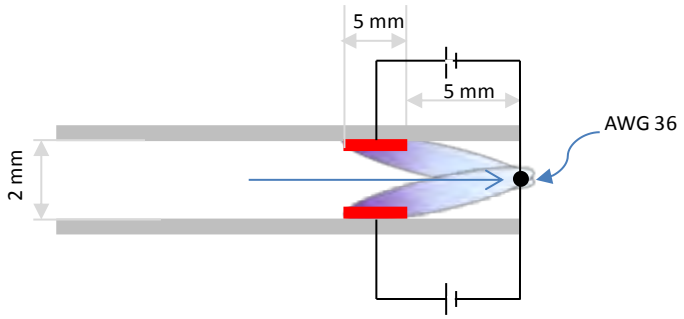

Figure 11-8. Electrostatic channel thruster design iteration III details

Force measurement from this design (Figure 11-9) is reminiscent of that from Design Iteration II. There is no clear, repeatable force trend that can be identified during the duration of thruster operation. As in previous results, the issue of thrust stand drift is made amply clear by the trial run depicted in black. The device drew a current comparable to previous designs, but was run at a higher voltage (-540 Volts) due to the slightly increased electrode distance. The corresponding power drawn was about ~7 Watts with no discernible force.

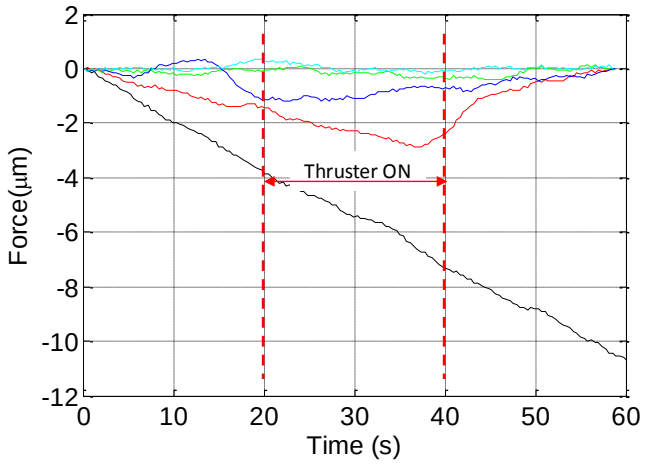

Figure 11-9. Force data for design iteration III, 540 V at 1.5 Torr

11.2 Lorentz Channel Thruster

Results from the three design iterations of electrostatic channel thruster suggest that electrostatic force alone may not be sufficient to provide thrust. The Lorentz force $\left(\vec{E}+\vec{v}\times\vec{B}\right)$ can offer significant improvement in thrust depending on the contribution from the $\vec{v}\times\vec{B}$ term. To explore the possibility of using magnetic field for thrust production in a channel, a Lorentz channel was built with crossing E and B fields. The channel consisted of a rectangular cross section 0.75” x 0.25”. Two 0.25” high brass plates were used as electrodes and were fixed to the side walls such that the electric field was in the horizontal direction. Two 0.5”x1”x1/8” neodymium magnets (N52 grade, surface B-field = 2451 Gauss) were placed on the top and bottom walls of the channel to apply a vertical magnetic field.

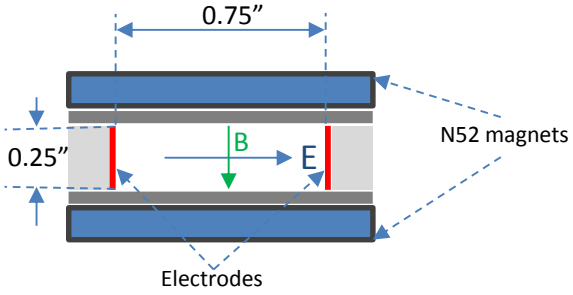

Figure 11-10. Lorentz channel thruster design details

The magnetic field distribution in the plasma region is found using numerical simulation using the FEMM open source software. Figures 11-11 shows the magnetic field strength in the center of the channel for 1/8" magnets. Simulations were performed with differing widths of magnets to obtain an estimate of the magnetic field that could be obtains at the channel centerline. As can be seen from Figure 11-12, a field of almost 0.3 Tesla (3000 gauss) can be imposed along the centerline using a ¼" thick N52 magnet.

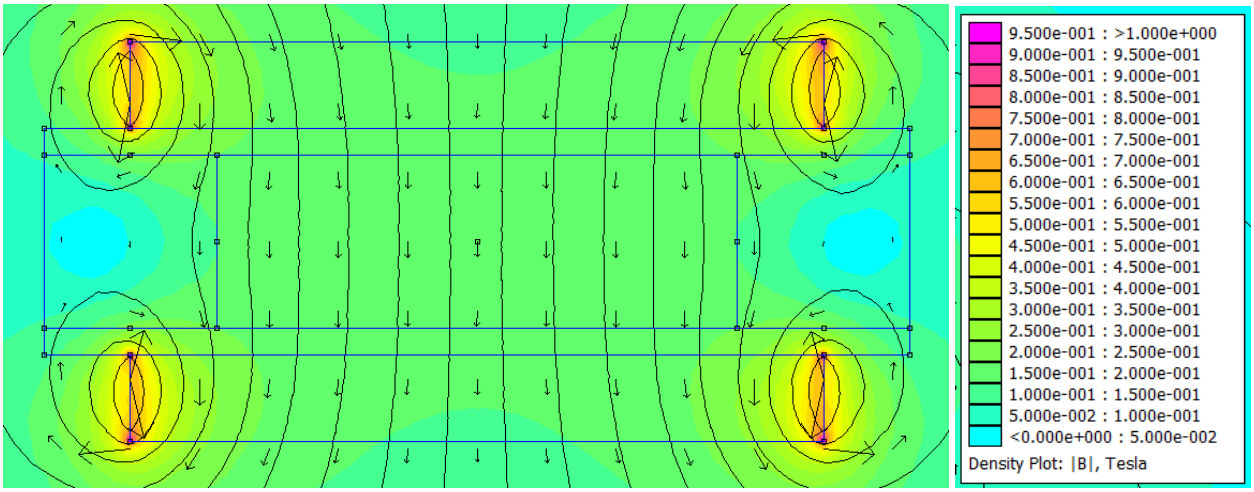

Figure 11-11. Magnetic field distribution inside the channel for 1/8" N52 magnets

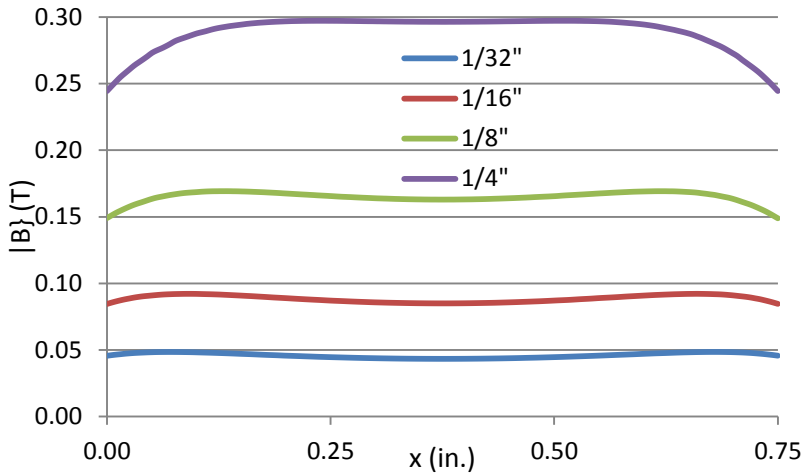

Figure 11-12. Magnetic field at channel centerline for different thicknesses of N52 magnets

Figure 11-13 shows results from 10 runs of the Lorentz channel thruster with 1/8" magnets, for positive and negative bias. The device was found to ignite at 530 V at 3 Torr and was found to draw a current of 13 mA, resulting in a power dissipation of 6.89 W. Unlike the electrostatic thrusters, a net force is clearly discernible for the duration when the thruster is on. The thrust for the positive bias is seen to be around 0.5 μN, whereas for the negative bias it is around half that value at about 0.25 μN. This asymmetry may be explained by the fact that the bias is reversed by reversing the polarity of the powered electrode while keeping the ground electrode as is. The plasma is seen to be different in characteristics depending on the polarity of the powered electrode. These differences have to do with the differences in sheath characteristics at the respective electrode, which alter the spatial distribution of plasma characteristics. Measurements of plasma quantities like electron temperature and densities can reveal more about the qualitative differences in the two modes.

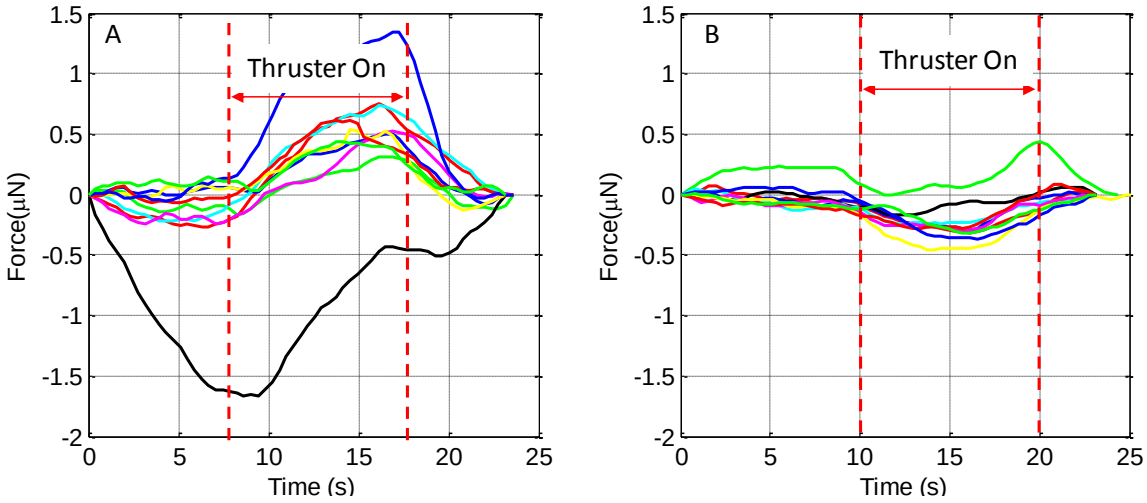

Figure 11-13. Force data for Lorentz channel thruster, 530 V at 3 Torr and 1/8" magnets. A) Positive bias. B) Negative bias.

The actuators Initial data from the Lorentz channel thruster look promising. Unlike the electrostatic channel thrusters, the Lorentz channel did manage to produce a force, albeit at the sub-micronewton level. It should be noticed, however, that this force was at an ambient pressure of 3 Torr, and no propellant flow was supplied or maintained. In an actual thruster, there will be some contribution from the pressure expansion of the propellant as it leaves the thruster, which will only improve performance. In the absence of plasma, this would essentially be a cold gas thruster, and would have a certain specific impulse associated with it. It remains to be seen if the presence of plasma and magnetic field would improve the specific impulse significantly.

CHAPTER 12
SUMMARY AND RECOMMENDATIONS FOR FUTURE WORK

12.1 Explanation of Low Pressure DBD Actuator Performance

The trend of DBD actuator force with reducing pressure, as presented in Chapter 7 provides an interesting opportunity for understanding the force production mechanism for these actuators better. The trend suggests an optimum pressure for peak effectiveness, which is dependent on the dielectric thickness and operating voltage. This trend suggests a corresponding optimum either in one of the important parameters of force production, or several competing mechanisms where by an increase in one is offset by a decrease in the other.

Current understanding of force production suggests a strong dependence on the production of oxygen negative ions as force carriers. This is corroborated by the fact that the actuator force drops linearly with dropping concentration of oxygen, as reproduced in Figure 12-1, while the discharge current drops only marginally (Enloe, McLaughlin, Font, & Baughn, 2006; Kim, Do, Mungal, & Capelli, 2007).

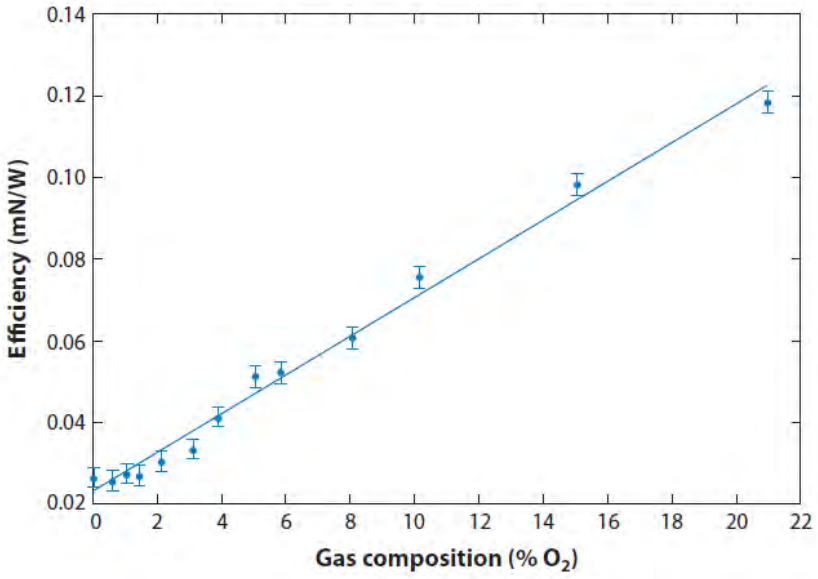

Figure 12-1. Dependence of actuator force on oxygen concentration (Enloe, McLaughlin, Font, & Baughn, 2006)

Based on these results, the researchers reached a conclusion that oxygen ions play an important role in the force production chain. It has been further argued that since bulk of the force is produced in the negative part of the cycle, it is the oxygen *negative* ion that plays a crucial role in transferring the force from the electron to the neutrals via electron attachment, since the collision cross section of oxygen ions and neutrals is much greater than electron-neutral collision cross-section.

At decreasing pressures, this force production chain could be affected in two ways. Firstly, the absolute electron number density itself will change as a result of changing degree of ionization, resulting in relatively more oxygen negative ions. Secondly, the electron temperature itself might change as a result of the reduced electric field. Collision cross sections of various electron interactions, including ionization and attachment, are well known to be a function of the electron energy and hence temperature. For electron attachment to oxygen (molecular and atomic), the cross section is a strong function of electron temperature as reported in literature (Itikawa, et al., 1989; Jeon, 2003).

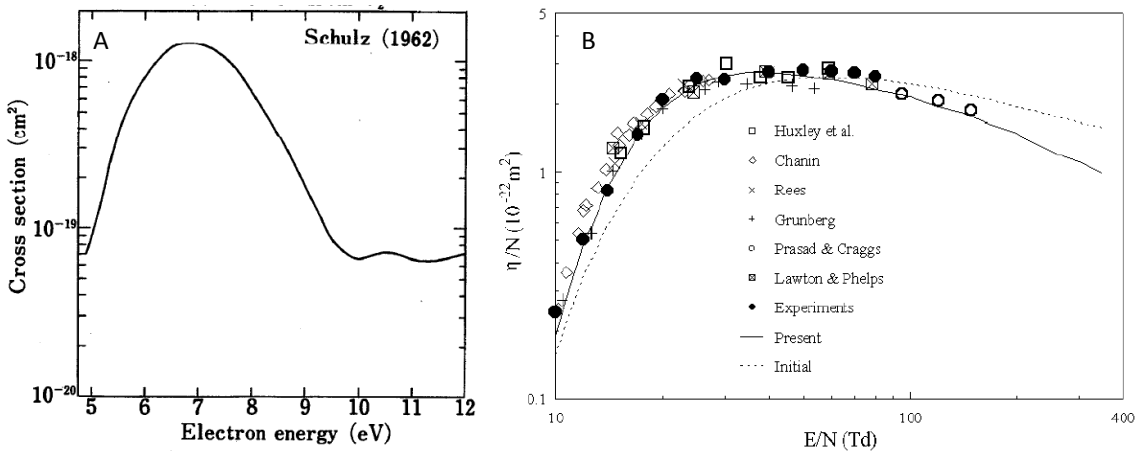

Figure 12-2. Electron attachment cross sections as a function of electron energy. A) For atomic oxygen (Itikawa, et al., 1989). B) For molecular oxygen (Jeon, 2003).

Both the atomic and molecular oxygen electron attachment cross section for O^- and the electron attachment coefficient for O_2^- seem to vary by upto an order of magnitude over the range of electron energies and reduced electric fields investigated. For thinner dielectrics, the increase in actuator force was found to be 700%. If the electron temperature varies in the right direction as the pressure goes down, conditions might be favorable for higher force transfer to the neutrals.

A verification of this hypothesis requires measurements in electron temperature and densities as a function of pressure. For conventional volumetric plasma, several intrusive (Langmuir probe, wave cut-off probe) and non-intrusive techniques (Thomson scattering, optical emission spectroscopy) are available. In DBD actuators, however, the plasma is confined to a very small region (O(mm)) close to the surface at the edge of the powered electrode. This renders intrusive probes unsuitable. Thomson scattering also relies on volumetric interactions of an electromagnetic wave with charged particles inside the plasma volume. Hence optical emission spectroscopy (OES) is the only method of choice available for investigate SDBD plasma parameters.

OES methods can be classified into two main types: Line intensity ratio method (Boltzmann plot) and spectral fitting methods. The main idea behind the line intensity ratio method is measuring the relative intensities of electronic transition of excited atoms or molecules of known species, which sheds light on their relative concentrations via the Boltzmann distribution. Spectral fitting, on the other hand, involves simulation the spectral contribution of various transitions to generate a spectrum that matches the experimental spectrum.

Spectra for SDBD actuators for three thickness of Garolite were obtained using an Ocean Optics USB2000 spectrometer with a wavelength range of 200-1100 nm and resolution of 0.45 nm. The actuators were placed inside an acrylic vacuum chamber and the emission from the plasma was collimated onto a fiber optic cable using a lens assembly, as shown in Figure 12-3.

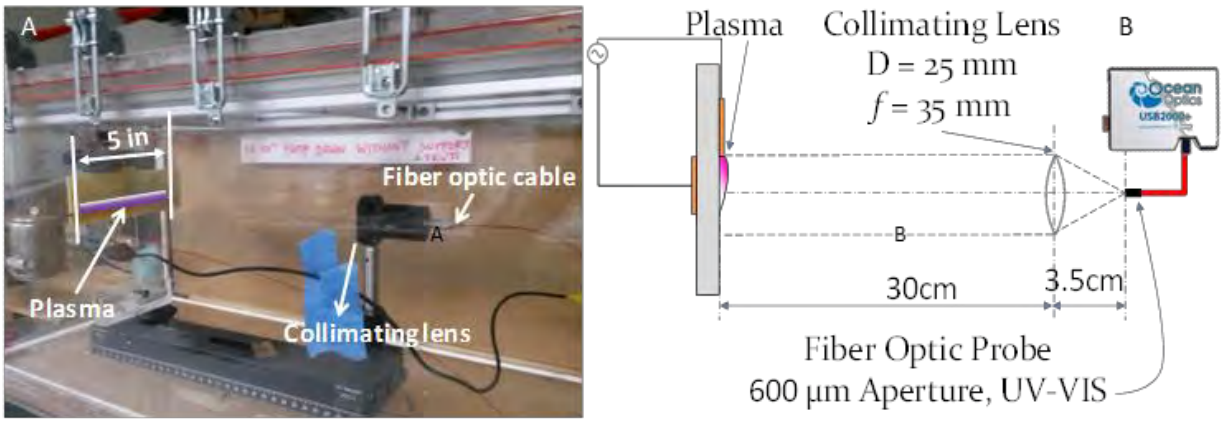

Figure 12-3. Experimental setup for optical emission spectroscopy. A) Actual arrangement . B) Schematic.

Spectra from the three different Garolite actuators (62.50mil, 9 kVpp, 93.75 kVpp 10 kVpp, 125.0mil 11 kVpp) are shown in Figure 12-4. As seen, the plasma emission grows stronger with decreasing pressure, indicating an increase in charged particle density. The spectrum has strong several peaks associated with various atomic and molecular transitions. These are identified in Figure 12-5.

Several researchers have used the nitrogen First Negative System (FNS) and the Second Positive System (SPS) line intensities for estimating electron temperatures and densities. Intensities of the (0,0) bands of the FNS at 391.44 nm and of the (0,2) bands of the SPS have been used to estimate electron temperature for a nitrogen pulsed discharge at a pressure of 2-4 Torr (Isola, Gomez, & Guerra, 2010). (Britun, Gillard, Ricard, Kim, & Han, 2007) used the line intensities of the N_2^+(B,0-X,0) transition

at 391.44nm and N_2(C,2-B.5) to estimate electron temperature and densities in an inductively coupled nitrogen plasma at pressures of 2-14 Torr.

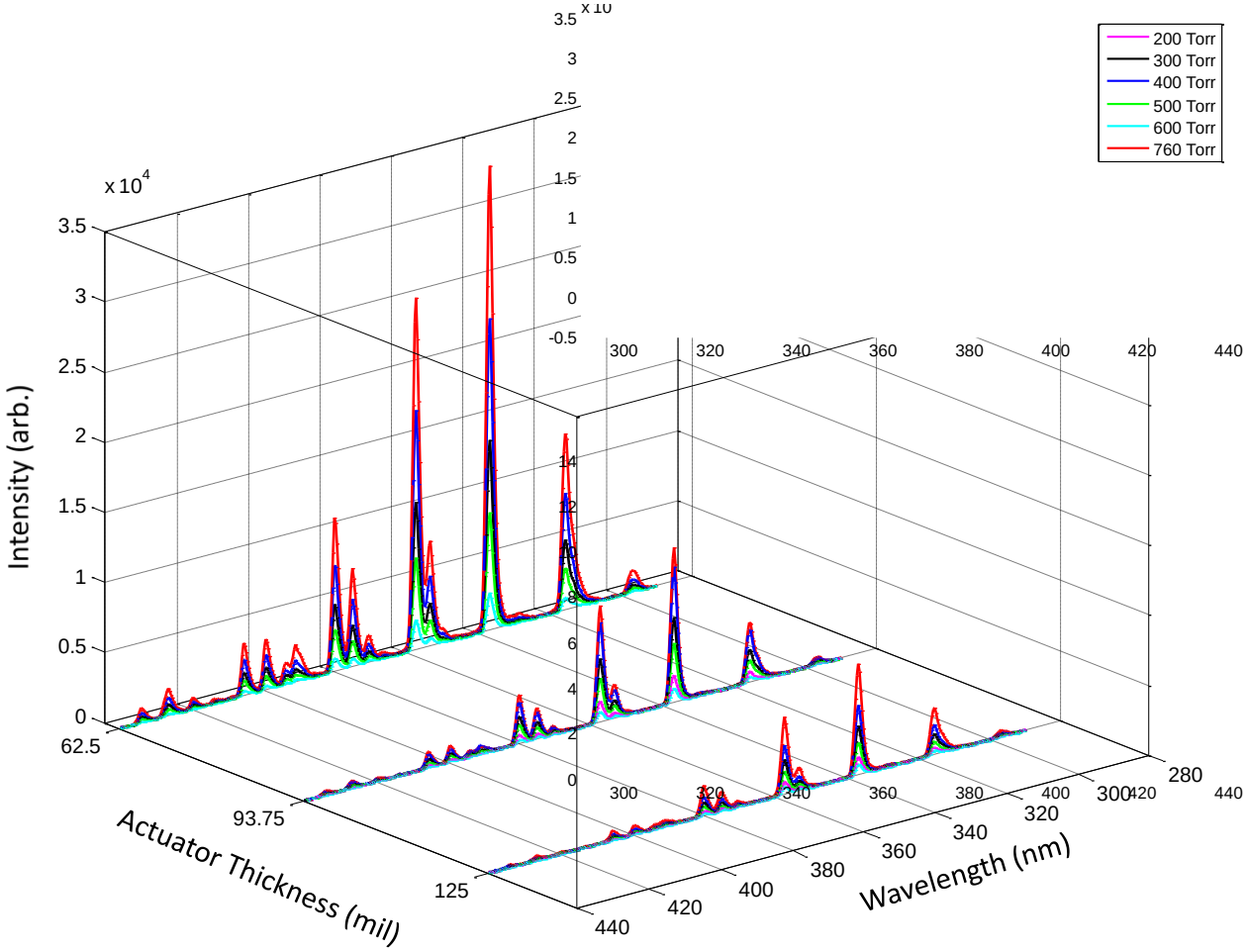

Figure 12-4. Plasma emission spectrum at different pressures and dielectric thicknesses

Optical diagnostics for SDBD have been performed recently (Wu, Li, Jia, Song, & Liang, 2013).by fitting simulated spectra with experimental one at pressures of 2-760 Torr. Results indicated an 800% increase in electron density at an intermediate pressure of about 375 Torr for the given actuator (0.5mm thick glass reinforced ceramic, ε_r = 3.48). The electron temperature was found to increase only marginally (from 1.63 eV to 1.91 eV) down to a pressure of about 45 torr, after which it increased rapidly with decreasing pressure, reaching 3 eV at 2 torr. The authors pointed that the discharge

transitions from filamentary to glow at this pressure, and the drastic rise in electron temperature might be a result of changing plasma behavior in this pressure regime.

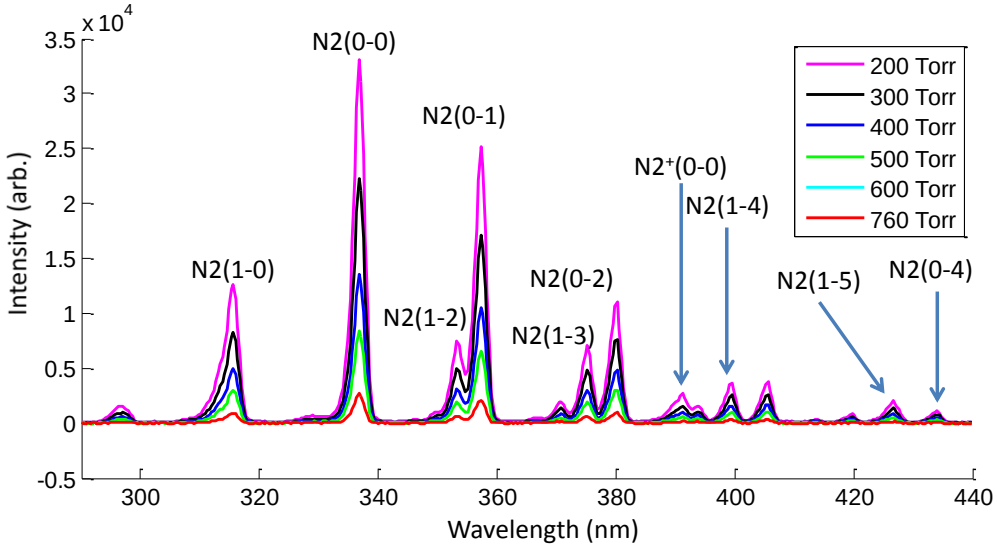

Figure 12-5. Identification of select transition peaks for actuator discharge spectra

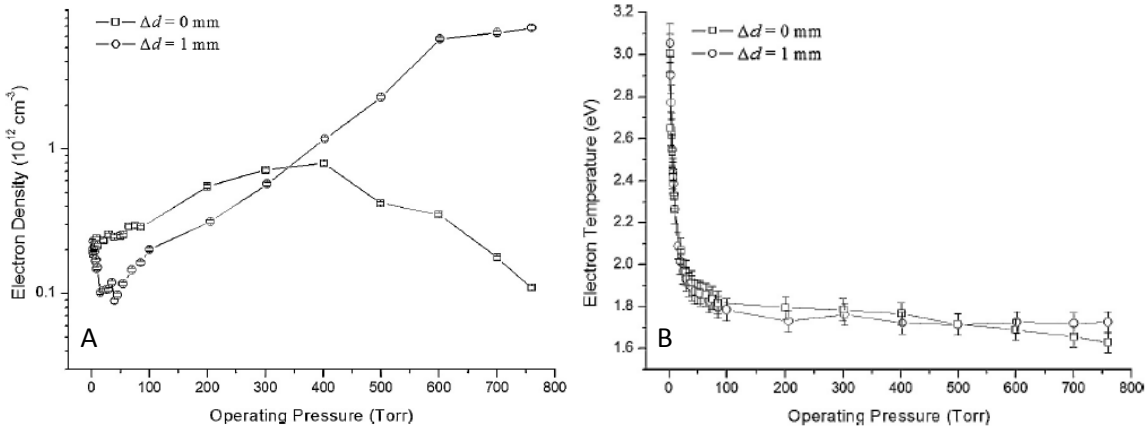

Figure 12-6. Variation of DBD plasma parameters with with pressure. A) Electron density. B) Electron temperature. (Wu, Li, Jia, Song, & Liang, 2013)

It is important to note that the thrust from the plasma actuators also shows a local maximum at an intermediate pressure like the electron density. Whether there is a cause and effect relationship between the two remains to be investigated. There is not enough data on low pressure electron and temperature and densities to investigate this with vigor. Towards this end, spectroscopic data was gathered for three different

thicknesses of dielectric to see if the pressure at which electron density peaks shows the same trend as the pressure at which thrust peaks.

The current resolution of the spectrum data, however, is not sufficient to allow spectral fitting methods to be used. Only a crude estimate of electron temperature could be obtained using the line intensity ratio method. Figure 12-7 shows the results. The values of electron temperature are seen to be more or less constant over the range of pressures and dielectric thicknesses tested, with a value of around 4.25. This value is higher than that reported by (Wu, Li, Jia, Song, & Liang, 2013). Other researchers, however, have reported electron temperature values of upto 3.75 (Figure 12-7), in light of which a value of 4.25 eV doesn't sound unreasonable.

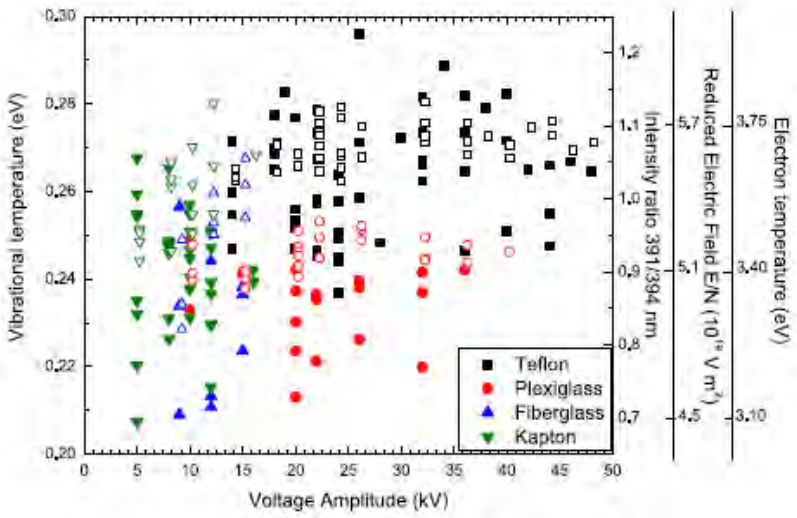

Figure 12-7. Electron temperature values for various dielectrics at different voltages.

The inherent limitation of the line intensity ratio is the assumption of complete thermal equilibrium, where all the species are in equilibrium at the same temperature. DBD plasmas are known to be non-thermal non-equilibrium plasma with vastly different electron and ion/neutral temperatures. Hence any reliable extraction of electron temperature and densities would need to resort to more detailed methods like spectral

fitting, which has been demonstrated to provide good estimates even for non-equilibrium plasma (Laux, Spence, Kruger, & Zare, 2003). Spectral fitting either requires in-depth knowledge of the subject to generate simulated spectra, or uses commercial software (e.g. Specair) that generate the spectra when the gas composition, pressure, and an initial guess temperature is specified. The spectra are then iteratively made to converge with the experimental spectra, given estimates of rotational, vibrational, and electronic temperature. Moreover, the experimental data needs to be high resolution ($\Delta\lambda \sim 0.05$) to obtain good spectral fit. Neither of these resources are at disposal for current work. Should these become available in the future, the role of electron density change in thrust production should be investigated.

12.2 Effect of Actuator Geometry on Performance

While investigating the effect of magnetic field on circular DBD actuators, it was discovered that the thrust form a circular geometry was significantly less than that from the linear actuator of the same wetted perimeter. This suggests that the effect of boundedness needs to be assessed to understand changes in performance of a certain actuator geometry. The change in performance may arise from the fluid dynamics of the problem. To this end, a circular and a linear DBD actuator with identical actuator and operating parameter were studied Figure 12-8 provides the details of these designs.

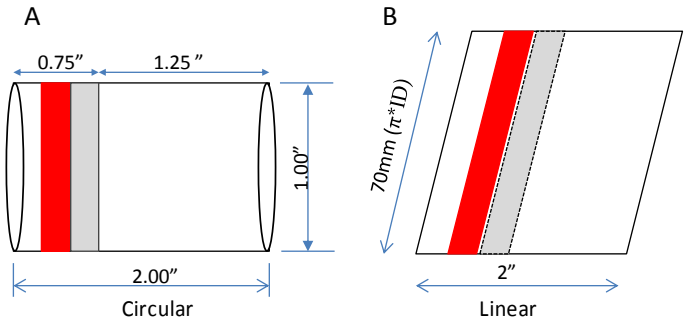

Figure 12-8. Details of actuators geometries. A) Ring. B) Linear.

The actuators were made to have identical wetted lengths, i.e. identical length of the plasma region. The ring actuator was made of an acrylic tube (ε_r = 3.0, ID: 0.875", OD: 1:00"), whereas the linear actuator was made of a flat plate of acrylic (ε_r = 3.0, 80mm width x 1.5mm thick) . Both actuators had identical total length along the flow direction (2.00"). The ring actuators had ¼" inch exposed copper tape electrode (40 micron thick) affixed on the inner surface of the tube with ¼" upstream gap, and the ground electrode was placed on the outer surface 0.5" from the upstream edge such that there was no lateral gap between the downstream edge of the powered electrode and the upstream edge of the ground electrode. The linear actuator electrodes were placed in an identical configuration, with an overall length of 70mm to match the inner periphery of the ring actuator. The actuators were powered using the two-stage amplification scheme of Figure 7-8. Actuator thrust was measured using the Ohaus precision balance. Flow field measurements were made using pitot tube as well as Particle Image Velocimetry (PIV) The actuators were run at a range of voltages to study voltage dependence of respective trends.

Results from the thrust measurement are presented in Figure 12-9. It is seen that the circular actuators produce substantially lower thrust than their linear counterparts, everything being same. The thrust from the ring actuators is over almost 50% lower than the linear actuators for most voltages.

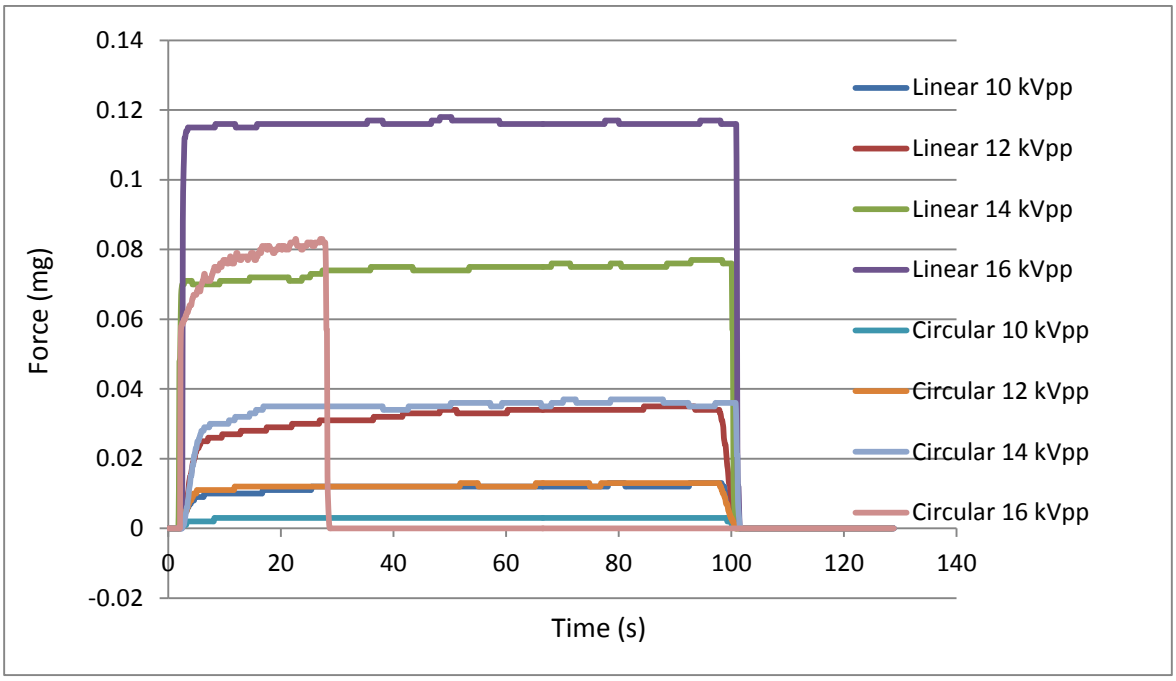

Figure 12-9. Thrust comparison of linear and circular actuators

Pitot measurements for the two actuator velocity profiles indicate significant differences (Figure 12-10). The velocity profile for linear actuator clearly shows the flat plate boundary layer behavior with no-slip condition imposed at the wall. The peak velocity is found to be very close to the wall, as is generally the case in a wall-jet. The peak velocity and the vertical height at which it occurs is seen to be a function of the operating voltage, with higher voltages resulting in a higher peak velocity which moves closer to the wall. For the circular actuator, the boundary layer was found to be much thicker than the flat plate. The peak velocity was seen to increase with voltage like the linear actuator, and the location of the peak was found to move closer to the wall. This might be attributed to the fact that the boundary layer has to swell in a bounded domain to accommodate the same momentum as the semi-bounded domain. This effect might be critical if the plasma channel height is small enough to cause boundary layer merger.

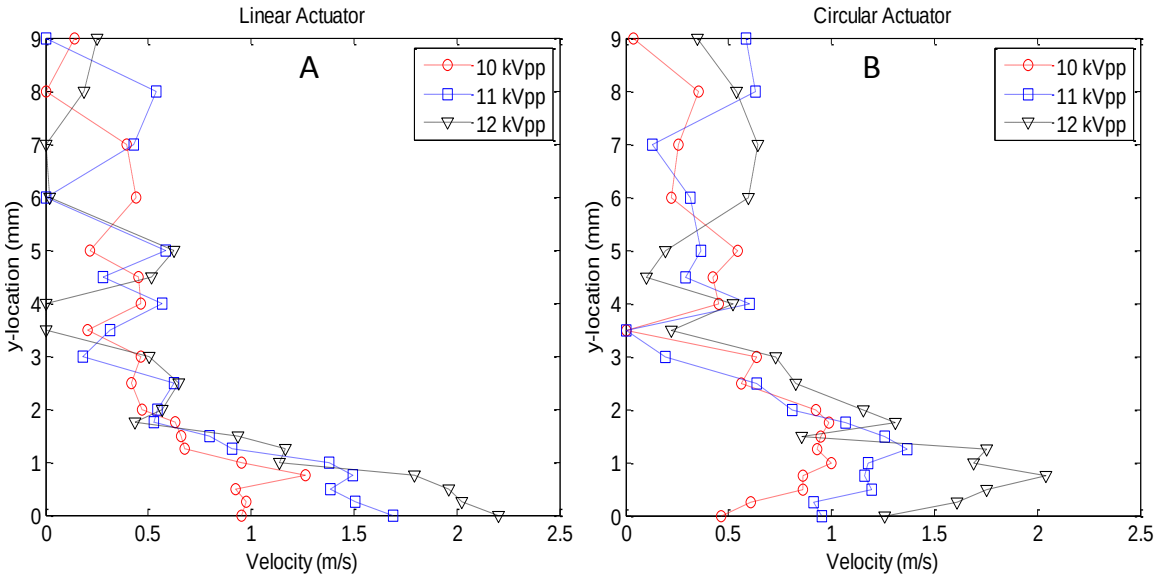

Figure 12-10. Differences in velocity profiles different geometries. A) Linear actuator. B) Circular actuator

Result from PIV for the flat plate and ring actuator suggest a similar story. Figure 12-11 show the flow field for the flat plate actuator at varying voltage.

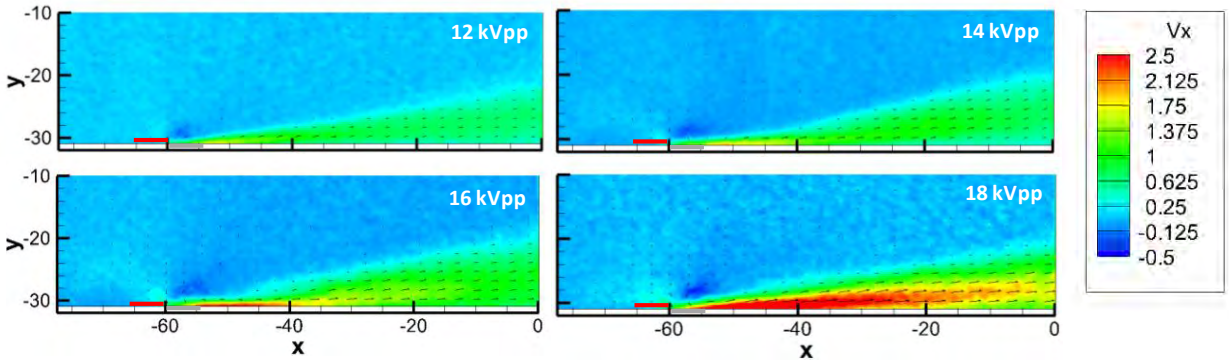

Figure 12-11. Flow field for linear actuator at varying voltages (5 kHz driving frequency)

It is seen that the results agree with the pitot probe velocity profiles, with peak velocities increasing and location of peak velocity decreasing. This has to do with the fact that most of the momentum is injected close to the wall and at higher velocities the gradients are able to remain sharp without much relative dissipation. At lower velocities the velocity profile diffuses out much quicker.

Flow field results for circular actuators are presented in Figure 12-12 for the same voltages. Again we see that, as expected, the peak velocity increases with voltage. The boundary later does not have a fully developed parabolic profile suggesting the downstream length is shorter than the minimum length required to achieve this. Furthermore, there is a clear asymmetry in the flow, which might have to do with slight imperfections in electrode spacing along the periphery of the actuator.

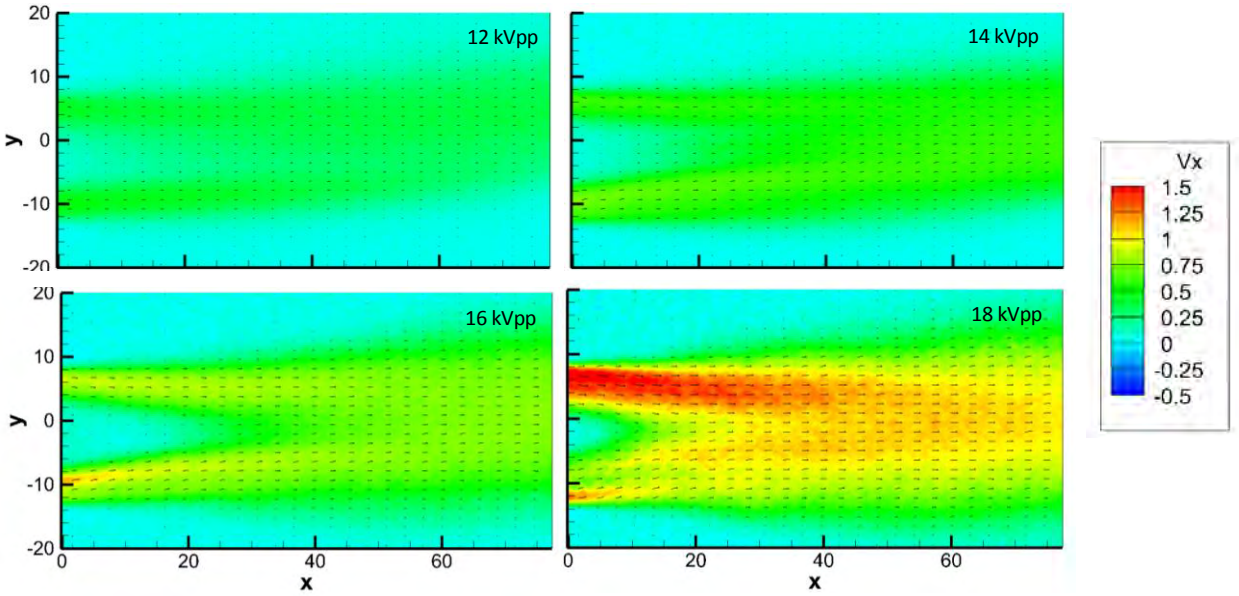

Figure 12-12. Flow field for circular actuator at varying voltages

Figure 12-13 compares the boundary later data extracted from the PIC flow field results for the two geometries at identical downstream distances (x=32mm). While the profiles from the linear actuator look as anticipated, flowfield asymmetry is very apparent in the circular actuator velocity profiles. More importantly, peak velocities and their locations show considerable difference, as was apparent from pitot measurements. Figure 12-14 shows peak velocities for the linear and the circular actuator (minimum and maximum values for the latter due to asymmetry). It is seen that the values from the

circular actuator are consistently lower, with the difference become more acute with increasing voltage with a reduction of almost 33% compared to linear actuator.

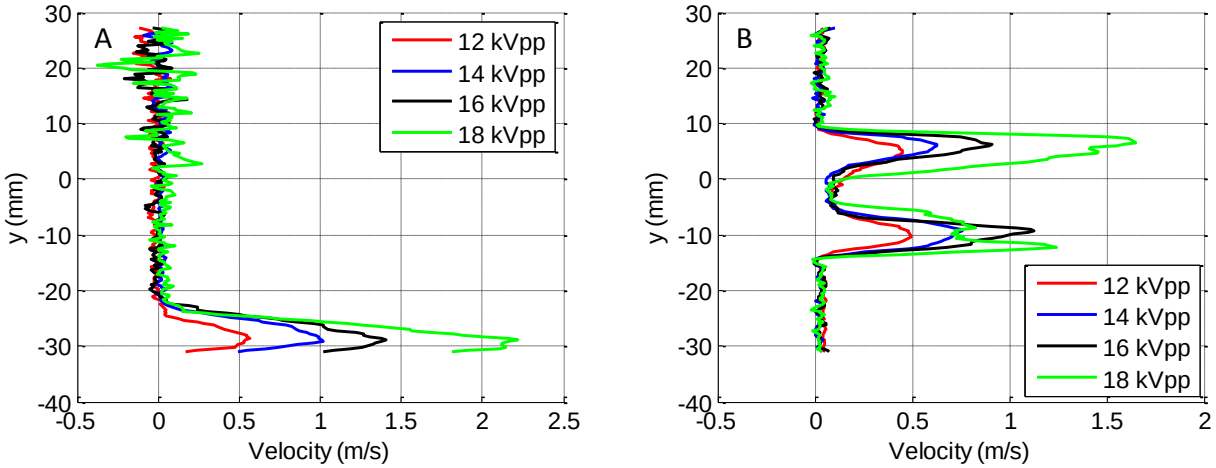

Figure 12-13. Velocity profiles from PIV. A) Linear actuator. B) Circular actuator

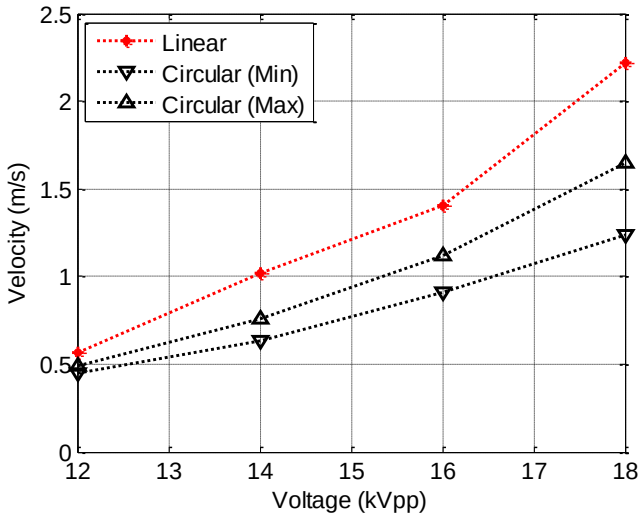

Figure 12-14. Peak velocities for linear and circular actuators as a function of voltage

This geometry dependence should be explored in more details. One parameter could be the radius of the circular actuator and to see if the loss in thrust becomes acute with decreasing radius. This effect is important for any device that uses DBD for transport of fluid in confined narrow spaces such as plasma channel thrusters (like FMEJ), or plasma based micro pumps.

12.3 Exploration of Lorentz Channel Thruster Design Space

The Lorentz channel thruster demonstrated a force of about 0.5 μN at a magnetic field of 0.1 Tesla at the channel centerline. This leaves room for exploring the effect of magnetic field strength on thrust. Optical emission spectroscopy could be used to estimate number densities and temperatures of charged species to understand spatial homogeneity of the plasma and explain the observed asymmetry in force with respect to the voltage bias. There is considerable design space for optimizing such a thruster vis-à-vis electrode separation, channel length, magnetic field. These parameters should be explored to aid design of a feasible thruster prototype.

Furthermore, the force production mechanism implies the charged particles could be exiting the thruster at an angle to the intended thrust vector. This might happen if the magnetic field is not ideal, leading to non-optimal curvature of trajectories. This is illustrated in Figure 12.15.

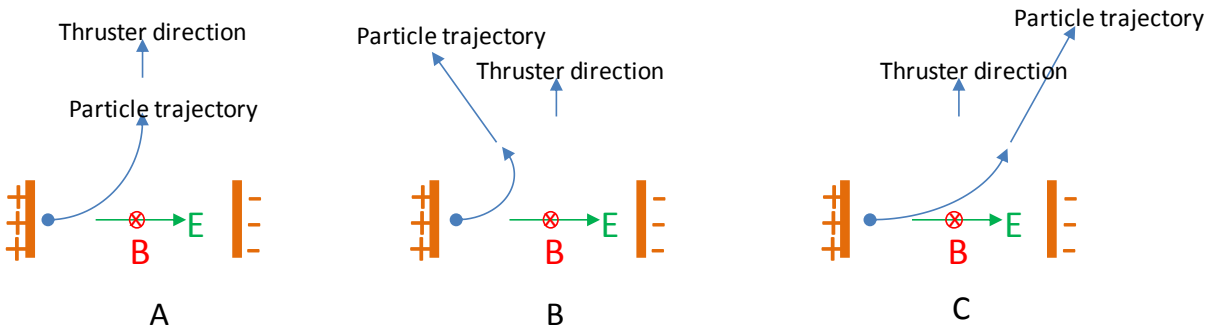

Figure 12-15. Particle trajectories and thrust vector for various B-field strengths. A) Optimum curvature. B) Excessive curvature. C) Insufficient curvature.

Direct estimate of the particle trajectories requires knowing the particle velocity *v*, which depends on the particle mobility and diffusivity. Even an elementary estimate of *v* requires knowledge of physical plasma quantities like particle densities and temperatures, which could be explored in the future.

The thrust vector direction can be estimated by measuring the thrust from two independent directions of the thruster, and analyzing thrust components to estimate the thrust vector direction and magnitude. For instance, the thruster could be placed with two orientations 90° apart, and the thrust measured and analyzed for thrust the vector.

REFERENCES

Abe, T., Takizawa, Y., & Soto, S. (2008). Experimental Study for Momentum Transfer in a Dielectric Barrier Discharge Plasma Actuator. *AIAA Journal, 46*(9).

Ahmed, Z., Gimelshein, S., & Ketsdever, A. (2005). Numerical Analysis of Free Molecule Micro-Resistojet Performance. *41st AIAA/ASME/SAE/ASEE Joint Propulsion Conference & Exhibit.* Tucson, AZ.

Alexander, M., Stark, J., Smith, K., Stevens, B., & Kent, B. (2003, June). Electrospray Performance of Microfabricated Colloid Thruster Arrays. *Journal of Propulsion and Power, 22*(3), 620-627.

Balagangadhar, D., & Roy, S. (2001). Design Sensitivity Analysis and Optimization of Steady Fluid-Thermal Systems Computer Methods. *Applied Mechanics and Engineering, 190*(42), 5465-5479.

Barnhart, D. J., Vladimirova, T., & Sweeting, M. N. (2007, November-December). Very-Small-Satellite Design for Distributed Space Missions. *Journal of Spacecrafts and Rockets, 44*(6).

Bartlett, P., & Stelbovics, A. (2002). Calculation of electron-impact total-ionization cross sections. *Physical Review A, 66*.

Bayt, R. L., Breuer, ,. K., & Ayon, A. A. (1998). DRIE-Fabricated Nozzles for Generating Supersonic Flows in Micropropulsion Systems. *Proceedings of the Solid-State Sensor and Actuator Workshop.* Hilton Head, SC.

Biganzoli, I., Barni, R., Riccardi, C., Gurioli, A., & Pertile, R. (2013). Optical and electrical characterization of a surface dielectric barrier discharge plasma actuator. *Plasma Sources Sci. Technol, 22*.

Blanco, A., & Roy, S. (2013). Numerical Simulation of a Free Molecular Electro Jet (FMEJ) for In-Space Propulsion. *51st AIAA Aerospace Sciences Meeting.* Grapevine, TX: AIAA.

Blanco, A., & Roy, S. (2013). Numerical Simulation of a Free Molecular Electro Jet (FMEJ) for In-Space Propulsion. *51st AIAA Aerospace Sciences Meeting.* Grapevine, TX: AIAA.

Britun, N., Gillard, M., Ricard, A., Kim, Y. M., & Han, J. G. (2007). Detrmination of the vibrational, rorational and electron temperatures in N2 and Ar-N2 rf discharge. *Journal of Physics: D, 40*.

Burton, R. (n.d.). *Microdischarge Cavity (MCD) Thruster for Small Satellites.* Retrieved April 20, 2013, from http://www.ae.illinois.edu/: http://www.ae.illinois.edu/isgc/esmd/documents/cuaburton2010mcd.pdf

Burton, R., Eden, G., Park, S.-J., Yoon, J., Chadenes, M., Garrett, S., . . . Carroll, D. (2009). Initial Development of the Microcavity Discharge Thruster. *31st International Electric Propulsion Conference.* Ann Arbor, MI.

Burton, R., Gary, E., Raja, L., park, S.-J., Laystrom-Woodard, J., & Chadenes, M. (2011). *Thrust and Efficiency Performance of the Microcavity Discharge Thruster.* University of Illinois at Urbana-Champaign. Arlington, VA: Air Force Office of Scientific Research.

Campbell, N., & Roy, S. (2014). Plasma channel flows: Electro-fluid dynamic jets. *Applied Physics Letters, 105*.

Cavendish, H. (1798). Experiments to determine the Density of the Earth. *Philosophical Transactions of the Royal Society of London (Part II), 88*, 469-526.

Chen, F. F. (1984). *Introduction to Plasma Physics and Controlled Fusion.* Plenum Press.

Corke, T. C., Enloe, C. L., & Wilkinson, S. P. (2009). Dielectric Barrier Discharge Plasma Actuators for Flow Control. *Annu. Rev. Fluid Mech, 45*, 505-29.

Corke, T. C., Mertz, B., & Patel, M. P. (2006). Plasma Flow Control Optimized Airfoil. *44th AIAA Aerospace Sciences Meeting and Exhibit.* Reno, NV.

Coulomb, C. (1785). Premier mémoire sur l'électricité et le magnetism. 569-577.

Daniel, J. (1999, Nov 7). *Introduction to Atmospheric Chemistry.* Princeton University Press. Retrieved Nov 7, 2014, from http://acmg.seas.harvard.edu/people/faculty/djj/book/bookchap2.html#27009

Darrin, A., & O'Leary, B. (2009). *Handbook of Space Engineering, Archaeology, and Heritage.* CRC Press.

Durscher, R. J. (2011). On Multi-Barrier Plasma Actuators. Orlando, FL: 49th AIAA Aerospace Sciences Meeting.

Durscher, R. J. (2012). *Characterization of Novel and Conventional Dielectric Barrier Discharge Actuators.* PhD Thesis.

Durscher, R., & Roy, S. (2012). Aerogel and ferroelectric dielectric materials for plasma actuators. *J. Phys. D: Appl. Phys., 45*.

Durscher, R., & Roy, S. (2012). Aerojel and ferroelectric dielectric materials for plasma actuators. *Journal of Physics D: Applied Physics, 45*.

Durscher, R., & Roy, S. (2012). Evaluation of thrust measurement techniques for dielectric barrier discharge actuators. *Exp. Fluids, 53*.

Durscher, R., & Roy, S. (2012). Three-dimensional flow measurements induced from serpentine plasma actuators in quiescent air. *Journal of Physics D: Applied Physics, 45*.

Durscher, R., Stanfield, S., & Roy, S. (2012). Characterization and manipulation of the "saturation" effect by changing the surface temperature of a dielectric barrier discharge actuator. *Applied Physics Letters, 101*.

Enloe, C., Font, G., McLaughlin, T., & Orlov, D. (2008). Surface potential and longitudinal electric field measurements in the aerodynamic plasma actuator. *AIAA J, 46*, 2730-2740.

Enloe, C., McLaughlin, T., Font, G., & Baughn, J. (2006). Parameterization of temporal structure in the single dielectric barrier aerodynamic plasma actuator. *AIAA Journal, 44*, 1127-1136.

Epstein, A. H., Li, H. Q., jacobson, S. A., & Kerrebrock, J. L. (2005). A Bipropellant Liquid MicroRocket Engine System. *5th International Workshop on Micro and Nanotechnology for Power Generation and Energy Conversion Applications.* Tokya, Japan: PowerMEMS.

Erfani, R., Zare-Behtash, H., & Kontis, K. (2012). Plasma actuator: Influence of dielectric surface temperature. *Experimental Thermal and Fluid Science, 42*, 258-264.

Fine, N. E. (n.d.). *Plasma Catalysis for Enhanced-Thrust Single Dielectric Barrier Discharge Plasma Actuators.* North Kingstown, Rhode Island: Technical Notes, Applied Science Products.

Font, G. I. (2000). Boundary layer control with atmospheric plasma discharges. *40th AIAA/ASME/SAE/ASEE Joint Propulsion Conference.* Ft. Lauderdale.

Font, G. I., & Morgan, W. L. (2005). Plasma discharges in atmospheric pressure oxygen for boundary layer separation control. *35th AIAA Fluid Dynamics Conference and Exhibit.* Toronto.

Forte, M., Jolibois, J., Moreau, F., Touchard, G., & Cazalens, M. (2006). Optimization of a dielectric barrier discharge actuator by stationary and non-stationary measurements of the induced flow velocity: application to flow control. *3rd AIAA Flow Control Conference .* San Francisco.

Franz, G. (2009). *Low Pressure Plasmas and Microstructuring Technology.* Springer-Verlag.

Friedman, A., & Kennedy, L. (2011). *Plasma Physics and Engineering.* CRC Press.

Gamero-Castano, M. (2003, October). A torsional balance for the characterization of microNewton thrusters. *Review of Scientific Instruments, 74*(10).

Gamero-Castaño, M. (2003). A torsional balance for the characterization of microNewton thrusters. *74*(10).

Gamero-Castano, M., & Hruby, V. (2001). A Torsional Balance that Resolves Sub-micro-Newton Forces. *International Electrcic Propulsion Conference.*

Gamero-Castano, M., Hruby, V., & Martinez-Sanchez, M. (2001). A Torsional Balance that Resolves Sub-micro-Newton Forces. International Electric Propulsion Conference.

Gimeno, L., Talbi, A., Viard, R., Merlen, A., Pernod, P., & Preobrazhensky, P. (2010). Synthetic jets based on micro magneto mechanical systems for aerodynamic flow control. *Journal of Micromechanics and Microengineering, 20*.

Goebel, D. M., & Katz, I. (2008). *Fundamentals of Electric Propulsion.* Wiley.

Goldston, R. J., & Rutherford, P. H. (1995). *Introduction to Plasma Physics.* Institute of Physics.

Gregory, J. W. (2007). Force Production Mechanisms of a Dielectric-Barrier Discharge Plasma Actuator. Reno, Nevada: 45th AIAA Aerospace Sciences Meeting and Exhibit.

Gregory, J. W., Enloe, C. L., & Font, G. I. (2007). Force Production Mechanisms of a Dielectric-Barrier Discharge Plasma Actuator. Reno, Nevada: 45th AIAA Aerospace Sciences Meeting and Exhibit.

Griem, H. R. (1964). *Plasma Spectroscopy.* McGraw Boax.

Griffith, D. (2012). *Introduction to Electrodynamics.* Prentice Hill.

Hoskinson, R. H. (2010). Differences between dielectric barrier discharge plasma actuators with cylindrical and rectangular exposed electrodes. *43*.

Hotinceanu, M., Borsos, Z., & Dinu, O. (2010). *Aspects of Thermodynamic Equilibrium in Plasma.* Universităţii Petrol – Gaze din Ploieşti.

Huang, J., Corke, T. C., & Flint, T. O. (2006). Plasma Actuators for Separation Control of Low-Pressure Turbine Blades. *AIAA J., 44*(1), 51-57.

Humble, R., Henry, G., & Larson, W. (2002). *Space Propulsion Analysis and Design.* McGraw Hill.

Ikeda, T., Togawa, K., Nishida, T., Tahara, H., & Watanabe, Y. (2011). Research and Development of Very Low Power Cylindrical Hall Thrusters for Nano-Satellites. *32nd International Electric Propulsion Conference.* Wiesbaden, Germany.

Isola, L. M., Gomez, B. J., & Guerra, V. (2010). Determination of electron temperature and density in the negative glow of nitrogen pulsed discharge using optical emission spectroscopy. *Journal of Physics: D, 43*.

Itikawa, Y., Ichimura, K., Onda, K., Sakimoto, K., Takayanagi, K., Hatano , Y., . . . Tsurubuchi, S. (1989). Cross Section for Collisions of Electrons and Photons with Oxygen Molecules. *Journal of Physical and Chemical Reference Data, 18*(1).

Ito, T., Gascon, N., Crawford, W., & Cappelli, M. (2007, September-October). Experimental Characterization of a Micro-Hall Thruster. *Journal of Propulsion and Power, 23*(5), 1068-1074.

J, R. R. (1995). *Industrial Plasma Engineering.* CRC Press.

J.C. Zito, D. A. (2010). Investigation of Impedance Characteristics and Power Delivery for Dielectric Barrier Discharge Plasma Actuators. Orlando, FL: 48th AIAA Aerospace Sciences Meeting.

Jamison, A. K. (2001). Accurate Measurement of Nano-Newton Thrust for Micropropulsion System Characterizatio. International Electric Propulsion Conference.

Jamison, A., Ketsdever, A., & Muntz, E. P. (2001). Accurate Measurement of Nano-Newton Thrust for Micropropulsion System Characterization. *International Electric Propuslion Conference.*

Janson, S. W., Helvajian, H., Hansen, W. W., & Lodmell, J. (1999). Microthrusters for Nanosatellites. *The Second International Conference on Integrated Micro Nanotechnology for Space Applications.* Pasadena, CA.

Jeon, B.-H. (2003). Determination of Electron Collision Cross-Sections for the Oxygen Molecule using Electron Swarm Study. *Journal of the Korean Physical Society, 43*(4), 513525.

Ketsdever, A. D., Green, A. A., Muntz, E. P., & Vargo, S. E. (2000). Fabrication and Testing of the Free Molecule Micro Resistojets : Initial Results. *36th AIAA/ASME/SAE/ASEE Joint Propulsion Conference & Exhibit.* Huntsville, AL.

Ketsdever, A. D., Lee, R. H., & Lilly, T. C. (2005). Performance testing of a microfabricated propulsion system for nanosatellite applications. *Journal of Micromechanics and Microengineering, 15*, 2254-2263.

Kieckhafer, A., & King, L. (2007). Energetics of Propellant Options for High-Power Hall Thrusters. *JOURNAL OF PROPULSION AND POWER, 23*(1).

Kim, W., Do, H., Mungal, M., & Capelli, M. (2007). On the role of oxygen in dielectric barrier discharge actuation of aerodynamic flows. *Applied Physics Letters, 91*.

Kogelschatz, U. (2002). Filamentary, Patterned, and Diffuse Barrier Discharges. *30*(4).

Kogelschatz, U. (2003). Dielectric-barrier Discharges: Their History, Discharge Physics, and Industrial Applications. *23*(1).

Kohler, J., Bejhed, J., Kratz, H., Bruhn, F., Lindberg, U., Hjort, K., & Stenmark, L. (2002). A Hybrid Cold Gas Micothruster. *Sensor and Actuato, A97-98*, 587-598.

Koizumi, H. K. (2004). Development of thrust stand for low impulse measurement from microthrusters. *75*(10).

Koizumi, H., Kakami, A., Furuta, Y., Komurasaki, K., & Arakawa, Y. (2003). LIQUID PROPELLANT PULSED PLASMA THRUSTER. *28th International Electric Propulsion Conference.* Toulouse, France.

Koizumi, H., Komurasaki, K., & Arakawa, Y. (2004, Oct). Development of thrust stand for low impulse measurement from microthrusters. *Review of Scientific Instruments, 75*(10).

Kotsonis, M., & Ghaemi, S. (2011). Forcing mechanisms of dielectric barrier discharge plasma actuators at carrier frequency of 625 Hz. *JOURNAL OF APPLIED PHYSICS, 110*.

Kroesen, G. M., Schram, D. C., Timmermans, C. J., & De Haas, J. C. (1990). The Energy Balance of a Plasma in Partial Local Thermal Equillibrium. *18*(6).

Kuan, C.-K., Chen, G.-B., & Chao, Y.-C. (2007, Nov-Dec). Development and Ground Tests of a 100-Millinewton Hydrogen Peroxide Monopropellant Microthruster. *JOURNAL OF PROPULSION AND POWER, 23*(6), 1313-1320.

Langmuir, I. (1928). Oscillations in Ionized Gases. *14*(8).

Laux, C. O., Spence, T. G., Kruger, C. H., & Zare, R. N. (2003). Optical diagnositcs of atmospheric pressure air plasmas. *Plasma Sources Science and Technology, 12*, 125-138.

Lee, R. H., Bauer, A. M., Killingsworth, M. D., Lilly, T. C., & Duncan, J. A. (2007). Performance Characterization of the Free Molecule Micro-Resistojet Utilizing Water Propellant. *43rd AIAA/ASME/SAE/ASEE Joint Propulsion Conference & Exhibit.* Cincinnati, OH.

Lee, R., Lilly, T., Muntz, E., & Ketsdever, A. (2005). *Free Molecule Micro-Resistojet: Nanosatellite Propulsion.* Edwards, CA: Air Force Research Laboratory.

London, A. J., Ayon, A. A., Epstein, A. H., Spearing, S. M., Harrison, T., Peles, Y., & Kerrebrock, J. L. (2001). Microfabrication of a high pressure bipropellant rocket engine. *Sensors and Actuators A*(92), 351-357.

Longstaff, R., & Bond, A. (2011). The SKYLON Project. *17TH AIAA INTERNATIONAL SPACE PLANES AND HYPERSONIC SYSTEMS AND TECHNOLOGIES CONFERENCE.* San Francisco: AIAA.

Matlis, E., & Corke, T. (2005). AC plasma anemometer for hypersonic Mach number experiments. *43rd AIAA Aerospace Sciences Meeting and Exhibit.* Reno, NV: AIAA.

Matlis, E., Corke, T., Cameron, J., & Morris, S. (2008). A.C. plasma anemometer for axial compressor stall warning. *12th Int. Symp. Transp. Phenom. Dyn. Rotat. Mach.* Honolulu.

McPherson, J., Kim, J., Shanware, A., Mogul, H., & Rodriguez, J. (2002). Proposed Universal Relationship Between Dielectric Breakdown and Dielectric Constant. *International Electron Devices Meeting. 633.* IEEE.

Mestiri, R. H. (2010). An experimental study of a plasma actuator in absence of free airflow: Ionic wind velocity profile. *17*.

Miziolek, A. E., Palleschi, V., & Schechter, I. (2006). *Laser Induced Breakdown Spectroscopy.* Cambridge University Press.

Moreau, E. (2007). Airflow control by non-thermal plasma actuators. *Journal of Physics D: Applied Physics, 40*(3), 605.

Mueller, J. (1997). Thruster Options for Microspacecraft: A Review and Evaluation of Existing Hardware and Emerging technologies. *Proceedings of the 33rd AIAA/ASME/SAE/ASEE Joint Propulsion Conference. Paper No. AIAA-97-3058.* Seattle, WA: AIAA.

Mueller, J. (2000). *Micropropulsion for Small Spacecrafts.* (M. M. Micci, & A. D. Ketsdever, Eds.) Reston: AIAA.

Mueller, J., Goldberg, H., & Alkalai, L. (2007). MicroInspector Spacecraft Testbed: Breadboard Subsystem Demonstrations. *AIP conference Proceedings, 880*(742).

Mueller, J., Hofer, R., & Ziemer, J. (2010). *Survey of propulsion technologies applicable to cubesats.* Pasadena, CA: JPL.

Mueller, J., Ziemer, J., Richard, H., Wirz, R., & O'Donnell, T. (2008). A Survey of Micro-Thrust Propulsion Options forMicrospacecraft and Formation Flying Missions. *5'th Annual CubeSat Developers Workshop.* San Luis Obispo, CA.

Muller, J. (2000). Thruster Options for Microspacecraft: A Review and Evaluation of State-of-the-Art and Emerging Technologies. *AIAA J., 187*.

Orlov, D. (2006). *Modelling and simulation of single dielectric barrier discharge plasma actuators.* PhD Thesis, Notre Dame.

Paulson, C., & Soberster, A. (2013). Bespoke Balloon Launched Sensorcraft for Atmospheric Research Missions. *AIAA Balloon Systems (BAL) Conference.* Daytona Beach: AIAA.

Paulson, C., & Sobester, A. (2013). Parameterization and Geometric Optimization of Balloon Launched Sensorcraft for Atmospheric Research Missions. *51ST AIAA AEROSPACE SCIENCES MEETING.* Grapevine: AIAA.

Platt, D. (2002). A Monopropellant Milli-Newton Thruster System for Attitude Control of Nanosatellites. *16th Annual AIAA/USU Conference on Small Satellites.* Logan, UT.

Polzin, K., Raites, Y., Gayoso, J., & Fisch, N. (2010). Comparisons in Performance of Electromagnet and Permanent Magnet Cylindrical Hall Thrusters. *46th AIAA/ASME/SAE/ASEE Joint Propulsion Conference & Exhibit.* Nashville, TN: AIAA.

Post, M. L., & Corke, T. C. (2004a). Separation Control on High Angle of Attack Airfoil Using Plasma Actuators. *AIAA J, 42*(11), 2177-2184.

Post, M. L., & Corke, T. C. (2006). Separation Control Using Plasma Actuators: Dynamic Stall Vortex Control on Oscillating Airfoil. *AIAA J., 44*(12), 3125-3135.

Post, M., & Corke, T. (2004b). Separation Control using Plasma Actuators - Stationary & Oscillating Airfoils. *42nd AIAA Aerospace Sciences Meeting and Exhibit.* Reno, NV.

Rafatov, I. (2012). On the accuracy and reliability of different fluid models of the direct current glow discharge. *Physics of Plasmas, 19*.

Raizer, Y. P. (1987). *Gas Discharge Physics.* Springer-Verlag.

Rayburn, C. D., Campbell, M. E., & Mattick, A. T. (2005). Pulsed Plasma Thruster System for Microsatellites. *42*(1).

Rethmel, C., Little, J., Takashima, K., Sinha, A., Adamovich, I., & samimy, M. (2011). Flow Separation Control over an Airfoil with Nanosecond Pulse Driven DBD Plasm Actuators. *49th AIAA Aerospace Sciences Meeting including the New Horizons Forum and Aerospace Exposition.* Orlando, FL: AIAA.

Rossi, C., Larangot, B., Pham, P.-Q., Briand, D., Rooij, N., Puig-Vidal, M., & Samitier, J. (2006, December). Solid Propellant Microthrusters on Silicon : Desgin, Modeling, Fabrication, and Testing. *Journal of Microelectromechanical Systems, 15*(6), 1805-1815.

Rossi, C., Orieux, S., Larangot, B., Conto, T. D., & Esteve, D. (2002). Design, fabrication and modeling of solid propellant microrocket-application to micropropulsion. *Sensors and Actuators A, 99*, 125-133.

Roth, J. R. (1995). *Industrial Plasma Engineering.*

Roth, J. R. (1998). Boundary Layer Flow Control with a One Atmosphere Uniform Glow Discharge Surface Plasma.

Roth, J. R. (1998). Electrohydrodynamically Induced Airflow in a One Atmosphere Uniform Glow Discharge Surface Plasma. Piscataway, NJ: IEEE International Conference on Plasma Science.

Roth, J. R. (2000). Electrohydrodynamic Flow Control with a Glow-Discharge Surface Plasma. *38*(7).

Roth, J., Sherman, D. M., & Wilkinson, S. P. (2000). Electrohydrodynamic flow control with a Flow-discharge Surface Plasma. *AIAA J., 38*(7), 1166-1172.

Roth, J., Sherman, D., & Wilkinson, S. (1998). Boundary layer flow control with a One Atmosphere Uniform Glow Discharge Surface Plasma. *36th AIAA Aerospace Sciences Meeting and Exhibit.*

Roupassov, D. V. (2008). Flow separation control by plasma actuator with nanosecond pulse periodic discharge. *17th International Conference on Gas Discharges and Their Applications*, (pp. 609-612).

Roy, S. (2000). Combining Galerkin matrix perturbation with Taylor weak statement algorithms Computer Methods. *Applied Mechanics and Engineering, 184*, 345-358.

Roy, S. (2011, August 25). *Patent No. WO/2011/103194A2.* US.

Roy, S., & Pandey, B. P. (2002). Numerical Investigation of a Hall Thruster Plasma. *Physics of Plasma, 9*(9).

Roy, S., & Pandey, B. P. (2003). Modeling Low Pressure Collisional Plasma Sheath with Space-charge Effect. *Physics of Plasma, 10*(6), 2578-2585.

Roy, S., & Wang, C.-C. (2009). Bulk flow modification with hroseshoe and serpentine plasma actuators. *Journal of Physics D: Applied Physics, 42*.

Roy, S., Raju, R., Chuang, H. F., Cruden, B. A., & Meyyappam, M. (2003). Modeling gas flow through microchannels and nanopores. *Journal of Applied Physics, 93*(8), 4870-4879.

Rysanek, F., Hartmann, J., schein, J., & Binder, R. (2002). MicroVacuum Arc Thruster Design for a CubeSat Class Satellite. *16th Annual/USU Conference on Small Satellites.*

Sandau, R. (2010). Status andtrendsofsmallsatellitemissionsforEarthobservation. *Acta Astronautica, 66*(1-12).

Scharfe, D. B., & Ketsdever, A. (2009). *A Review of High Thrust, High Delta-V Options for Microsatellite Missions.* AFRL.

Schein, J., Qi, N., Binder, R., Krishnan, M., Ziemer, J., Polk, J., & Anders, A. (2001). Low Mass Vacuum Arc Thruster System for Station Keeping Missions. *27th International Electric Propulsion Conference.* Pasadena, CA: Electric Rocket Propulsion Society.

Schlichting, H. (2000). *Boundary-Layer Theory.* Springer.

Simon, D., Land, B., & Emhoff, J. (2006). Experimental Evaluation of a Micro Liquid Pulsed Plasma Thruster Concept. *42nd AIAA/ASME/SAE/ASEE Joint Propulsion Conference & Exhibit.* Sacramento, CA.

Smith, K., Stark, J., Krpoun, R., & Shea, H. (2009). Performance of a micro-fabricated Colloid thruster system. *31st International Electric Propulsion Conference.* Ann Arbor, MI.

Sóbester, A. (2011). *Stratospheric Flight.* London: Springer Praxis Books.

Sobester, A., Johnston, S., Scanlan, J., O'Brien, N., Hart, E., Crispin, C., & Cox, S. (2011). High Altitude Unmanned Air System for Atmospheric Science Missions. *11TH AIAA AVIATION TECHNOLOGY, INTEGRATION, AND OPERATIONS (ATIO) CONFERENCE.* Virginia Beach.

Sodano, H. (2006, June). Improved Concept and Model of Eddy Current Damper. *Transactions of the ASME, 128*.

Sodano, H. A., Bae, J.-S., Inman, D. J., & Belvin, W. (2006). Improved Concept and Model of Eddy Current Damper. *128*.

Soni, J., & Roy, S. (2013). Design and characterization of a nano-Newton resolution thrust stand. *84*.

Soni, J., & Roy, S. (2013a). Design of a microNewton Thrust Stand for Low Pressure Characterization of DBD Actuators. *51st AIAA Aerospace Sciences Meeting.* Grapevine, TX.

Soni, J., & Roy, S. (2013b). Low Pressure Characterization of DBD Actuators. *Applied Physics Letters, 102*.

Stoewer, H. (1996). The Enigma of Small Satellites for Earth Observation. *Acta Astronautica, 39*(9-12), 631-646.

Tajmar, A., & Genovese, A. (2003). Experimental validation of a mass- efficiency model for an indium liquid-metal ion source. *Applied Physics A, 76*(6), 1003-1006.

Thomas, F. O., Corke, T. C., Iqbal, M., & Kozlov, A. (2009). Optimization of Dielectric Barrier Discharge Plasma Actuators for Active Aerodynamic Flow Control. *AIAA Journal, 47*(9).

Thomas, F. O., Corke, T. C., Iqbal, M., Kozlov, A., & Schatzman, D. (2009). Optimization of Dielectric Barrier Discharge Plasma Actuators for Active Aerodynamic Flow Control. *AIAA J., 47*(9), 2169-2178.

Thomas, F. O., Kozlov, A., & Corke, T. C. (2006). Plasma actuators for bluff body flow control. *3rd AIAA Flow Control Conference.* San Francisco, CA.

Thomas, F., Kozlov, A., & Corke, T. (2008). Plasma actuators for bluff body flow control. *AIAA J. , 46*, 1921-1931.

Tirumala, R., Benard, N., Moreau, E., Fenot, M., Lalizel, G., & Dorignac, E. (2014). Temperature characterization of dielectric barrier discharge actuators: influence of electrical. *Journal of Physics: D, 47*, 12.

Uhm, H. S., Jung, S. J., & Kim, H. S. (2003, February). Influence of Gas Temperature on Electrical Breakdown in Cylindrical Electrodes. *Journal of the Korean Physical Society, 42*, S989-S993.

Valerioti, J., & Corke, T. (2012, July). Pressure Dependence of Dielectric Barrier Discharge Plasma Flow Actuators. *AIAA J., 50*(&), 1490-1502.

Versailles, P., Gingras-Gosselin, V., & Duc Vo, H. (2010, April). Impact of Pressure and Temperature on the Performance of Plasma Actuators. *AIAA J., 48*(4), 859-863.

Wang, C.-C. R. (2011). Geometry Effects of Dielectric Barrier Discharge on a Flat Surface. Orlando, FL: 49th AIAA Aerospace Sciences Meeting.

Wang, C.-C., & Roy, S. (2009). Three-dimensional simulation of a microplasma pump. *Journal of Physics D: Applied Physics, 42*.

Wang, C.-C., & Roy, S. (2011). Combustion stabilization using serpentine plasma actuators. *Applied Physics Letters, 99*(4).

Wertz, J., & Larson, W. (2007). *Space Mission Analysis and Design* (3rd ed.). Micocosm Press.

Wilkinson, S., Siochi, E., Sauti, G., Xu, T.-B., Meader, M. A., & Guo, H. (2014). Evaluation of Dielectric-Barrier-Discharge Actuator Substrate Materials. *45TH AIAA Plasmadynamics and Lasers Conference.* Atlanta, GA.

Wong, J., Reed, H., & Ketsdever, A. (2001). Temperature and Power Predictions for Flight-testing the Free Molecule Micro-Resistojet. *27th International Electric Propulsion Conference.* Pasadena, CA.

Wu, M.-H., & Lin, P.-S. (2010). Design, fabrication and characterization of a low-temperature co-fired ceramic gaseous bi-propellant microthruster. *JOURNAL OF MICROMECHANICS AND MICROENGINEERING, 20*.

Wu, M.-H., & Yetter, R. A. (2009). A novel electrolytic ignition monopropellant microthruster based on low temperature co-fired ceramic tape technology. *Lab On a Chip, 9*, 910-916.

Wu, Y., Li, Y., Jia, M., Song, H., & Liang, H. (2013). Effect of pressures on the emission chatacteristics of surface dielectric barrier discharge. *Sensors and Actuators: A, 203*.

You, D., & Moin, P. (2008). Active control of flow separation over an airfoil using synthetic jets. *Journal of Fluids and Structures, 24*(8).

Young, D., Munson, B., & Okiishi, T. (2004). *A breif Introduction to Fluid Mechanics* (3rd ed.). Wiley & Sons.

Young, J. L. (2001). *Determination of Atmospheric Density in Low-Earth Orbit Using GPS Data.* Annapolis, Maryland: United States Naval Academy. From www.dtic.mil/get-tr-doc/pdf?AD=ADA392479

Yuan, T., Li, A., Huang, B., Chen, Y.-T., & Chen, C. (2011). Design, Fabrication, and Test of a MEMS-based Millinewton-Level Hydrazine Thruster. *Journal of Propulsion and Power, 27*(2).

Zhang, K. I., Chou, S. K., & Ang, S. S. (2004). Development of a solid propellant microthruster with chamber and nozzle etched on a wafer surface. *Journal of Micromechanics and Microengineering, 14*, 785-792.

Zhang, K. L., Chou, S. K., Ang, S. S., & Tang, X. S. (2005). A MEMS-based solid propellant microthruster with Au/Ti igniter. *Sensors and Actuators A, 122*, 113-123.

Zhao, P. R. (2012). Study of Spectrum Analysis and Signal Biasing for Dielectric Barrier Discharge Actuator. Nashville, TN: 50th AIAA Aerospace Sciences Meeting.

Ziemer, J. K. (2001). Performance Measurements Using a Sub-Micronewton Resolution Thrust Stand. International Electric Propulsion Conference.

Ziemer, J. K. (2001). Performance Measurements Using a Sub-Micronewton Resolution Thrust Stand. *International Electric Propulsion Conference.*

Zito, J. C. (2012a). Flow and force inducement using micron size dielectric barrier discharge. *100*(193502).

Zito, J. C. (2012b). Microscale Dielectric Barrier Discharge Plasma Actuators: Performance Characterization and Numerical Comparison. *43rd AIAA Plasmadynamics and Lasers Conf.* New , LA: AIAA.

Zito, J. C., Arnold, D. P., Houba, T., Soni, J., Durscher, R. J., & Roy, S. (2012b). Microscale Dielectric Barrier Discharge Plasma Actuators: Performance Characterization and Numerical Comparison. *43rd AIAA Plasmadynamics and Lasers Conf.* New , LA: AIAA.

Zito, J. C., Durscher, R. J., Soni, J. S., Roy, S., & Arnold, D. (2012a). Flow and force inducement using micron size dielectric barrier discharge. *100*(193502).

BIOGRAPHICAL SKETCH

Jignesh conducted his undergraduate studies at Mumbai University, followed by a graduate degree in Aerospace Propulsion at IIT Bombay. He held the position of Systems Engineer for Rolls-Royce Defense Aerospace from 2007-2009. Jignesh started his doctoral research in the field of plasma actuators at UF in 2010, graduating in December 2014.